

Design, Implementation, and Testing of Apparatus to Investigate Combustion Phenomena Relevant to High-Altitude Relight

A Major Qualifying Project Report
Submitted to the Faculty of the
WORCESTER POLYTECHNIC INSTITUTE
in Partial Fulfillment of the Requirements for the
Degree of Bachelor of Science
in Aerospace Engineering

by

Ethan Davis

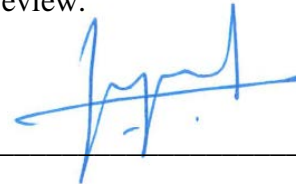
Meenakshi Kodali

John Sirois

Jonathan Stern

*This report represents the work of one or more WPI undergraduate students submitted to the faculty as evidence of completion of a degree requirement. WPI routinely publishes these reports on the web without editorial or peer review.

March 24, 2022
Approved by:



Jagannath Jayachandran, Advisor
Assistant Professor, Aerospace Engineering Department
WPI

Abstract

Relight is the process of reigniting an aircraft engine after the extinction of the flame in the combustion chamber. With flameout typically occurring at low pressure and temperature conditions, present at cruise altitudes, successful relight can be a challenge, especially for modern low-NO_x, lean-burn engines. This project aimed to replicate high-altitude combustor conditions in a custom-built experimental apparatus. This design consisted of a counterflow configuration supplied with fuel spray droplets to understand ignition and flame propagation relevant to high-altitude relight. A pressure vessel and cooling system were designed to emulate high-altitude atmospheric conditions. To improve the designs, structural, fluid, and thermal analyses were conducted using ANSYS, FLUENT, and COMSOL. Lastly, testing was conducted to validate the experimental apparatus.

“Certain materials are included under the fair use exemption of the U.S. Copyright Law and have been prepared according to the fair use guidelines and are restricted from further use.”

Acknowledgements

We would like to thank the following individuals and groups for their help and support throughout the entirety of this project.

- Professor Jayachandran
- Tina Stratis
- Katherine Crowley
- Adriana Hera
- Nolan Dexter-Brown

Abstract.....	1
Acknowledgements.....	2
Authorship	14
1 Introduction	16
1.1 Background and Literature Review	16
1.1.1 Relight Conditions.....	16
1.1.2 Atmospheric and Combustor Conditions	17
1.1.3 Flow Characteristics	21
1.1.4 Atomizers.....	25
1.1.5 Fuel Types	29
1.1.6 Air to Fuel Ratio	31
1.1.7 Experimental Configurations.....	32
1.1.8 Burner Nozzle Design	34
1.1.9 Particle Image Velocimetry	37
1.1.10 Pressure Vessel.....	38
1.2 Project Design Requirements.....	41
1.3 Project Goals.....	41
1.4 MQP Objectives and Methods	41
1.5 Project Management	42
1.6 MQP Gantt Chart	44

2	Preliminary Design.....	45
2.1	Experimental Configuration.....	46
2.2	Laminar Flame Speed	46
2.3	Air Flow Rates	47
2.3.1	Air Flow Control	47
2.3.2	Flow System Design.....	48
2.4	Fuel Types for Testing	54
2.4.1	Methane	54
2.4.2	Heptane	55
2.4.3	Ethanol.....	55
2.4.4	Kerosene	55
2.5	Atomizer Requirements	56
2.6	Burner Dimensions	57
2.7	Pressure Vessel	62
2.7.1	Pressure Vessel CAD Design	72
3	Modeling	75
3.1	Air to Fuel Ratio and Droplet Vaporization Times	75
3.1.1	Methane AFRs - 9.52 molar; 17.16 mass	76
3.1.2	Heptane AFRs – 52.36 molar; 30.20 mass	76
3.1.3	Ethanol AFRs – 14.28 molar; 8.95 mass	76

3.1.4	Heptadecane AFRs – 123.76 molar; 14.84 mass.....	76
3.2	Burner FLUENT Modeling.....	87
3.2.1	Grid Independence Study	87
3.2.2	Comparison Between Straight, Linear, and Optimized Contour.....	89
3.3	Fluid Flow Heat Transfer COMSOL Modelling	93
3.4	Pressure Vessel Analysis	108
4	Experimental Results.....	113
4.1	Particle Image Velocimetry Testing	113
4.2	Droplet Sizing	118
4.3	Droplet Dispersion Angles.....	121
4.4	Sonic Nozzle Validation	123
5	Challenges	125
5.1	Design Challenges	125
5.2	Experimental Challenges	126
5.3	Global Project Challenges.....	127
6	Summary, Conclusions, Recommendations, Broader Impacts	127
6.1	Summary	127
6.2	Conclusions.....	128
6.3	Recommendations for Future Work.....	129
6.4	Project Broader Impacts.....	130

Appendix A: Flow System Parts.....	133
Appendix B: Images of Flow System Parts.....	135
Appendix C: 2D CAD Drawings.....	140
References.....	145

List of Figures

Figure 1: Commercial Engine under Cruise Conditions (Animagraff 2019)	17
Figure 2: Atmospheric Thermodynamic Conditions as a Function of Altitude Plotted as a Fraction of the Value at Sea-Level (Read 2008)	18
Figure 3: 100-micron Decane Droplet Vaporization Times with Respect to Temperature Differentials of Fluid and Air (Calculations occurred at 1 atm of pressure and 300 K).....	23
Figure 4: Distribution of Spray Droplet Size at Different SMDs (Lefebvre 2010).....	25
Figure 5: Dependence of Viscosity on Temperature (Courtesy of Science Direct 2018)	27
Figure 6: Pressure Swirl Atomizer Schematic (courtesy of Lefebvre 2010).....	28
Figure 7: Minimum Ignition Energy vs. Equivalence Ratio (Khandelwal, 2021).....	32
Figure 8: Graphic for Axis Convention for Nozzle Contour	35
Figure 9: Flow Chart of Design Process	45
Figure 10: Final Flow System P&ID	53
Figure 11: Flow System Calibration P&ID	54
Figure 12: Burner Preliminary Design	57
Figure 13: Rouse Burner Profile Along Length of Burner, Exit Diameter of 20 mm.....	58
Figure 14: Bergthorson Burner Profile Along Length of Burner, Exit Diameter of 20 mm .	59
Figure 15: Gortler Parameter Along Length of Burner, Bergthorson Profile.....	60
Figure 16: Initial Burner Configuration.....	61
Figure 17: Second Iteration of Burner Configuration.....	62
Figure 18: Pressure Vessel Preliminary Diagram.....	64
Figure 19: Hoop Stress at Tested Pressures.....	66

Figure 20: Maximum Working Pressure of A537 and A516 Carbon Steel with an Inner Radius of 17 in	67
Figure 21: Pressure Relief Valve SV805.....	70
Figure 22: Inflow and Outflow of the Vessel	72
Figure 23: Pressure Vessel Design	73
Figure 24: Pressure Vessel Endcap.....	74
Figure 25: Pressure Vessel Window and Holder.....	74
Figure 26: Full Assembly of Pressure Vessel.....	75
Figure 27: Stoichiometric Fuel Calculations Utilizing the Commonly used Domino Method	77
Figure 28: 100-micron Decane Droplet Size versus Time with Respect to Temperature Differentials Between the Fluid and the Flow	78
Figure 29: 100 um Droplet Evaporation Times of Different Fuels and Water.....	80
Figure 30: Parametric Study of Ethanol-Water Solution Estimated Vaporization Times.....	82
Figure 31: Equations Used for Ethanol-Water Solution Study	84
(Terms defined earlier within this section).....	84
Figure 32: Placement of the Modular Atomizer Assembly within the Burner.....	85
Figure 33: Four Meshes Characterized by Element Size.....	88
Figure 34: Outlet Velocity Profile for Optimized Contour for Four Meshes	89
Figure 35: Outlet Axial Profile for Straight, Linear and Optimized Contour at 0.15 m/s Inlet Velocity Boundary Condition.....	91
Figure 36: Outlet Axial Velocity Profile for Straight, Linear and Optimized Contour at 0.45 m/s Inlet Velocity Boundary Condition.....	92

Figure 37: Outlet Radial Velocity Profile for Straight, Linear and Optimized Contour at 0.15 m/s Inlet Velocity Boundary Condition	93
Figure 38: Schematic of 2D Axisymmetric Model Design	95
Used for both COMSOL modelling and hand calculations.....	95
Figure 39: Schematic of 2D Axisymmetric Control Volume Design.....	95
Used for both COMSOL modelling and hand calculations.....	95
Figure 40: Complete COMSOL Heat Transfer Study	97
Figure 41: COMSOL Heat Transfer Study Another POV	98
Figure 42: Temperature as a Function of Pipe Length of Complete Heat Transfer Study, ...	99
Figure 43: Temperature as a Function of Radial Distance of Complete Heat Transfer Study,	100
Figure 44: Coolant System Heat Transfer Model for Coolant System.....	102
Figure 45: Coolant System Temperature Versus Radial Distance of Complete Heat Transfer Study. Each line represents a different cut of the pipe's length starting at the inlet and moving 1 inch each cut. The arrow depicts increasing pipe lengths from the inlet.	103
Figure 46: Coolant System Temperature Versus Pipe Length of Complete Heat Transfer Study,	104
Figure 47: Room Temperature Inlet Model of Temperature Versus Pipe Length	107
Figure 48a: Heat Exchanger Diagram (Wikipedia, "Heat Exchanger").....	108
Figure 48b: Standard Operation of a Vortex Cooler (Wikipedia, "Vortex Tube")	108
Figure 49: Element Size 5×10^{-3} m with Displacement of 0 m on Main Body of Vessel and Internal Pressure of 250000 Pa	109

Figure 50: Element Size 7×10^{-3} m with Displacement of 0 m on Main Body of Vessel and Internal Pressure of 250000 ka	110
Figure 51: Stress Analysis of Element size 5×10^{-3} m with Displacement of 0 m on Main Body of Vessel and Internal Pressure of 250 kPa (Units in Pa)	111
Figure 52: Stress Analysis of Element size 7×10^{-3} m with Displacement of 0 m on Main Body of Vessel and Internal Pressure of 250 kPa (Units in Pa)	111
Figure 53: Equivalent Stress of Pressure Vessel External with Displacement of 0 m on Main Body of Vessel and Internal Pressure of 250 kPa (Units in Pa)	112
Figure 54: Total Deformation of Pressure Vessel External with Displacement of 0 m on Main Body of Vessel and Internal Pressure of 250 kPa (Units in m)	113
Figure 55: Experimental Setup for Particle Image Velocimetry Testing	114
Figure 56: Experimental Setup Featuring the Burner and Laser, Focused by 3 Lenses.....	114
Figure 57: Experimental Setup Featuring Particle Seeder and Flowmeter.....	115
Figure 58: Images Captured with High-Speed Camera.....	116
Figure 59: Open PIV Settings Used to Conduct Analysis.....	116
Figure 60: Open PIV Results for 30 SLPM, 1 kHz	117
Figure 61: Experimental Setup for Droplet Testing	119
Figure 62: 34 Degree Angle of Dispersion at 30 psi	122
Figure 63: 74 Degree Angle of Dispersion at 30 Psi.....	123
Figure 64: Flow Rate Exiting Three Types of Sonic Nozzles under Three Pressure Conditions	125
Figure B1: Atomizer (courtesy of Grainger)	135
Figure B2: Sonic Nozzle (courtesy of O'Keefe Controls).....	135

Figure B3: Mechanical Flowmeter, (courtesy of Brooks).....	137
Figure B4: NPT Connector (courtesy of Swagelok).....	137
Figure B5: Pressure Gauge (courtesy of Omega).....	138
Figure B6: Pressure Regulator (courtesy of Omega).....	139
Figure C1: 2D CAD Drawing for Burner (mm).....	140
Figure C2: 2D CAD Drawing for Flange Endcap in Inches.....	141
Figure C3: 2D CAD Drawing for Window in Inches.....	142
Figure C4: 2D CAD Drawing for Window Holder in Inches.....	143
Figure C5: 2D CAD Drawing for Vessel Body in Inches.....	144

List of Tables

Table 1: Approximate Atmospheric Conditions at Various Altitudes.....	18
Table 2: Typical Combustor Conditions at Various Altitudes	20
Table 3: Boundary Conditions and Parameters for Bergthorson Burner Profile.....	59
Table 4: Mechanical Properties of Possible Pressure Vessel Materials	65
Table 5: Pressure Vessel Dimensions.....	73
Table 6: Fuel Flow Rates for the Minimum Air Mass Flow Rate 0.000038 kg/s	77
Table 7: Fuel Flow Rates for the Maximum Air Mass Flow Rate 0.00038 kg/s.....	77
Table 8a: Time to Reach 10% Loss of Diameter Due to Vaporization of 100 um Droplets (Various Fuels).....	80
Table 8b: Time to Reach 10% Loss of Mass Due to Vaporization of 100 um Droplets (Various Fuels).....	81
Table 9a: Time to Reach 10 % Reduction in Diameter of 100-micron droplets of Different Ethanol Concentrations.....	83
Table 9b: Time to Reach 10 % Reduction in Diameter of 100-micron droplets of Different Ethanol Concentrations.....	83
Table 10: Total Vaporization Times of 100-micron droplets of Different Ethanol Concentrations	84
Table 11: Properties Used for Ethanol-Water Solution Study.....	84
Table 12: Velocity Magnitudes Across the Straight, Linear, and Optimized Contours for Two Inlet Boundary Conditions.....	90
Table 13: Droplets Captured at Various Distances from the Atomizer, Air Pressure of 30 psi, Each Image 1mm x 1mm	120

Table 14: Range of Droplet Sizes at Different Distances from the Atomizer	121
Table A1: Final Flow System Parts Details.....	133
Table A2: Cost Breakdown for Ordered Parts.....	134
Table B1: Air Flow Table for Sonic Nozzles in SLPM.....	136

Authorship

1	Introduction	
1.1	Background and Literature Review	
1.1.1	Relight Conditions	Primary Author: Jonathan Stern Secondary Author: Ethan Davis
1.1.2	Atmospheric and Combustor Conditions	Primary Author: Meena Kodali Secondary Author: Jonathan Stern
1.1.3	Flow Characteristics	Primary Author: Jonathan Stern Secondary Author: John Sirois
1.1.4	Atomizers	Primary Author: Jonathan Stern
1.1.5	Fuel Types	Primary Author: Jonathan Stern Secondary Author: Ethan Davis
1.1.6	Air to Fuel Ratio	Primary Author: Ethan Davis Secondary Author: Jonathan Stern
1.1.7	Experimental Configurations	Primary Author: Meena Kodali
1.1.8	Burner Nozzle Design	Primary Author: Meena Kodali
1.1.9	Particle Image Velocimetry	Primary Author: Meena Kodali
1.1.10	Pressure Vessel	Primary Author: Ethan Davis
1.2	Project Design Requirements	
1.3	Project Goals	
1.4	MQP Objectives and Methods	
1.5	Project Management	
1.6	MQP Gantt Chart	
2	Preliminary Design	
2.1	Experimental Configuration	Primary Author: Meena Kodali
2.2	Laminar Flame Speed	Primary Author: Meena Kodali
2.3	Air Flow Rates	Primary Author: John Sirois
2.4	Fuel Types	Primary Author: Jonathan Stern
2.5	Atomizer Requirements	Primary Author: Jonathan Stern

2.6	Burner Dimensions	Primary Author: Meena Kodali
2.7	Pressure Vessel	Primary Author: Ethan Davis
3	Modeling	
3.1	Air to Fuel Ratio and Droplet Residence Times	Primary Author: Jonathan Stern
3.2	Burner FLUENT Modeling	Primary Author: Meena Kodali
3.3	Fluid Flow Heat Transfer COMSOL Modelling	Primary Author: John Sirois & Jonathan Stern
3.4	Pressure Vessel Analysis	Primary Author: Ethan Davis
4	Experimental Results	
4.1	Particle Image Velocimetry	Primary Author: Meena Kodali
4.2	Droplet Sizing	Primary Author: Meena Kodali
4.3	Droplet Dispersion Angles	Primary Author: Ethan Davis
4.4	Sonic Nozzle Validation	Primary Author: Meena Kodali
5	Challenges	
5.1	Design Challenges	Primary Author: Jonathan Stern and Meena Kodali
5.2	Experimental Challenges	Primary Author: Jonathan Stern and John Sirois
5.3	Global Project Challenges	Primary Author: Jonathan Stern and John Sirois
6	Summary, Conclusions, Recommendations, Broader Impacts	
6.1	Summary	Primary Author: Jonathan Stern
6.2	Conclusions	Primary Author: Meena Kodali
6.3	Recommendations for Future Work	Primary Author: Ethan Davis
6.4	Project Broader Impacts	Primary Author: Jonathan Stern

1 Introduction

1.1 Background and Literature Review

1.1.1 Relight Conditions

Inside commercial jet engines, fuel and air combust, ejecting hot gases and spinning turbines to produce thrust. This combustion begins with a small flame, formed from ignited droplets of fuel in atmospheric air. This little flame faces many environmental challenges throughout its journey. At takeoff, there is not much of a challenge, dense air and warm fuel easily combust within an engine, starting the turbines allowing for takeoff. This initial ignition process is more difficult at different atmospheric conditions. However, an aircraft must be equipped to respond to situations when an engine's flame would have to be reignited swiftly. Relight, as the name implies, is the situation when an aircraft must reignite its engine to continue normal thrust generation (Reed 2008). The need for relight occurs when engines suddenly flame out, typically during cruise. Flameout spontaneously happens during flight with environmental factors greatly challenging engine flame stability. Ice, dust, and water can enter the engine thereby extinguishing the flame. Additionally, disturbances in airflow can contribute to flameout when unintended interactions occur with turbulent air and the combustor. The Federal Aviation Administration (FAA) and European Aviation Safety Agency (EASA) mandates engines must have methods to restart under high-altitude conditions (FAA 2000; EAS 2003 as cited in Reed 2008). The majority of dangerous relight situations occur at the commercial airline cruising altitude of 30,000 feet. As stated above, dense air and warm reagents hold keys to fast flame ignition and stability. The low air density and temperature encountered at 30,000 feet makes reignition difficult. If an engine is unable to reignite after flameout, it may crash. The figure below was added to aid in visual understanding of relight.

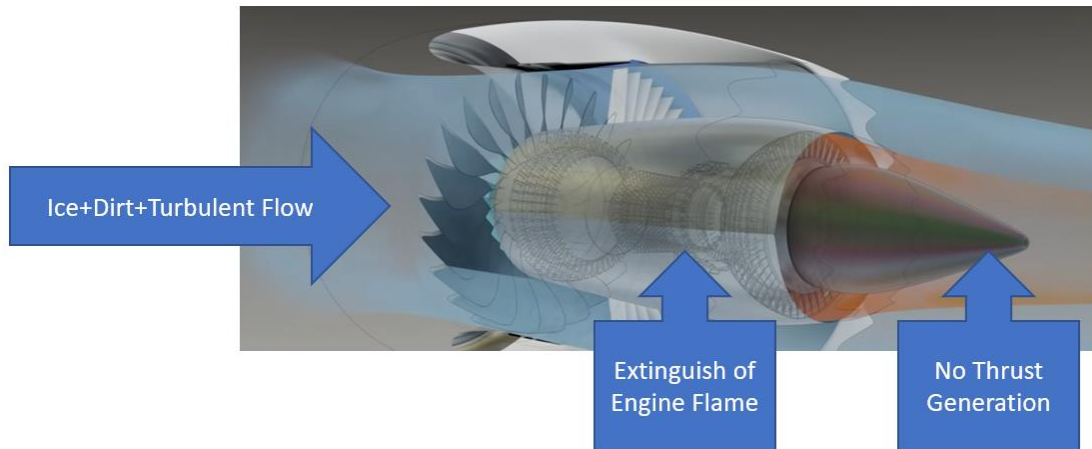


Figure 1: Commercial Engine under Cruise Conditions (Animagraff 2019)

Figure 1 depicts a typical commercial engine which has ice, dirt, and turbulence entering the engine inlet. These disturbances can extinguish the flame. Once the flame has been extinguished, thrust generation significantly drops and turbines slow. Additionally, the engine cools rapidly, causing engine relight to be hampered. At these lower temperatures, fuels ignite less consistently causing dangerous situations to occur.

There exist differing schools of thought regarding relight; some believe relight is limited by chemical kinetics and others focus on the fluid dynamics, evaporation, and mixing. The conditions of high-altitude relight are not easy to recreate putting additional strain on the ability to accurately probe the phenomena of relight at these conditions. When the flame extinguishes, the components of a typical modern commercial engine do not function optimally and thus, especially at high altitudes, distinctions in operating conditions become apparent.

1.1.2 Atmospheric and Combustor Conditions

To begin to study relight conditions, it is important to understand the atmospheric and combustor conditions where flameout typically occurs, at cruise altitudes. The atmospheric

conditions at cruise altitudes, roughly 30,000 ft, are well-documented but can vary depending on the exact location around the world due to local environmental factors. Approximate values for atmospheric conditions at various altitudes can be found in Table 1. Furthermore, Figure 2 depicts values for temperature, pressure, and density as a function of altitude.

Table 1: Approximate Atmospheric Conditions at Various Altitudes

Altitude	Sea Level	15,000 ft	30,000 ft
Pressure	101.3 kPa	57 kPa	25 kPa
Temperature	280 K	256 K	230 K
Air Density	1.225 kg/m ³	0.74 kg/m ³	0.43 kg/m ³

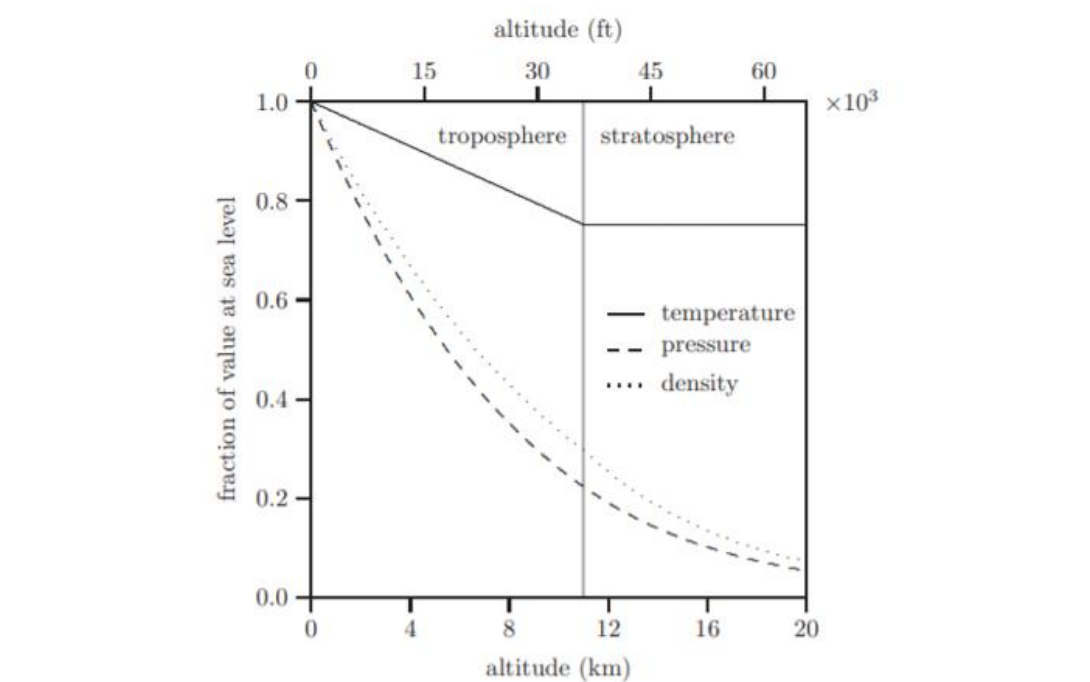


Figure 2: Atmospheric Thermodynamic Conditions as a Function of Altitude Plotted as a Fraction of the Value at Sea-Level (Read 2008)

Knowledge of atmospheric conditions allows for the calculation of the conditions inside an aircraft's combustor (Read 2008). Several assumptions were made regarding the airflow through the engine. The first is that the heat and work transfers are negligible immediately prior to a relight attempt. This assumption is made because after flameout, the engine would rapidly cool, and the spools greatly decelerate; their rotation is maintained only by the ram pressure at the inlet of the compressor. The second assumption is that the combustor inlet temperature is equivalent to the stagnation temperature; this can be assumed because the velocity within the combustor is only a fraction of the flight-speed. Thus, the combustor temperature, T_c , can be calculated through Equation 1 where T_{atm} is the atmospheric temperature, γ is the specific heat ratio of dry air, and M is the Mach number.

$$T_c = T_{atm} \left[1 + \left(\frac{\gamma - 1}{2} \right) M^2 \right] \quad (1)$$

The third assumption is that there is a significant reduction in stagnation pressure between the engine inlet and the combustor. The rotation of the compressor blades causes irreversible, non-isentropic flows causing this reduction by half (Read 2008). Equation 2 is the combustor pressure, where P_0 is the engine inlet stagnation temperature and P_{atm} is atmospheric pressure.

$$P_c = \frac{P_0 + P_{atm}}{2} \quad (2)$$

At the entrance of the high-pressure turbines, the flow through the throat of the nozzle guide vanes (NGVs) determines the total mass flow rate through the engine. The flow through this throat is assumed to be steady, adiabatic, and isentropic. Also, assuming two-thirds of the pressure drop between the combustor and engine exhaust is represented at the NGV, the Mach number at this nozzle throat can be determined, Equation 3.

$$M = \left[\frac{2}{\gamma - 1} \left(\left(\frac{P_c}{P_{throat}} \right)^{\frac{\gamma-1}{\gamma}} - 1 \right) \right]^{\frac{1}{2}} \quad (3)$$

P_{throat} is the static pressure at the throat and can be expressed in terms of the combustion chamber pressure by Equation 4 (Read 2008).

$$P_{throat} = \frac{P_c + 2P}{3} \quad (4)$$

Thus, the mass flow rate through the engine is given by Equation 5 where A is the area of the NGV throat.

$$\dot{m} = AMP_c \sqrt{\frac{\gamma}{RT_c}} \left[1 + \left(\frac{\gamma - 1}{2} \right) M^2 \right]^{\frac{-(\gamma+1)}{2(\gamma-1)}} \quad (5)$$

Utilizing these relations, the combustor conditions at any altitude atmospheric conditions after flameout can be calculated. Table 2 displays typical combustor conditions following a flameout at two separate altitudes at a Mach number of 0.8 (Read 2008).

Table 2: Typical Combustor Conditions at Various Altitudes

Altitude	15,000 ft	30,000 ft
Pressure	60 kPa	40 kPa
Temperature	290 K	265 K
Flow Rate	2.5 kg/s	1.25 kg/s

1.1.3 Flow Characteristics

To characterize the flow inside the combustor, the Reynolds number can be used. The Reynolds number is the ratio of inertial to viscous forces. Conditions upstream will be controlled using a flow controller, however looking downstream this parameter is used to predict whether a flow will be laminar or turbulent. In contrast to the smooth flow and regular path taken by a laminar flow, a turbulent flow is chaotic and results in intense mixing. A Reynolds number below 2300 indicates a laminar flow. A Reynolds number above 3500 indicates turbulent flow. Between these two limits, the flow is transient. Equation 6 shows the relation between the Reynolds number, the density of the fluid, ρ , the flow speed, u , the characteristic length, L (which is often the diameter of a pipe for pipe flow), and the dynamic viscosity of the fluid, μ . Airflow in combustors is typically highly turbulent. But during high-altitude relight, a combustor's flow will have a reduction in its Reynolds number. The flow speed decreases, and the viscosity increases due to the lower temperature and pressures.

$$Re = \frac{\rho u L}{\mu} \quad (6)$$

Another key characteristic of the flow is the dynamics and kinetics of the fuel. Perhaps the most influential differences between relight at standard conditions and high altitudes would be that of fuel dynamics and chemical kinetics. The low pressure and temperature of the surroundings has a large effect on the fuel inside the engines. With the decrease in temperature, the fuel will be cooler and more viscous. This viscosity can greatly hamper the formation of small homogenous droplets that would be present at optimal combustion, post atomization, and this atomization and effects of high viscosity will be discussed further in sections 1.1.4 and 2.4. Larger diameter droplets increase the amount of ignition energy needed to support relight (Lefebvre 2010). The impacts on combustion don't end there, it has also been maintained that larger droplets decrease

the speed of a flame relative to the surface area of the spray, thus increasing the tendency for blowoff (Read 2008).

It can be seen through the D^2 law how droplet diameter affects vaporization and thus combustion time. Since ignition typically occurs with the vapors of a fuel and not the liquid, the amount of vapors surrounding the fuels and the droplet size impact combustion and flame propagation. When a droplet's diameter increases, the time it takes to evaporate increases. The equations governing D^2 law are displayed below, Equations 7-10.

$$d_d^2 = d_0^2 - K_v t \quad (7)$$

$$K_v = \frac{-8(\lambda/C_p)}{\rho} * \ln(1 + B_{h,v}) \quad (8)$$

$$B_{h,v} = \frac{C_p(T_a - T_1)}{Q_v} \quad (9)$$

$$\tau = d_0^2 / K_v \quad (10)$$

In the D^2 law: d_d is the droplet diameter, d_0 is the initial droplet size, K_v is the evaporation rate constant, and t is the time. λ is the thermal conductivity of the gas, C_p is the specific heat constant, ρ is the density, and $B_{b,v}$ is the characteristic heat transfer number. Q_v is the latent heat of vaporization, T_1 is the temperature at the surface of the droplet, while sometimes being the latent boiling point, and T_a is temperature of the far field/atmosphere. τ is the total time it takes for a droplet to evaporate completely.

Figure 3 depicts calculations of droplet evaporation times of the organic compound, decane, found using the D^2 law equations listed above. More information on the calculations can be found in section 3.1. The droplet size is the vertical axis with the horizontal axis being time. The various temperature differentials between the surface of the droplet and the far field can be seen in the legend on the right side. Visualized on the graph is the understanding that droplets will vaporize

much quicker when there is a larger difference in temperature between the air surrounding the liquid and the liquid itself. To support the formation of large droplets which create little vapor, to meet high-altitude relight criteria, a consistent temperature across both liquid and surrounding air must be held relatively close. When a jet engine is working optimally, the temperature difference will be greater enabling vaporization to occur within a second. This can both be explained by an increased vapor concentration surrounding the droplets and the extreme temperature differential between the fuel and the air stream. Even with decane at a temperature difference of 50 K 100-um droplets vaporize within a second as seen on Figure 3. For high-altitude relights the temperature gradient would be smaller since the engine spools cool down and the air inside the combustor cools.

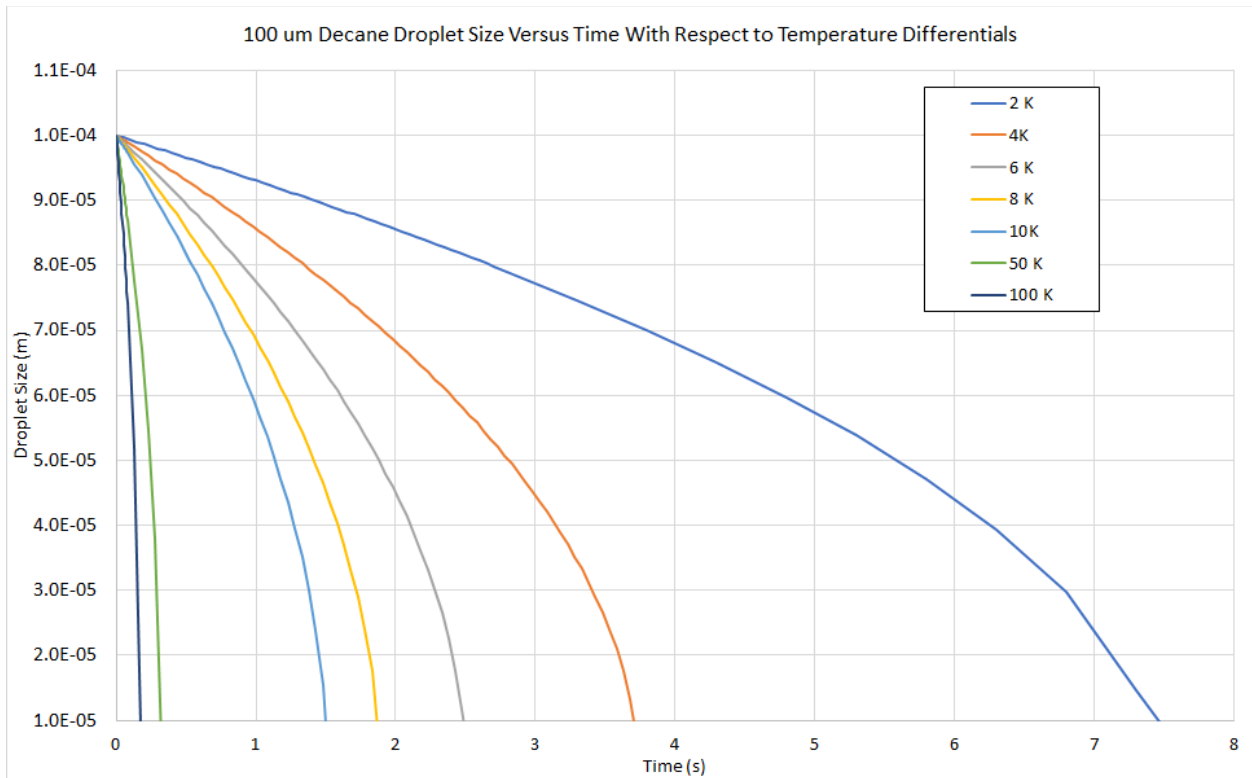


Figure 3: 100-micron Decane Droplet Vaporization Times with Respect to Temperature Differentials of Fluid and Air (Calculations occurred at 1 atm of pressure and 300 K)

Since it is not practical to understand the totality of a complex heterogeneous fuel flow by the diameter of each individual fuel droplet, the Sauter mean diameter (SMD) is often used. This method of quantifying the fuel spray represents the diameter of a droplet with a volume-to-surface area ratio equal to that of the entire spray (Read 2008). This quantification of the entirety of the spray allows researchers to understand the spray dynamics and kinematics more easily. Within a combustor, wide ranges of droplet sizes can occur due to a variety of conditions. SMD allows for a quantitative analysis of where the average distribution lays. Smaller SMDs can correlate with faster vaporization times and thus more consistent faster ignition since the droplets are on average smaller.

$$SMD = \frac{\sum_{i=1}^N D_i^3}{\sum_{i=1}^N D_i^2} \quad (11)$$

Equation 11 is used to calculate the SMD where D_i is the droplet diameter and N is the number of droplets at each diameter. The SMD is a terrific way to understand and quantize fuel sprays, but special care must be taken to ensure that it isn't the only thing considered for size distribution of the spray, it only shows averages of the distribution. As seen in Figure 4, the spray distribution can occur mainly at one droplet size or take place over a greater distribution. In this figure dD over dQ on the vertical axis is the total droplet surface area over the amount of a certain droplet size. Additionally, q is a non-dimensional number that is can be used to describe droplet distributions but is not important in understanding how the same SMD can impact droplet distribution.

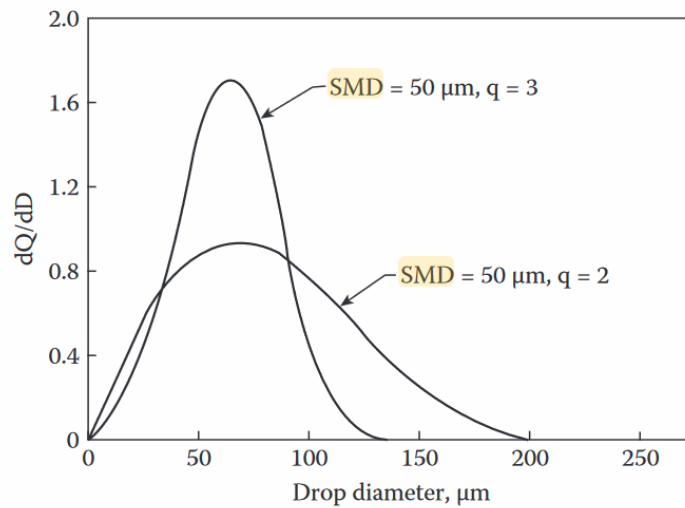


Figure 4: Distribution of Spray Droplet Size at Different SMDs (Lefebvre 2010)

The optimal diameter for fuel droplets is centered around 45 microns (Richards and Lefebvre 1989, as cited in Read 2008). With the largest acceptable droplets reaching 100 microns. In lower pressure and temperature environments, droplets have been seen to be as large as 300 microns wide (Caines 2001, as cited in Read 2008). Pertinent to high-altitude relight, fuel is typically met with cooler temperatures and lower pressures, generating less than optimal droplets.

1.1.4 Atomizers

Breaking liquid fuel into droplets takes many synonymous names, most commonly atomization and nebulizing. The terms atomizer and nebulizer contain a vast number of tools and equipment that all strive to break large volume of fuel into smaller droplets thus making combustion faster. The size of the fuel droplets reacting in a combustion chamber is heavily dependent on the atomizer technique used. Thus, choosing the appropriate atomizer is instrumental in liquid fuel combustion. Smaller droplets evaporate and combust quicker compared to that of larger radius droplets, as seen with the D^2 law. Smaller droplets rely on lower ignition energy to combust, in part due to higher vapor densities surrounding the droplets (Read 2008). During high-

altitude relight, atomizers may not function as optimally due to the higher viscosity of the liquid fuel as well as the lower pressure and temperature oxidizers interacting in the combustion chamber. The non-dimensional Weber number relates disruptive aerodynamic forces to the surface tension and can be used to quantify the effects of viscosity on droplet breakup. When the critical Weber number is reached a droplet will break off, when the aerodynamic drag is equal to the surface tension. To further illustrate viscosities effect on droplet breakup the non-dimensional Ohnesorge number is used. The Ohnesorge number is the square root of the Weber number over the Reynolds number. This division allows viscosity to directly enter the Ohnesorge number through the Reynolds number definition, thus relating viscous forces to the inertial and surface tension forces (Lefebvre 2010). An increased “viscosity is always accompanied by an increase in mean drop size” since droplets break further from atomizer nozzle exits (Lefebvre 2010). Colder reagents additionally need more energy to reach their chemical activation energies. This is due to the higher difference between their temperature and the required energy. The viscosity of a liquid is correlated with the liquid’s temperature, the lower the temperature the slower the liquid flows over itself. And so larger, clumpier, nonhomogeneous droplets appear since atomization occurs further from the nozzle (Lefebvre 2010).

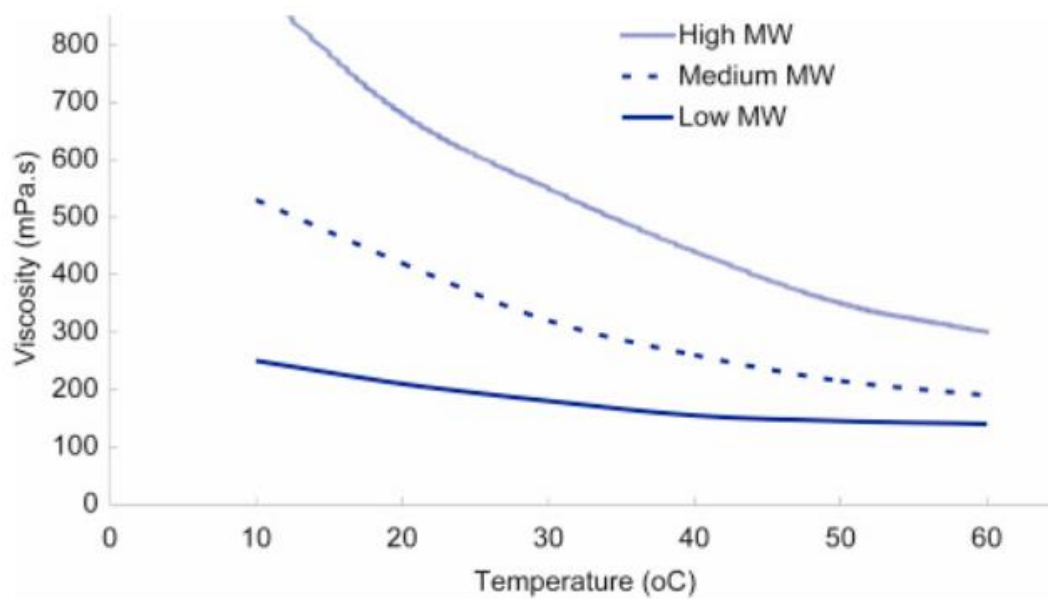


Figure 5: Dependence of Viscosity on Temperature (Courtesy of Science Direct 2018)

1.1.4.1 Pressure-Swirl Atomizer

In a pressure-swirl atomizer, fuel is forced with high pressure through a specially designed opening. This opening is created at a certain angle directed away from the fuel flow and can be compared to the situation when one puts their thumb over a garden hose to spray water droplets further. The fuel flow rate is dependent on the pumped pressure of the fuel and size of the opening. The size of the fuel droplets exiting the atomizer relate proportionally to the size of the exit. One disadvantage with normal pressure-swirl atomizers is the extreme high pressures required to continue optimal atomization when a smaller exit opening is used, making fuel delivery a challenge. However, the reliability and cost of these atomizers can outweigh the disadvantages (Lefebvre 2010). Figure 6 shows a pressure swirl atomizer schematic with pressurized fuel entering with the arrow and exiting out of the orifice.

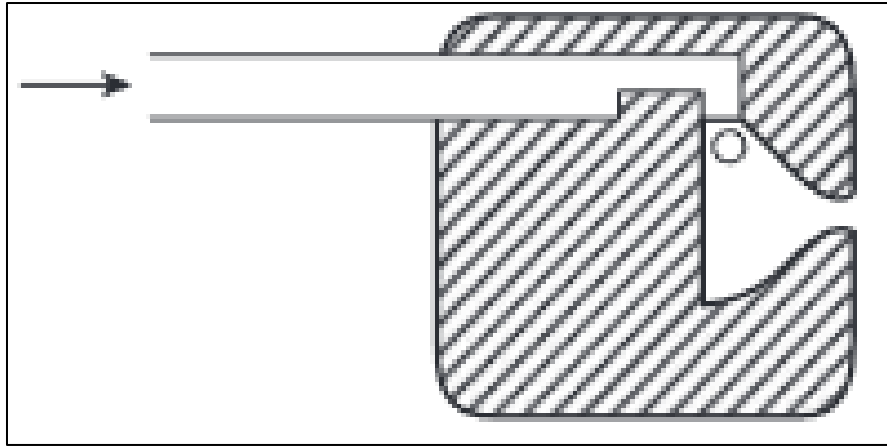


Figure 6: Pressure Swirl Atomizer Schematic (courtesy of Lefebvre 2010)

1.1.4.2 Air-Blast Atomizer

Air-blast atomizers utilize high velocity air streams to atomize fuels pumped utilizing significantly smaller pressure gradients. Air flies over the top of the flow of fuel and carries droplets of fuel to the combustion chamber. The high velocity of the air flow is needed for optimal atomization. Larger physical interaction between the surface of the fuel and the air stream maximizes the potential for atomization. The drawbacks of the air-blast atomizer correlate with the high velocity air stream needed. When an engine starts up, low atomization occurs due to the low air speeds. This brings challenges trying to consistently model relight from the inconsistent startups. The challenges this atomizer faces most frequently can be viewed congruently with what an engines atomizer encounters at relight due to the poor atomization of fuel at low air speeds. Air-blast atomizers do, however, give the benefit of usually creating cooler internal injection line temperatures (Lefebvre 2010).

1.1.4.3 Nebulizers

Nebulizers and atomizers sometimes overlap in roles and definitions. Two main categories of nebulizers exist: air jet nebulizers and ultrasonic nebulizers. Air jet nebulizers are extremely similar to air-blast atomizers. In air jet nebulizers, liquids and gases meet in a chamber in which a

high-pressure gas flows over the inlet of a liquid, generating an aerosolized spray (Meinhard 2021). Another nebulizer is the ultra-sonic nebulizer. Ultra-sonic nebulizers, often used for medical purposes, employ high frequency vibrations to generate an aerosol (WebMD 2021). There is no inherent air flow to carry the aerosol, droplets stay suspended in the air with just an increase in their height relative to the liquid surface. This necessitates an air flow over the top of the fuel if the droplets are to be carried horizontally to a new location.

1.1.4.4 Gaseous Fuels

Gaseous fuels do not require atomization. Modern airplanes overwhelmingly choose to not use gaseous fuel. Gaseous fuels create storage issues for airplanes and typically do not carry the same efficiency bonuses as liquid fuels, mainly related to the size, weight, and storage conditions necessary. Liquid fuel's density allows for a higher amount of energy to be stored, commonly called energy density. Researchers do use simple gaseous hydrocarbons, such as methane, to study a plethora of combustion phenomena. Chemical kinetics of these simple hydrocarbons leads to a better understanding of combustion that can be extrapolated to more complex, longer carbon chain fuels.

Many of the atomization techniques can synergize together and create optimal atomization used in unison. When the complexity of atomizers increases so does that of studying atomization and thus relight. Therefore, single atomization techniques are generally used.

1.1.5 Fuel Types

The characterization of the flow inside a combustor during relight is also dependent on the specific fuel type used. Modern commercial airplane engines typically run off highly refined long chain hydrocarbon fuels. Refined kerosene is the most common jet fuel used today, called Jet-A.

Kerosene itself is a composition of hydrocarbons straight chains, typically 10-16 carbons in length, and aromatic rings. Due to the number of species inside kerosene the complexity of understanding the combustion mechanisms comparatively increases. Researchers occasionally resort to simpler and singular fuel species to study relight and combustion phenomena. In the following sections, a select few fuels will be discussed to understand their individual properties.

1.1.5.1 Methane

The simplest organic molecule is a singular carbon atom covalently bonded to 4 hydrogens. Methane is a gas at sea level conditions as well as high-altitude conditions. Methane easily ignites and is extensively used. The molecular weight is 16.043 g/mol. Its boiling point is -258°F at 760 mm Hg (PubChem 2021).

1.1.5.2 Ethanol

Being a usual additive to fuels, ethanol is a highly studied alcohol. Ethanol consists of two carbons bonded together with 5 hydrogens and an alcoholic group attached to those carbons. It is the second simplest alcohol. Ethanol-water solutions will further be discussed, to express ways of increasing droplet vaporization times. Ethanol has a thermal conductivity of $0.171\text{ W/m}\cdot\text{K}$ and a heat of vaporization of 38.7 kJ/mol . Ethanol's specific heat is $2.57\text{ kJ/kg}\cdot\text{K}$. The molecular weight is 46.17 g/mol .

1.1.5.3 Heptane

Heptane consists of a saturated seven carbon long chain. Its properties can mimic those of more typical organic fuels, such as kerosene. Similar traits derive from the fact that it is a saturated long carbon chain like components found in fuels. The benefits of considering heptane as a fuel for study relate to the simplicity of the molecule.

1.1.5.4 Kerosene and larger chain organic compounds

Kerosene is a highly refined derivative of crude oil composed of large chain hydrocarbons and aromatic rings. The complexity, when compared to simple saturated hydrocarbons, of the aromatic and long carbon ring constituents of kerosene bring about some challenges to experimental study and understanding of high-altitude relight combustion dynamics. Due to the challenges brought from the complexity of kerosene's composite molecules the team decided to additionally study a simple straight chain carbon compound. Heptadecane is a saturated 16 carbon chain whose properties are similar to other straight chain organic fuels. Heptadecane was considered for its longer vaporization times when compared to smaller chain hydrocarbons, this analysis is illustrated in section 3.1. Decane, a 10 carbon long saturated hydrocarbon, was also considered for its increases in vaporization times and similarity to modern fuels.

1.1.6 Air to Fuel Ratio

The air to fuel ratio (AFR) is an important parameter for creating relight and combustion. Having the correct amount of fuel to air will allow relight to occur. If the ratio is off the combustion efficiency will be changed. The equivalence ratio is one of many factors including airflow, temperature, pressure, spark rate, and fuel that affects the minimum ignition energy, the amount of energy required for relight to occur (Khandelwal, 2021). The air to fuel ratio is used to calculate the equivalence ratio. The equivalence ratio is found by taking the actual AFR and dividing it by the stoichiometric AFR. Based on the phase of the fuel and the equivalence ratio the minimum ignition energy will be lower for relight as shown in Figure 7. Figure 7 shows the effects of equivalence ratio and droplet size on minimum ignition energy. The minimum ignition energy is much higher for fuel rich mixtures.

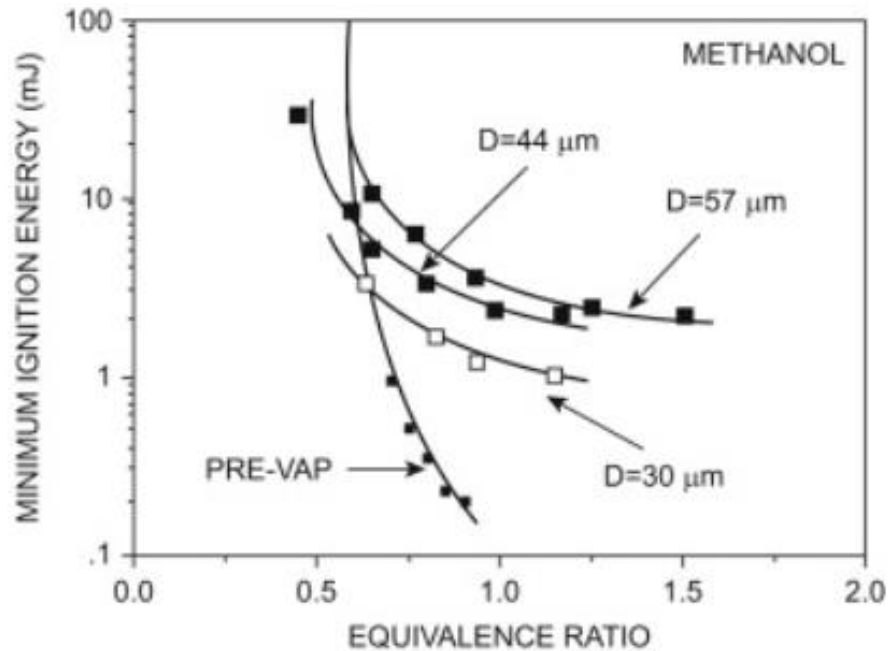


Figure 7: Minimum Ignition Energy vs. Equivalence Ratio (Khandelwal, 2021)

1.1.7 Experimental Configurations

There exists a plethora of experimental configurations to study the ignition and relight of hydrocarbon fuels. One subsection of these configurations, consisting of a flow travelling through a horizontal box chamber, was used extensively by Ballal and Lefebvre (1979) to study ignition and flame quenching. The properties of a wide variety of fuel sprays under both laminar and turbulent conditions were measured and then used to develop analytical models.

Another subsection of these configurations is known as stagnation-point flows (Jarosinski & Veyssiere 2009). They are used due to the simplicity attained from the fact that their flow fields are well defined. Two possible stagnation flow configurations are tubular flows and counterflows. In a tubular flow configuration, the direction of inlet flow is radial while the outlet flow is axial. The counterflow configuration consists of two coaxial opposing jets that meet at a stagnation plane where a flame can be stabilized. These can be premixed, in which both flows consist of a mixture

of fuel and oxidizer. Or they can be non-premixed, also known as diffusion flames, where one flow is an oxidizer while the other flow is pure fuel or diluted with an inert gas. Due to the planar flame in the counterflow configuration, the complications resulting from flame curvature can be minimized significantly compared to the other configurations. Ahmed et al. (2007), Ji et al. (2010), Egolfopoulos et al. (2014), Hayashi et al. (2011), and many others have utilized the counterflow configuration for the simplicity it provides for analysis.

It is important to understand the behavior of the flow leaving the burners, the final section of the experimental apparatus through which the flow exits. A fully developed flow features a parabolic velocity profile. However, a top-hat, or uniform, velocity profile is much simpler to analyze. Although counterflows and free jets are typically dissimilar, for the purpose of understanding the effects of momentum transfer of the exit flow behavior of a counterflow setup with a top-hat exit velocity profile, a free jet assumption is used. Simon et al. (2017) utilizes a differential equation to describe a liquid jet flowing from a circular orifice. The kinematic momentum of the jet, K , is constant along the axial direction and is related to the u , the axial velocity and r , the radial distance from the center of the jet, Equation 12.

$$K = 2\pi \int_0^{\infty} u^2 r dr = \text{constant} \quad (12)$$

Utilizing continuity relations, a momentum balance, stream functions, and applying boundary conditions, the components of the velocity are given by Equations 13-16 where ν is the dynamic viscosity of the fluid, x is the axial distance from the exit of the orifice, η is a dimensionless variable, and c is a constant to satisfy the momentum balance.

$$u = \frac{3}{16\pi} \frac{K}{\nu x} \frac{2}{(1 + \eta^2/4)^2} \quad (13)$$

$$v = \sqrt{\frac{3K}{16\pi} \frac{1}{x} \frac{\eta - \eta^3/4}{(1 + \eta^2/4)^2}} \quad (14)$$

$$\eta = \frac{r}{x} \frac{\sqrt{cK}}{v} \quad (15)$$

$$c = \frac{3}{16\pi} \quad (16)$$

These equations describe the change in the velocity of the jet, u and v , at axial distances directly out of the burner exit, x .

As this jet exits the burner, momentum transfer occurs between the flowing jet and the quiescent medium. At lower pressures, the effect of the momentum transfer invades further into the core of the exiting jet, further minimizing the top-hat velocity profile into a parabolic profile. Utilizing a larger burner diameter at lower pressures ensures that less of the velocity of the core of the jet is affected.

Along with the velocity profile, another feature of the flow that is important to understand is whether it is laminar or turbulent. Although combustor conditions are typically highly turbulent, experimental configurations studying these behaviors often use a laminar flow. One reason for this is to better understand, “the controlling physics of a variety of phenomena that may not be accessible under turbulent conditions” (Egolfopoulos et al. 2014).

1.1.8 Burner Nozzle Design

There are two primary methods to physically create a laminar flow with a top-hat velocity profile exiting the burners. The first is to utilize flow-smoothing devices, such as meshes and glass beads. However, spray droplets can get trapped at these screens, changing the expected air to fuel ratio. The second method is to use a nozzle at the exit of the burner that can disrupt the boundary layers of a parabolic velocity profile and leave a more uniform exit velocity profile (Morel 1975).

The Rouse nozzle profile is one such nozzle contraction that can disturb the flow (Hoghooghi et al. 2016). It is defined by two curves, an internal and external, with a turning point, x_i , at some length along the nozzle. Equations 17 and 18 define the two curves where R is the radius of the nozzle at a distance x along the nozzle. D_s is the diameter of the nozzle outlet, while D is the diameter of the nozzle inlet. L is the total length of the nozzle. Figure 8 is a graphic for visualizing this axis convention.

$$0 \leq x \leq x_i \quad \frac{R}{D/2} = \frac{D_s}{D} - \left[\frac{D_s}{D} - 1 \right] \frac{(x/L)^3}{(x_i/L)^2} \quad (17)$$

$$x_i \leq x \leq L \quad \frac{R}{D/2} = 1 + \left[\frac{D_s}{D} - 1 \right] \frac{(1 - x/L)^3}{(1 - x_i/L)^2} \quad (18)$$

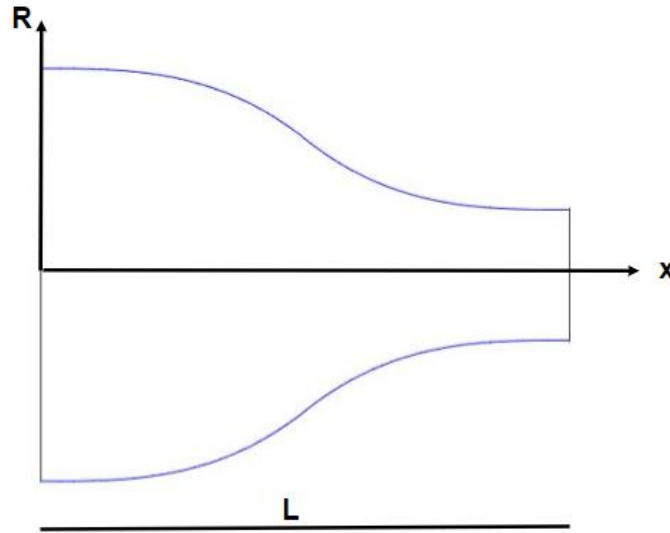


Figure 8: Graphic for Axis Convention for Nozzle Contour

The Rouse profile, although it has been used by other works, is not backed with theory, but rather with experimental trial error. To utilize an approach grounded more in theory as well as practice, another nozzle design was also considered, the one developed by Bergthorson (2005).

When designing a nozzle contraction, it is important that the formation of Taylor- Görtler vortices in the concave section is minimized (Bergthorson 2005). The Gortler parameter, Equation 19, can be used to understand the formation of Taylor-Gortler vortices. Re_θ is the momentum thickness Reynolds number, similar to the typical Reynolds number except that the characteristic length is the momentum thickness of the flow where θ is the momentum thickness. r'' is the second derivative of $r(x)$. These vortices are formed by instabilities in boundary layers experiencing concave curvature. By minimizing this parameter to be below 50 for the entire length of the contraction nozzle, it can be assumed that vortex formation is minimal.

$$G = -Re_\theta^2 \theta r'' \quad (19)$$

$r(x)$, is assumed to be a seventh-degree polynomial to give enough freedom in describing the contraction. Equations 20-23 detail the boundary conditions and parameters utilized to define the nozzle. r_0 and r_e are the radius at the inlet and exit. x_e is the length of the nozzle. r_1 , r_2 , x_1 , and x_2 are parameters that are altered to adjust the profile.

$$r(0) = r_0 \quad r(x_e) = r_e \quad (20)$$

$$r'(0) = 0 \quad r'(x_e) = 0 \quad (21)$$

$$r''(0) = 0 \quad r''(x_e) = 0 \quad (22)$$

$$r(x_1) = r_1 \quad r(x_2) = r_2 \quad (23)$$

An axisymmetric Thwaites approximation (White 1991) is used for the estimation of the momentum thickness, θ . An initial guess for the momentum thickness is given, 0.5 mm and inlet velocity are chosen such that the nozzle exit velocity would be the desired exit velocity using mass conservation. Equation 24 is that of momentum thickness as given by White (1991).

$$\theta^2 = \frac{0.45\nu}{r^2 U^6} \int_0^z r^2 U^5 dz \quad (24)$$

Using the initial guess for the momentum thickness, θ , the kinematic viscosity, ν , the initial radius, r_0 , and the initial velocity, U_0 , the integral term in Equation 25 can be found. This integral term is held constant across the entire analysis and represents the behavior of the flow before entering the nozzle. Knowing the initial estimates of the momentum thickness along the nozzle, the displacement thickness, δ^* , can be found, Equation 26 where $H(\lambda)$ is calculated using Equation 28.

$$\delta^* = H(\lambda)\theta \quad (25)$$

$$H(\lambda) = \begin{cases} 2.0 + 4.14z - 83.5z^2 + 854z^3 - 3337z^4 + 4576z^5, & \lambda \leq 0.25 \\ 2.0, & \lambda > 0.25 \end{cases} \quad (26)$$

$$z = 0.25 - \lambda$$

λ the Holstein-Bohlen parameter is calculated using Equation 27.

$$\lambda = \frac{\theta^2}{\nu} \frac{dU}{dx} \quad (27)$$

$\frac{dU}{dx}$ is assumed to be the same as $\frac{dA}{dx}$, the change in the area of the nozzle. The displacement thickness is used to calculate a new flow area at each location along the nozzle. With this new area, a new velocity is found using conservation of mass. With these values, the Taylor-Gortler parameter is calculated along the length of the nozzle. If this parameter is kept below 50 for the entire length of the nozzle, it can be reasonably assumed that the flow is relatively smooth and free of vortices.

1.1.9 Particle Image Velocimetry

Particle image velocimetry is an experimental technique used to visualize flows (Atkins, 2016). This technique is used later to characterize the flow exiting the experimental apparatus. Particles are seeded into the flow to provide a reference to measure the flow. A thin laser sheet is shone through the flow which scatters off the particles and indicates the positions of these particles.

It is assumed that the movement of the particles is the same as the movement of the surrounding flow. The determination of the velocity field depends on capturing a minimum of two images of the random particle pattern in the flow, calculating the displacement of the particles, and dividing by the time interval. A key advantage of this indirect, nonintrusive measurement method is the ability to capture the velocity vectors for the entire field at once.

With this technique, it is important to sync the operation of the laser and camera, especially at higher speeds. Another important factor is the camera exposure time. A longer exposure time leads to clearer indications for the positions of the particles. However, if particles undergo considerable displacement during this exposure time, rather than distinct particle placement, the image will depict streaks. A separate technique, particle streak velocimetry (PSV) can be conversely used to analyze streaks.

1.1.10 Pressure Vessel

A pressure vessel is important in recreating the thermodynamic conditions relevant to relight. A pressure vessel is a container designed to house the experiment at a pressure different from the ambient pressure. The most important aspects for a working pressure vessel are the materials that compose the pressure vessel and the design of the vessel. If the material has a lower maximum pressure threshold or a lower maximum hoop stress than the pressures, it is being used at then the pressure vessel will fail. Yield strength is the maximum stress the vessel can reach without causing permanent deformation. In a cylindrical pressure vessel, the strongest stress on the vessel is hoop stress. Hoop stress is the stress exerted along the circumference of a cylindrical vessel and accounts for almost all the stress exerted on the vessel (Sinclair and Helms, 2015). Hoop stress increases as the pressure in the vessel increases. This relationship is key when figuring out the max pressure the vessel can hold. The other main stress is longitudinal stress. This stress is

exerted down the barrel of the cylindrical vessel and is negligible when accounting for yield strength because it is so much smaller than hoop stress in a cylinder. The following equations, 28 and 29, can be used to find the hoop stress, σ_θ , of a material at a specific pressure (p), thickness (t), internal radius (r), and joint efficiency (E). Joint efficiency is the rating given to the joints in a pressure vessel after the welding is completed. A minimum joint efficiency of 0.7 is required for the vessel to pass inspections so 0.7 is assumed for the joint efficiency for the equations.

$$\sigma_\theta = \frac{p(r + 0.6t)}{tE} \quad (28)$$

$$p = \frac{\sigma_\theta t E}{(r + 0.6t)} \quad (29)$$

Geometry of the vessel is also important for the project it is being used for. Pressure vessels are designed in spherical and cylindrical forms. Even though cube vessels would be easier to pack in a smaller area, spherical vessels are used in tighter space and mass constrained projects that need to integrate with other systems such as being used as a fuel tank for a rocket. A spherical vessel is used because the pressure in a spherical or cylindrical vessel is distributed equally on the walls of the vessel unlike that of a cube vessel. A spherical tank holds more volume in a lighter and smaller amount of material. Cylindrical vessels are used for larger storage and for larger projects that do not have the constraint of space. Cylindrical vessels are larger and can have more input and integration for the experiment we are trying to design. Furthermore, the stresses exerted for a spherical vessel are distributed equally across the entire circumference because of the shape of the vessel. Spherical vessels can hold higher pressures, but cylindrical vessels are cheaper to manufacture.

When deciding the material to make the pressure vessel, tensile strength is the most important factor in the decision. Steel alloys, aluminum, and plastic are the materials typically

used for pressure vessels. Plastic is used for low pressures and has low tensile strength. Aluminum is a newer material that can be used and can have higher tensile strength by using special welding techniques. However, these techniques are usually more expensive, and the durability and longevity of the material is questionable. Steel alloys are very strong contenders as they have the best properties of the materials, they are composed of but are usually much more expensive than the alternatives. Two specific alloys, carbon steel and stainless steel, are two great materials. Both have great longevity and corrosion and chemical resistance because of the properties of the materials. Furthermore, they both have high tensile strengths which is integral to the design of a pressure vessel. Stainless steel is typically used in vessels planned to be outdoors because material is excellent against the environment but can be used indoors too.

Pressure vessels are normally thin walled because having a thick-walled pressure vessel is unnecessary, impractical, and expensive. A thin-walled pressure vessel is defined as having a thickness that is at less than $1/5$ the internal radius of the vessel. Thin-walled pressure vessels have a lower maximum allowable pressure than a thick-walled pressure vessel. When wall thickness decreases the maximum allowable pressure also decreases. For example, a pressure vessel with 1-inch-thick walls, a 12-inch inner radius, hemispherical end caps, a minimum joint efficiency of 0.7, and made of A537 or A516 carbon steel has a maximum allowable pressure of 3907 psi. However, the same pressure vessel with a wall thickness of 0.5 inches has a maximum allowable pressure of 2001 psi. The same affect also occurs when the inner radius is increased for the pressure vessel. All the factors laid out in this section are integral to the design of the pressure vessel for this experiment.

1.2 Project Design Requirements

- The pressure vessel must recreate relight conditions and sustain a pressure difference from 0.5 atm to 10 atm
- The burner must create a laminar uniform flow that matches the flame speed of a chosen fuel. The ranges are from 40 to 100 cm/s
- The flow system must deliver uniform air at a temperature consistent with relight conditions (265 K)
- The spray system must deliver minimally vaporized fuel that is somewhat comparable to droplet sizes at relight (3 to 300 μm)

1.3 Project Goals

The goals of this project are:

- Develop a design for an experimental apparatus to understand the effect of atmospheric and fuel conditions on the success of relight
- Improve and validate the design through fluid, thermal, and structural analyses
- Construct the experimental apparatus based on the predetermined design
- Conduct a series of tests to validate the designs and enable the study of ignition and flame propagation at relight

1.4 MQP Objectives and Methods

- Design an experimental apparatus to study the phenomenon of relight at realistic atmospheric conditions
 - Fuel spray droplet size and distribution, pressure, and temperature will be individually varied to understand their effect on the success of relight

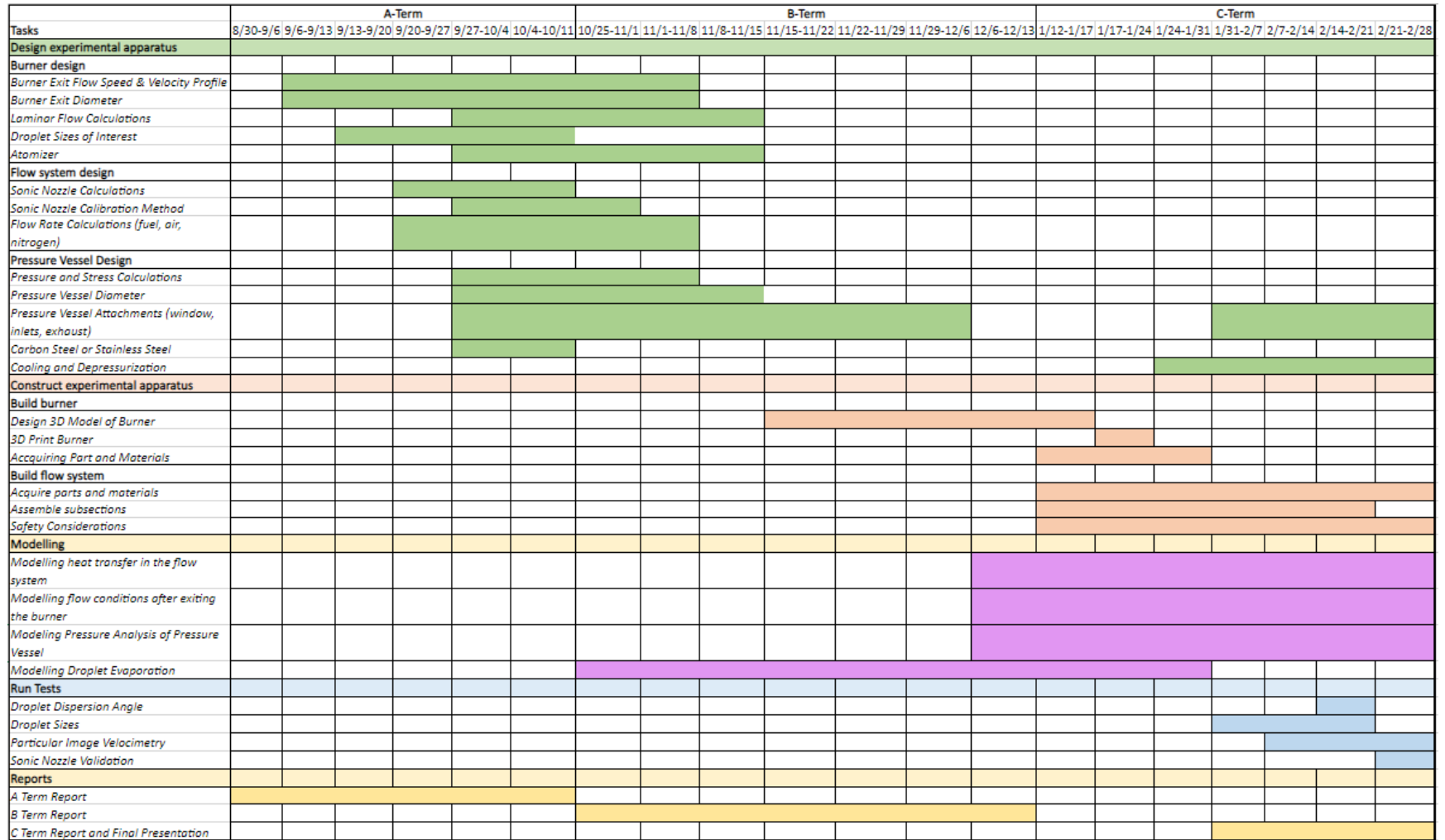
- Conduct structural, fluid, and thermal analyses
 - Model the structural loads experienced by the pressure vessel in ANSYS
 - Model fluid flow exiting the burner in FLUENT
 - Model the heat transfer of the air flow to ensure the correct temperature conditions at the burner exit in COMSOL
- Construct the experimental apparatus
 - Correctly source parts that will integrate with the design and manufacture necessary hardware
 - Use the modeling analyses to validate and compare to the experimental configuration
- Conduct a series of tests on experimental configuration
 - Validate the flow systems operation
 - Validate the atomizer spray angle and droplet sizes
 - Validate that the flow of the burner converging section is uniform, laminar, and matches the model
 - Integrate subsystems into a functional apparatus
 - Validate test configuration with flame ignition

1.5 Project Management

To undertake the design of the experimental apparatus, each member was tasked with leading the design of one subsystem. Ethan Davis oversaw the pressure vessel design. Meenakshi Kodali was responsible for the burner design. John Sirois handled the design and implementation of the flow system. Jonathan Stern oversaw the spray system design while accounting for vaporization physics.

The modeling aspects of the project were undertaken by the team member(s) whose subsystem was most relevant to that model. Ethan Davis conducted the structural analysis of the pressure vessel through ANSYS. Meenakshi Kodali modeled the exit flow conditions in FLUENT. John Sirois and Jonathan Stern studied the heat transfer in the flow system with COMSOL.

1.6 MQP Gantt Chart



2 Preliminary Design

During the design process, a flow chart was created to showcase interdependencies and lead the decision-making process in the preliminary design. This flow chart is shown in Figure 9. The first step of the design process for the experimental apparatus was to identify the exit velocity of the burner. This is entirely dependent on the laminar flame speed of the mixture being studied, which depends on the fuel. Once a specific fuels flame speed is documented that speed can be used to compute differing air mass flow rates throughout the burner, the dimensions of the burner outlet can then be chosen to match the desired conditions. Then, knowing these parameters, air mass flow rates can be decided. Fuel mass flow rates are decided based on the expected air to fuel ratios. These flow rates dictate the equipment that can be used, such as the flow metering devices and the atomizer. The droplet dispersion produced by the chosen atomizer decides the rest of the dimensions of the burner, like its length and inlet diameter, and the dimensions of the pressure vessel. The rest of this section goes into further detail regarding the design choices for the experimental apparatus.

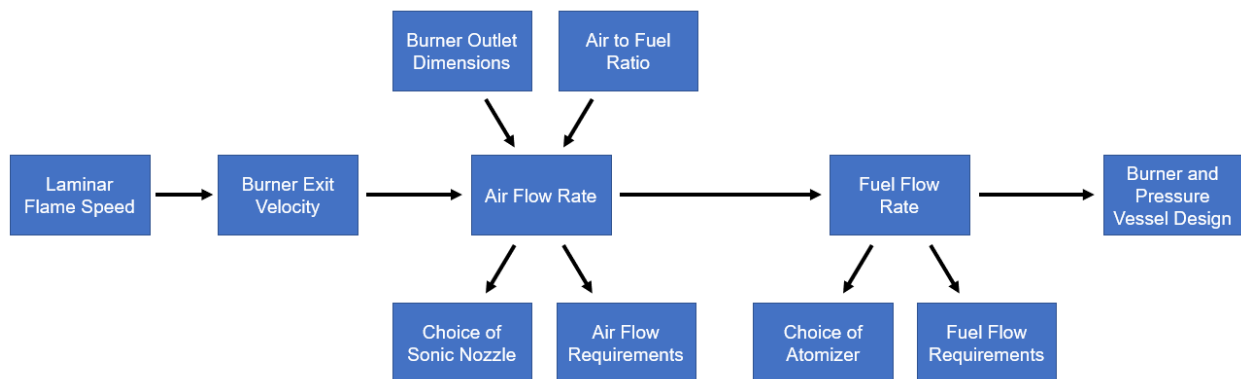


Figure 9: Flow Chart of Design Process

2.1 Experimental Configuration

Although flow conditions within combustors are turbulent, to simplify data collection and analysis, it has been decided that a laminar flow will be studied. Of the possible experimental configurations, a counterflow configuration was chosen. In counterflow configurations, there is great optical access and ready access for instrumentation. Additionally, the comparison between theory and experiment is simplified because conservation equations are reduced to ordinary differential equations which be easily numerically analyzed (Li et al. 1992). Heat losses are also minimized (Darabiha et al. 1993). And lastly, both premixed and non-premixed modes are easily interchangeable (Niemann et al. 2014).

2.2 Laminar Flame Speed

As discussed in earlier sections, as a jet exits a circular orifice, the jet's radial spread increases and axial velocity decreases. Flame stabilization is dependent on the fuel's laminar flame speed. Methane's laminar flame speed is 35 cm/s at the stoichiometric air to fuel ratio (Egolfopoulos et al. 2014). The exit velocity profile of the jet exiting the burner was chosen to be that of a top-hat velocity profile to simplify calculations. Heptane, similarly, has a laminar flame speed of roughly 40 cm/s (Shi et al, 2017). And lastly, kerosene has a laminar flame speed around 60 cm/s (Wu et al. 2018).

To verify that these flows will remain laminar, the Reynolds number was calculated. The equation can also be represented as $Re = UL/\nu$, where U is the average burner exit velocity, L is the burner inner distance, and ν is the kinematic viscosity (Niemann et al. 2014). The Reynolds numbers of air resulting from the flows used for the experiment at ambient conditions are calculated. For an exit velocity of 45 cm/s, the Reynolds number is 576. For 100 cm/s, the Reynolds number is 1280. Both are well within the threshold for laminar flow. Values higher than

the exact laminar flame speeds of the fuels were chosen to ensure complete stabilization of the flame.

2.3 Air Flow Rates

2.3.1 Air Flow Control

Once the necessary exit velocities are known, it is key that the experimental apparatus can control such a flow. A sonic nozzle was desired for controlling mass flow in this experiment as it is relatively cost effective and has no moving parts which renders it very accurate. A sonic nozzle is a flow meter which restricts and chokes the flow of a gas. In a choked flow, the downstream pressure and flow conditions are not transferred upstream. Thus, the sonic nozzle can create a constant volumetric flow rate, independent of downstream conditions. The sonic nozzle also is drastically cheaper, varying upwards of hundreds of dollars cheaper than the controllers. Its accuracy is also consistent over time which allows for great repeatability of tests. Companies often rate their sonic nozzles with the flow coefficient, C_v .

Additionally, to calibrate the sonic nozzle, a mechanical bubble meter was selected. A mechanical flowmeter is a flow calibration device that has a ball trapped within a cylinder. This ball will rise to a level correlating with the amount of gas flowing through it. This ball starts at the bottom of a cylinder and as gas is released through a tube the pressure causes the ball to make its way up the cylinder which is marked. Knowing how far the ball moves in a measured amount of time at a certain pressure allows one to determine the flow rate of the gas. The same considerations were taken in choosing a calibrator. A Drycal Piston, while slightly more accurate, would additionally cost hundreds of dollars more, making it an unnecessary addition to the experiment. This bubble-meter can help calibrate to about 0.25% accuracy. This is an incredibly

small margin of error and would mean the team would be receiving consistent results throughout the experiment.

We then chose what size sonic nozzles we wanted to use based on the flow rates of air we would expect. The range of outlet velocities necessary is from 45 cm/s to 100 cm/s, dependent on the laminar flame speeds for each of the fuels. These are necessary for two different burner outlet diameters, 10 mm and 20 mm, for different pressure conditions. Mass flow rates were calculated using principles of mass conservation to find the required sonic nozzle sizes, Equation 30. A minimum air flow rate of 0.000038 kg/s and a maximum of 0.00038 kg/s were thus found.

$$\dot{m} = \rho VA \quad (30)$$

With this information, the team ordered six precision metal orifices from O'Keefe Controls Co. Each of these parts was a different size spanning across the entire range of flow rates required. This was done to allow the team to change and test at different flow rates while still operating within the higher, and therefore better operable, pressure range for each nozzle. With this array of nozzles, the group could also test with different gases if they desired and still have the proper size for the pressures that would be tested with.

2.3.2 Flow System Design

When looking to put together our flow system to properly transfer air and fuels to the ignition zone at the appropriate velocity, several considerations came into play. First off what equipment would be needed to accomplish this task and to ensure that our expected conditions were met. Secondly, each part had to be rated for conditions related to ours for greater accuracy, we then had to determine how to connect all of them in the appropriate manner, and at an appropriate price considering budgetary restrictions. While material selection could vary between items, we made

sure everything was one quarter inch. Compression fittings and NPT (National Pipe Threading) fittings were used to connect various parts and assemble the flow system.

For both our air and gaseous fuels we would have tanks containing large volumes of each which we would need to release the appropriate fixed flow rate to maintain a steady state system. To restrict and change the pressure of the various gases we needed to obtain a pressure regulator. This item can be viewed along with all others in Appendix B. For this piece of equipment, we went to Omega and searched through their catalog. The company site was relatively limited with regulators that had handles to turn to adjust pressure. These regulators take a high amount of gas and pressure through its inlet, then open or narrow its outlet to allow gas to pass through at a controlled pressure. We found a regulator that had at least our maximum desired pressure of 100 psi and that was also reasonably priced at \$108.82 compared to others which were both more expensive and could only handle half of our desired pressure. The regulator would help us set the pressure well upstream of our other parts and allow us to control the flow rate.

While having the regulator was a good first step, it would be very unreliable without knowing what the pressure at its outlet would be. Therefore, the next piece of equipment we looked to obtain was a pressure gauge. For this we also went to Omega, and this time we had a much larger selection to choose from. The first one was to get a digital gauge. While this meant that it would cost more, it also meant that we would be getting significantly more accurate readings as we would not have to account for human error such as in the analog options that were available. Since we didn't require alarms or shut-off functions, we were still able to save some money by choosing a gauge that had basic zeroing and digital read out functions. Looking at the remaining options, only a couple were designed for our range of pressures. Essentially, by choosing an item made to read 100 psi instead of one made to read upwards of 300 psi, we could expect more consistency in the

and accuracy of our readings. Uncertainty is scaled based on the range of the team's measurement device and made to the smallest available increment of measurement. We ended up going with a model that cost \$121.24 which was one of the cheaper options while still meeting all our requirements and having the proper connectors.

Tubing transfers the gases from the gas supply all the way to the burner and became our next focus. We looked through a few different options. While some options like metal tubing would be very safe and more than strong enough for our tests being good for pressures upwards of 15,000 psi, it also would require precision to cut and bend to the appropriate lengths and turns. This would make using it much more difficult than other options like flexible tubing. The group found PVC plastic tubing at a quarter inch diameter that was rated for 250 psi meaning that it would be more than safe enough for our testing. This tubing also advertised a mesh pattern which we had to double check was embedded in the plastic. This was to ensure an uneven surface wouldn't mess up the compression seal by allowing air to escape when we went to connect the tubing to other devices and cause a leak or malfunction. This plastic tubing costs \$0.84 a foot, which considering the distance our setup in the lab would need to cover, was more than justifiable to have strong tubing we could rely on at hand.

Following our path down the system toward the converging nozzle the next device we would need is a sonic nozzle. For these we were in contact through phone calls and emails with O'Keefe Controls Co. discussing their precision metal orifices. Through calculations we were able to determine our maximum and minimum air flows at assumed atmospheric standard pressure (calculated in SLPM). In these calculations, our team took our mass flow rate and divided it by density, at the correct conditions and units to get the volumetric flow. More detail on the mass flow rate calculations and their relationship to burner diameter can be viewed below. The

maximum and minimum flow rates correspond to our team's maximum and minimum burner outlet diameters and desired velocity. This allowed us to see the range we would need to cover when looking at various nozzle sizes. We wanted to make sure that we chose a range of sizes so that we could test various SLPM (standard liters per minute) values at ideal pressures for the top ranges of the nozzle (100 psi) which would allow for ease while testing. For air we ended up choosing four assorted sizes including orifices with diameters of 0.022 in, 0.017 in, 0.012 in and 0.009 in. A table of values relating to pressure and size can be found in Appendix B. Then for gaseous fuel like methane we chose smaller diameters of 0.011 in and 0.004 in. O'Keefe's website displayed the necessary information to understand how their sonic nozzles sizes relate to expected output flow, and each of these nozzles would cost \$29.95. Since these nozzles are composed of stainless steel, higher safety and pressure ratings were achieved when compared to the same parts made of brass. This and the low price compared to other flow controllers allowed us to purchase multiple nozzles to test at various upstream conditions. Although O'Keefe depicts the ability to lower the inlet pressure by a large margin, we could only lower it so much before our inlet and outlet pressure ratio does not match the typical sonic nozzle requirement of 1.4. This would cause the flow to no longer be choked going through these specific nozzles and affect our flame speed and other aspects later down the line.

Now while we know what the nozzles are rated for, we still want a way to calibrate them to confirm that we know how they're working, especially when changing the temperature of the gas or even what gas we're using. We then searched for a mechanical flowmeter and the search for an accurate meter was difficult as there weren't many made for lower flow rates. Having them rated for significantly higher flow would mean that they wouldn't be quite as accurate for our use. Furthermore, we had the issue of when we did find the appropriate flow rating, the meter would

be made for significantly lower pressures (50 psi) than what was expected within the pipe. In the end we found a series of three flowmeters from Grainger that would cover different ranges we were hoping to test in that way we could use whichever was more appropriate for the test at hand. The average cost of these meters was around \$70, which was a standard for the cheaper ones or else the price jumped way beyond our range. Each mechanical flowmeter would be attached downstream of the sonic nozzle, we'd essentially start a test and adjust the pressure to confirm the flow throughout the sonic nozzle we wanted, then remove the bubble meter and attach the tubing to the inlets and conduct the actual test.

The last part we had to find was the connectors to attach all the above-mentioned devices and tubing. For this we went to Swagelok and looked for compression fittings with NPT connectors as all the above devices had been selected with that attachment port in mind to ensure everything would fit together with ease. These would all be a quarter inch, and we had some flexibility here between materials. We had to have some stainless-steel connectors for any devices that were also stainless steel, like the nozzles and the pressure gauge. The reason for this is matching up stainless steel with brass could strip the brass threading and render the connectors useless. Otherwise, brass connectors are strong enough and cheaper to order so we would be able to be more economically efficient in this area. Most of our connectors were typical straight connectors simply connecting two parts. For example, tubing could be connected to the nozzle then the nozzle back to the tubing, through the sole use of straight connectors. However, for places like the gauge and splitting the air flow to two separate inlet areas we would need tee connectors. The gauge that we had earlier chose had a steel male NPT threading, so a female stainless-steel connector was required to keep the flow going and allow us to obtain pressure readings at the same time. The tee to split the air, however, being located on its own and only having contact with the tubing could be brass. The

stainless-steel tee was slightly more expensive, so this was a good place for us to switch and save some money. Additionally, not all the devices had male NPT threads, some had female and would require male connectors which could essentially be obtained by removing a nut from one (or both sides) of female connectors. This was helpful as the website didn't sell quarter inch diameter male connectors. The brass tee cost \$18.59 and the steel cost \$41.58. The straights cost \$21.12 for steel and \$9.46 for the brass.

P&ID diagrams, Figures 10 and 11, are displayed below for the experimental setup and the calibration. A combined part list and pictures of each of the final parts can be seen in Appendices A and B.

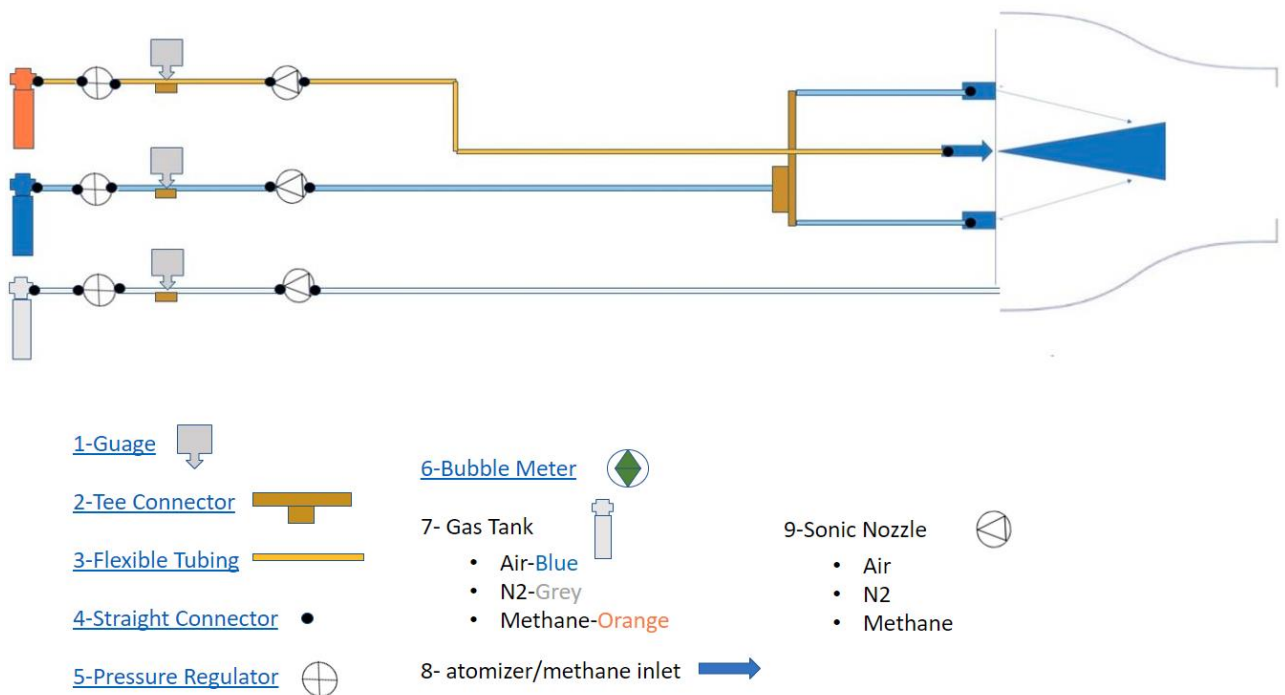


Figure 10: Final Flow System P&ID

Calibration

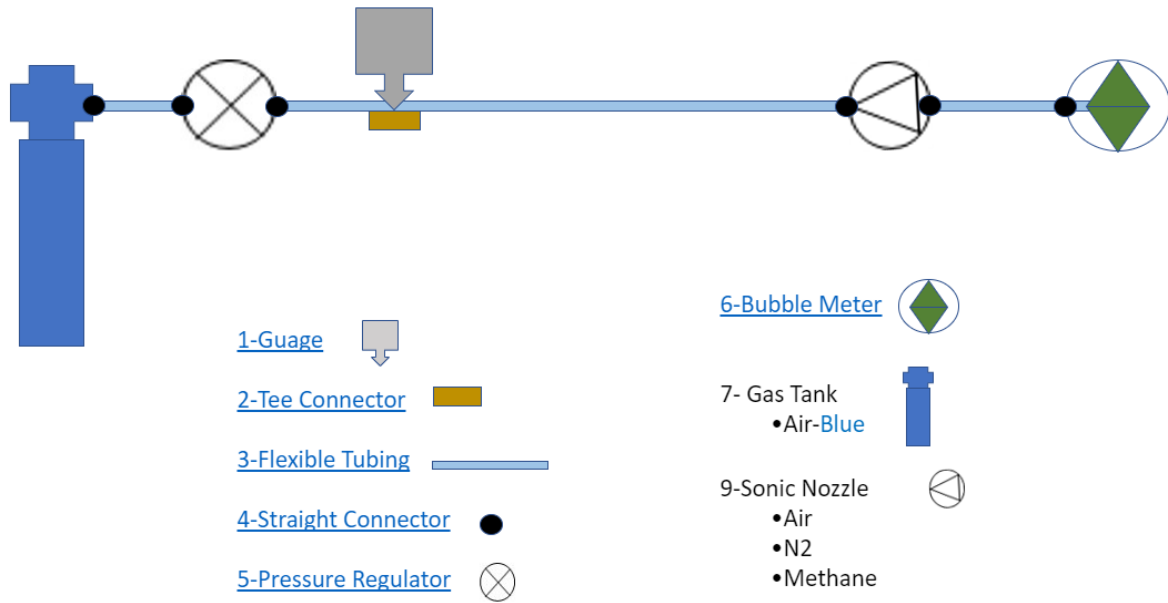


Figure 11: Flow System Calibration P&ID

2.4 Fuel Types for Testing

This section details the rationale in deciding which fuel types to plan to test to best understand the phenomenon of relight. The methodology for calculating specific air to fuel ratios can be found in modelling section 3.1. Theoretical fuel rates can also be viewed in that section. These items were placed in that section to better understand the following droplet modelling.

2.4.1 Methane

The choice to test methane was an easy one. Methane is the simplest hydrocarbon and a well-studied fuel. Methane is inexpensive and readily available. Methane's chemical properties are well understood, and its safety hazards have been studied. An air to fuel ratio of 17.19 to 1 is ideal for relight. The team plans to start with the molar stoichiometric AFR of 9.52. The theoretical maximum flow rate is 1988.58 mL/min. This is using the standard density of 0.55 kg/m³.

2.4.2 Heptane

Heptane is a great fuel for this experiment as well. Heptane is a saturated hydrocarbon, so its combustion results are easier to interpret than longer unsaturated hydrocarbons. An air to fuel ratio 15.2 to 1 is ideal for relight. The team plans to start with the molar stoichiometric AFR of 52.36. The theoretical maximum fuel rate is 2.197 mL/min. This calculation used a density of 684 kg/m³.

2.4.3 Ethanol

Ethanol became a fuel to consider once the droplet lifetime modelling was compared to saturated hydrocarbons. Ethanol boasts a relatively longer vaporizations times compared to that of heptane, detailed in section 4.1. It was still not the most optimal to recreate the vapor poor conditions of high-altitude relight. However due to its miscibility in water from hydrogen bonding, the team can create aqueous ethanol solutions to maximize the droplet lifetime. The other saturated hydrocarbons will not form these mixtures. This increase in vaporization time was still less than diluted ethanol water solutions forcing the decision of which aspect of high-altitude relight this study would focus on, a more realistic fuel or droplet suspension times. The team plans to start with the molar stoichiometric AFR of 14.28. The theoretical maximum fuel rate is 3.213 mL/min. This calculation used a density of 789 kg/m³.

2.4.4 Kerosene

The choice of kerosene was additionally straightforward. Most modern aircraft use liquid fuels. Many of those liquid fuels constitute forms of kerosene, creating an optimal situation to best recreate and model true high-altitude relight conditions. An air to fuel ratio of 15.6 to 1 is ideal for relight. The team plans to start with the stoichiometric AFR of 9.52.

2.5 Atomizer Requirements

As discussed in the section 1.1.3, droplets previously have been detected reaching over 200 microns wide – in similar experimental setups. Most of the available research has been done on droplets ranging from 3 to 110 microns. The experimental setup will thus ideally feature droplets in this range while creating the possibility to generate and measure non-ideal droplets over the 110-micron barrier.

An atomizer needed to be chosen that can create the droplet sizes the team is interested in. Pressure swirl and nebulizers are the focal point. Pressure swirl atomizers and nozzles were typically less expensive as compared to chemistry grade nebulizers. Additionally, if a nebulizer or an air blast atomizer was to be used the additional flow of air out of the nozzle would have to be included. The nebulizer company assured the team that their nebulizers could reach the team's desired flow rates, discussed below, but the droplet sizes would be very small. With pressure fed atomizers, this isn't the case. A Delavan WDB industrial spray nozzle was initially selected due to the flow rate flexibility and the cost effectiveness. The WDB nozzle had a ¼ in thread and a stainless steel and brass option. Their spray angle could be chosen from 30, 45, 60, 70, and 80 degrees and the flow rates varied from 0.3 Gallons per Hour to around 1 GPH for the lowest flow rates. However, this nozzle, explained further at the end of section 3.1, was unavailable; the steps taken by the team are additionally shown at the end of section 3.1. The atomizer chosen needs to meet and vary the volumetric flow rate of fuel to achieve the correct stoichiometric ratio of fuel to oxidizer. The estimated flow rates of fuel ranged from .05 to .5 gallons per hour, depending on the chosen fuel, calculations and fuel specific rates can additionally be seen in section 3.1. The team additionally discussed scaling up the air and fuel rates to match available atomizer fuel rates

for further experimentation, since even the top choice nozzle had a minimum flow rate double the team's desired minimum.

2.6 Burner Dimensions

Many possible designs were considered for the burner. Figure 12 depicts one such initial configuration where the atomizer is within the burner, and a N_2 coflow surrounds the exiting flow to reduce the impact of momentum dissipation. This was the team's initial theoretical design, and which was subsequently greatly modified.

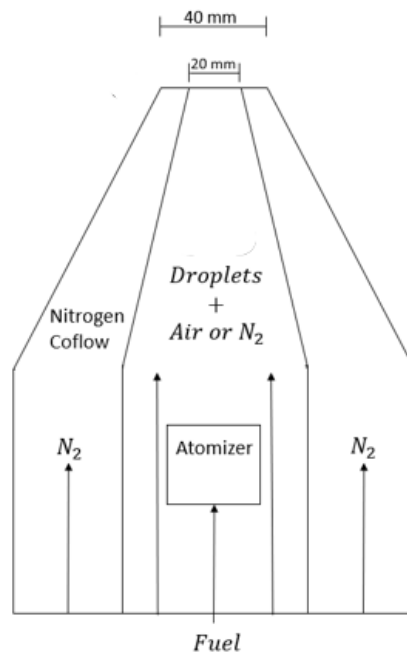


Figure 12: Burner Preliminary Design

Two different burners were then designed to have an initial diameter that narrows to an outlet diameter of 20 mm and 40 mm. The profile of the converging section of the nozzle needs to be optimized to limit boundary layer formation so a uniform, or top-hat profile, exits the burner. Several possible converging profiles were investigated and considered. The Rouse profile, as mentioned in Section 1.1.9, has been used for this purpose by other researchers. This was first

employed due to the simplicity of its calculation. Figure 13 shows the nozzle profile utilizing the Rouse profile for an inlet diameter of 63 mm, an outlet diameter of 20 mm, and a contraction length of 80 mm. The area contraction ratio, the ratio of the area of the outlet and the inlet, is set to 10.

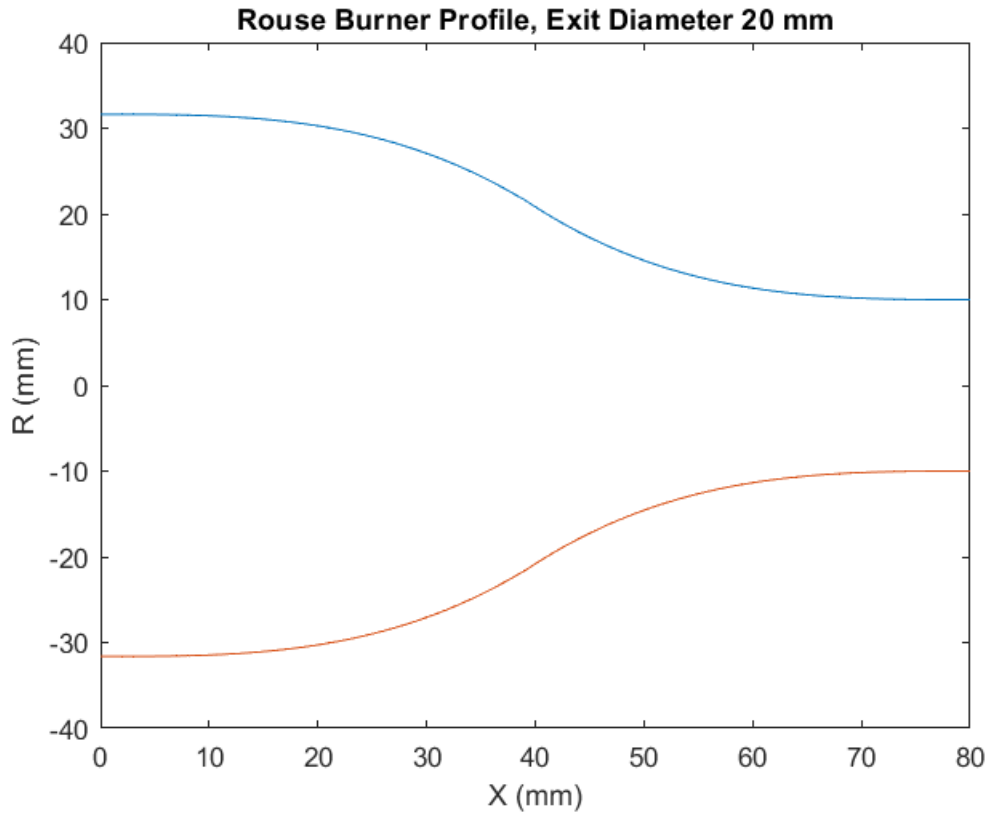


Figure 13: Rouse Burner Profile Along Length of Burner, Exit Diameter of 20 mm

It is also important to consider the minimization of the vortices at the concave section of the contraction. For that purpose, the methodology developed by Bergthorson (2005) was employed. The boundary conditions and parameters used to find this profile can be seen in Table 3. Figure 14 shows one such burner profile developed by utilizing this approach. The inlet radius is 25 mm, the outlet radius 10 mm, and the total length of the burner is 50 mm.

Table 3: Boundary Conditions and Parameters for Bergthorson Burner Profile

$r(0) = 25mm$	$r(x = 50mm) = 10mm$
$r'(0) = 0$	$r'(x = 50mm) = 0$
$r''(0) = 0$	$r''(x = 50mm) = 0$
$r(x = 10mm) = 25mm$	$r(x = 20mm) = 23mm$

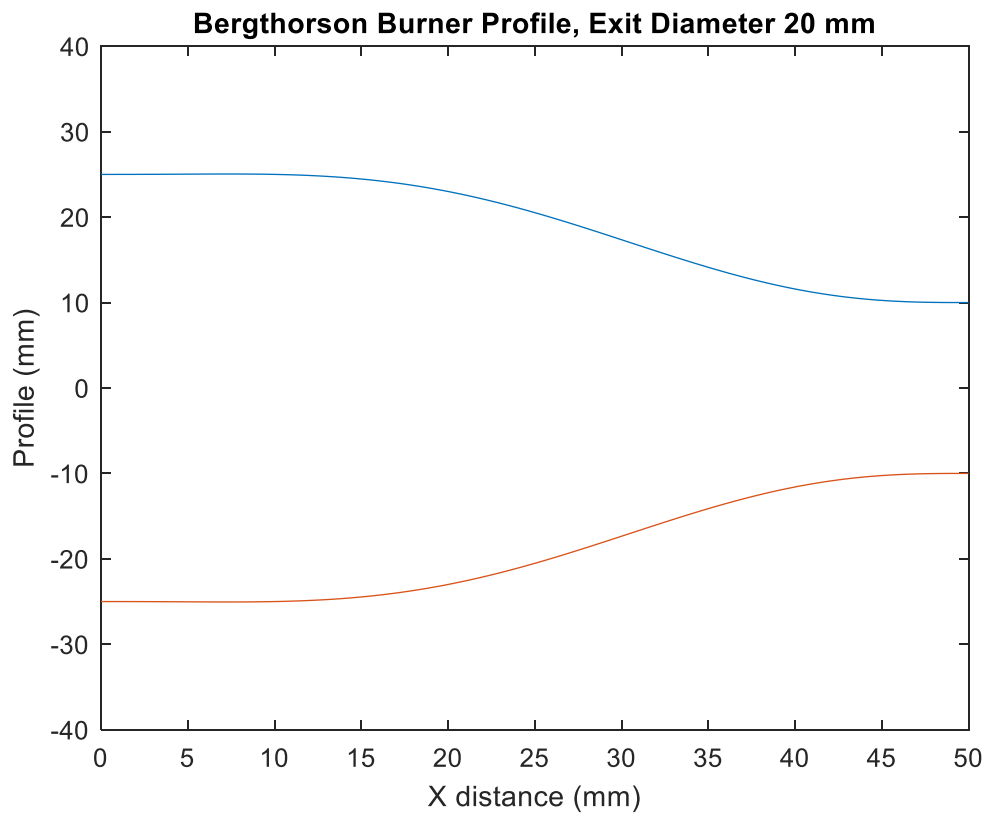


Figure 14: Bergthorson Burner Profile Along Length of Burner, Exit Diameter of 20 mm

For this profile, the Gortler parameter is kept below 50 for the entire length of the burner.

Figure 15 shows the values of this parameter along the burner.

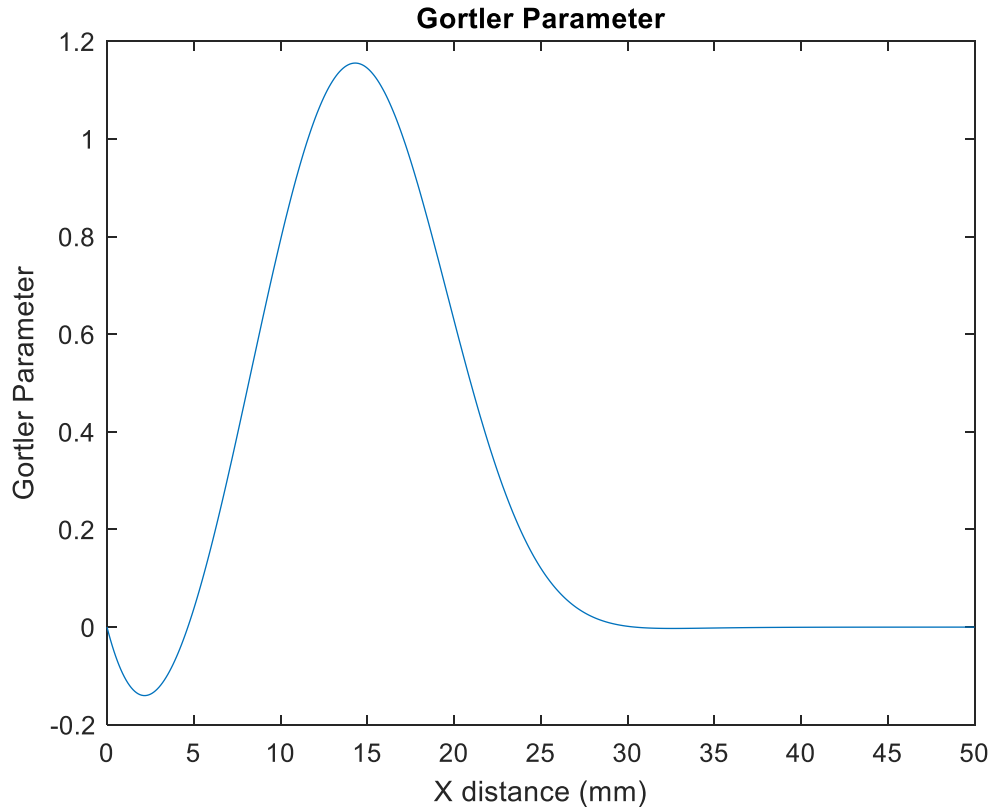


Figure 15: Gortler Parameter Along Length of Burner, Bergthorson Profile

Modeling of the flow will be conducted on the optimized Bergthorson profile, in FLUENT, to understand the exact nature of the exit velocity, see Section 3.2.

Along with ensuring that the flow will be close to uniform at the exit, the burner must be designed to allow for proper mixing between the fuel and the carrier gas, whether that is nitrogen for non-premixed or air for premixed. An initial configuration can be seen in Figure 16. The central inlet is for fuel, while the two other inlets are for the carrier gas. The issue that may arise with this configuration is the lack of mixing between fuel spray droplets and the gas: the small gas inlets do not allow the carrier gas to properly encase and mix with the fuel.

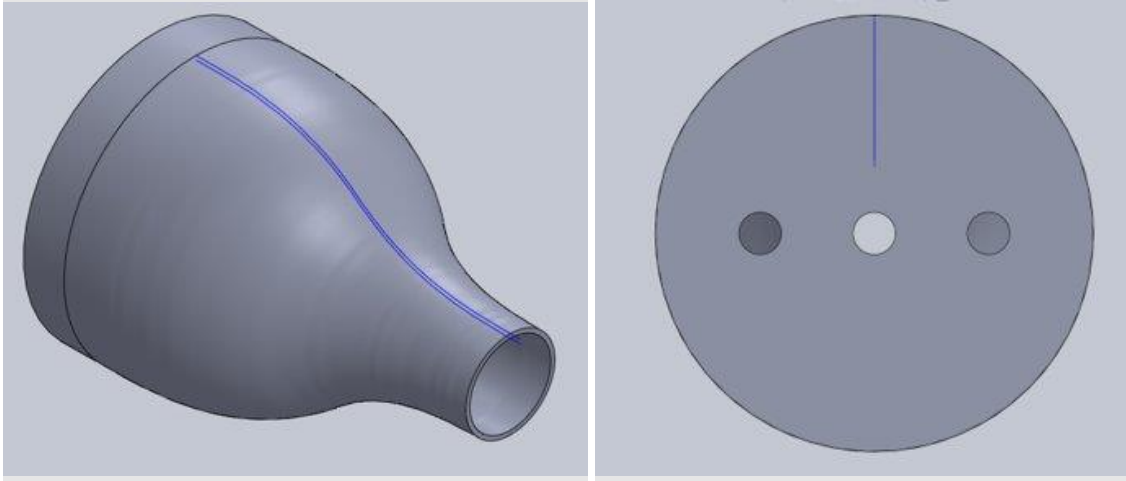


Figure 16: Initial Burner Configuration

The second iteration of the burner design can be seen in Figure 17. A detailed 2D CAD drawing can be found in Appendix C. Two carrier gas inlets are on the side of the burner. The fuel spray enters through an inner tube. After traveling a short distance, the gas flow is disturbed with the use of a mesh layer. Passing through the mesh, the gas is free to mix with the fuel spray before entering the converging portion of the nozzle and exiting the burner. The exact length of the burner is dependent on the residence and vaporization times of the fuel spray droplets and the atomizer spray angle, this is further discussed in section 3.1. The team's first choice of atomizer had a spray angle option of 30 or 45 degrees but due to challenges in obtaining one, the team utilized other options.

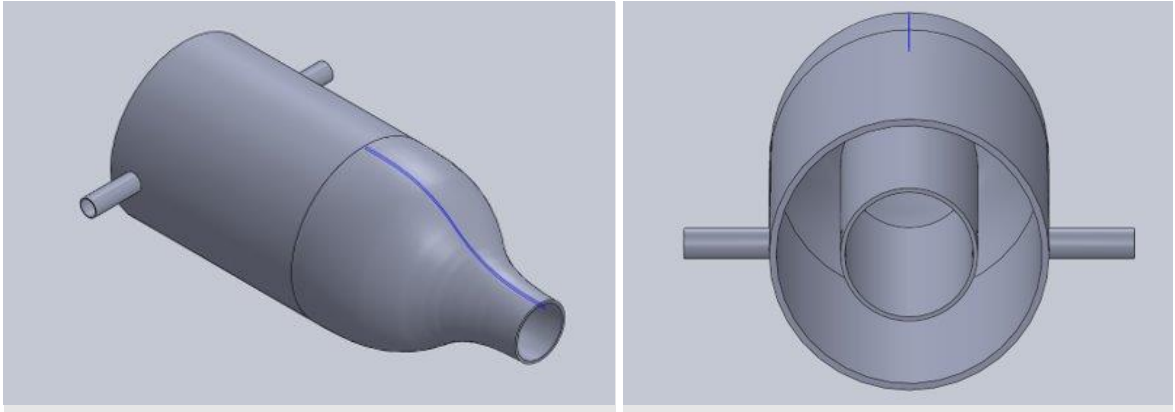


Figure 17: Second Iteration of Burner Configuration

The burner separation will be made adjustable to account for different fuels and jet velocities utilized. To ensure stability, this separation is kept between $0.5 < L/d < 2$ where L is the separation and d is the burner diameter (Figura & Gomez 2012).

2.7 Pressure Vessel

The pressure vessel outlined in this report is has not been constructed and thus has not been experimentally tested. Initial testing of the experimental apparatus was conducted without the use of a pressure vessel. As such, the first round of tests is expected to be under ambient conditions: 293 K and 101.325 kPa. Once the pressure vessel is installed, a range of high-altitude combustor conditions can be tested. With an average temperature of 265 K at 30,000 ft, a range of 250 K to 280 K will be considered. Similarly, with an average pressure of 40 kPa, a possible range of 30 kPa and 50 kPa was considered in the design of the pressure vessel. For future work, the apparatus should also be able to handle any temperatures and pressures between ambient and high-altitude combustor conditions.

The design requirements of the pressure vessel are quite complex and have been updated and changed as the experiment has updated. The vessel needs to be able to contain the burner, provide optical access through two windows, control inflow and outflow of gases to maintain

pressure, and relieve pressure to prevent accidents in the event of an uncontrolled pressure increase. The vessel needs to be able to hold the burners in place while in use. Refer to Figure 17 for the burner schematic with the inlet diameter of the burner as 10 cm, the outlet diameter as 2 cm, the total length as 50 cm, and the converging section of the burner as 5 cm. Figure 17 is the configuration, the dimensions are taken from the 3D printed model tested for uniform flow in Chapter 4. The maximum space between the burners is 5 cm. Considering the 50 cm burner length and the 5 cm space between the total space taken up by the burners is 110 cm. A minimum of 1 in (2.54 cm) will need to stick out of the flange to allow the air flow to enter the system. It also needs to be large enough to not interfere with the flow from the burners. The two windows need to be large enough for the experiment to be viewed. However, the larger the windows the lower the maximum pressure is so a balance must be maintained. The windows are the weak point of a pressure vessel because they are made of weaker materials than the vessel itself. The tensile strength of glass is much lower than steel. A constant inflow and outflow of gases in the vessel need to occur to maintain the desired pressure of the experiment. Safety must also be considered to stop accidents from occurring that could cause damage during use.

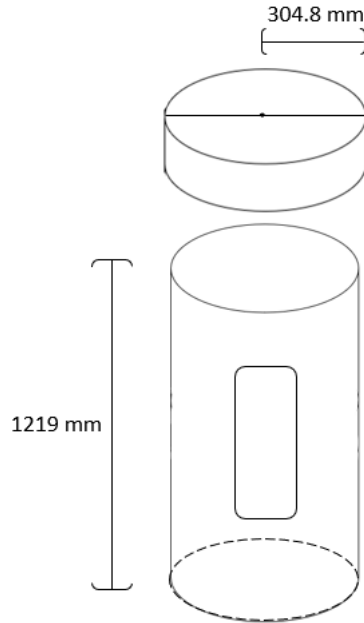


Figure 18: Pressure Vessel Preliminary Diagram

The initial pressure vessel dimensions are shown in the pressure vessel preliminary design figure. These dimensions considered the original design of the experiment. The burners would be inserted at the top and bottom of the vessel and could be adjusted to fit the distance between them at a maximum of 5 cm. Initially, this design was supposed to stop the vessel from interfering with the space in between the burners. However, modifications were made further on in the design process that drastically changed the vessel. When deciding on a material the most important factors are the cost, corrosion, ability to handle forces, and the tensile strength of the material. Most pressure vessels are created out of aluminum, carbon steel, or stainless steel. The cost of aluminum is lower than both carbon steel and stainless steel. However, the actual welding of the pressure vessel requires special techniques for aluminum which cost much more money than the welding of carbon steel or stainless steel. 6061-T6 aluminum is a common pressure vessel material. It does have a lower tensile strength than A537 carbon steel and T-316 stainless steel. Both carbon steel and stainless steel have high tensile strength. Due to steel's high tensile strength the maximum

allowable stress on a vessel made of steel is much higher than that of other materials. Both stainless steel and carbon steel are chemically resistant and are used in industry to hold several different corrosive materials. The corrosive materials in this experiment such as heptane, kerosene, and ethanol are resisted by both stainless steel and carbon steel quite well. The three materials found based on the factors listed and several industry pressure vessel creators were A537 and A516 carbon steel and T-316 stainless steel. The following table shows the mechanical properties of the three materials.

Table 4: Mechanical Properties of Possible Pressure Vessel Materials

Material	Tensile Strength (Mpa)	Density (g/cm ³)	Modulus of Elasticity (Gpa)	Bulk Modulus (Gpa)	Poissons Ratio	Shear Modulus (Gpa)	Cost \$/kg
T-316 stainless steel	500	8	193	152	0.265	82	2.36
A537 Carbon Steel	315	7.8	200	60	0.29	80	0.64
A516 Carbon Steel	260	7.8	200	60	0.29	80	0.65
6061-T6	276	2.7	68.9	68	0.33	26 (.25" thick 12"x12")	50.91

Based on the cost and accessibility A537 carbon steel was chosen as the material. The tensile strength, 315 Mpa, was high enough for the use of the vessel in the experiment while also having also having a similar density and modulus of elasticity to its stainless-steel counterpart and having equal properties to A516 carbon steel without having the lower tensile strength.

Using Equation 28, also written below, the hoop stress exerted on the vessel using the dimensions found in Figure 18, a wall thickness of 0.5 in, and a pressure of 50 kPa was 254.85 psi.

$$\sigma_{\theta} = \frac{p(r + 0.6t)}{tE}$$

Equations 28 and 29 outline the calculation of hoop stress, σ_{θ} , in a cylindrical vessel. Hoop stress varies with pressure (p), inner radius (r), and thickness (t). Furthermore, calculations were also done from 1 atm to 10 atm. This was done to see how much the hoop stress would increase at higher pressures. Initially this testing was done with a 12 in radius as shown in Figure 18. However, the radius has been adjusted to the 17 in radius which is explained later in this section. Figure 19 shows the hoop stress for each of the pressures tested.

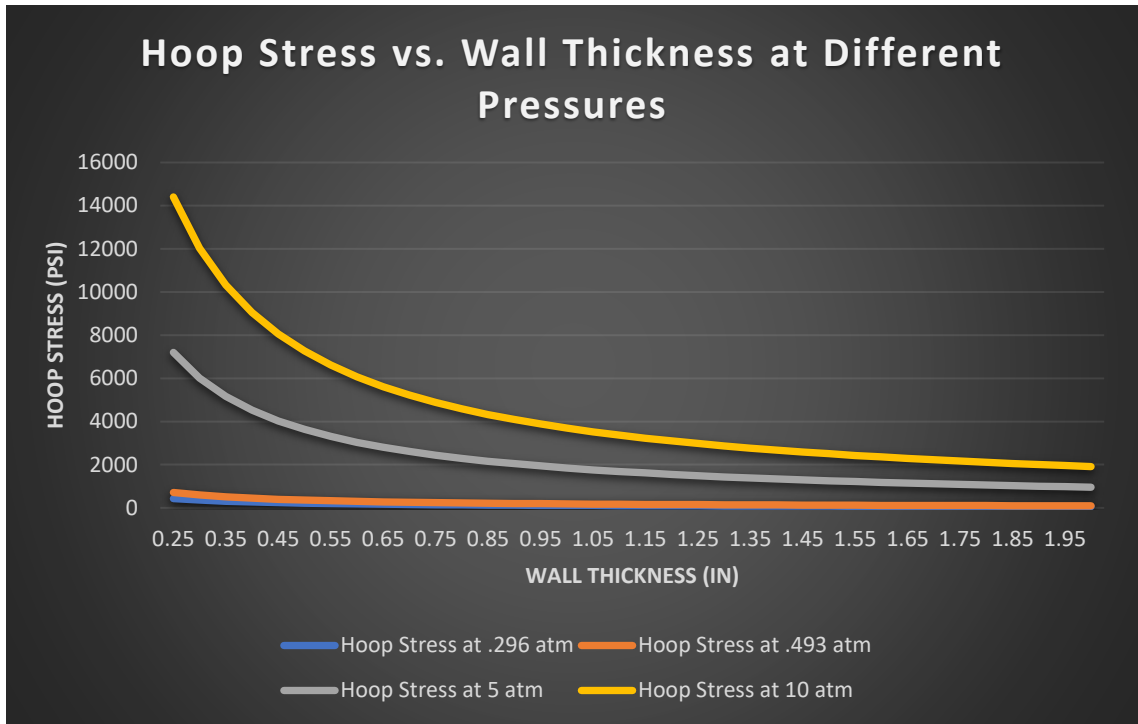


Figure 19: Hoop Stress at Tested Pressures

While the experiment will be done between 30 and 50 kpa, the vessel is designed with 10 atm pressures in mind. This was done to allow the vessel to be used in other experiments. Because the tensile strength of A537 carbon steel is so high, attaining a pressure of 10 atm was not difficult. Figure 20 shows the maximum working pressure vs. wall thickness of the vessel with an inner radius of 17 in.

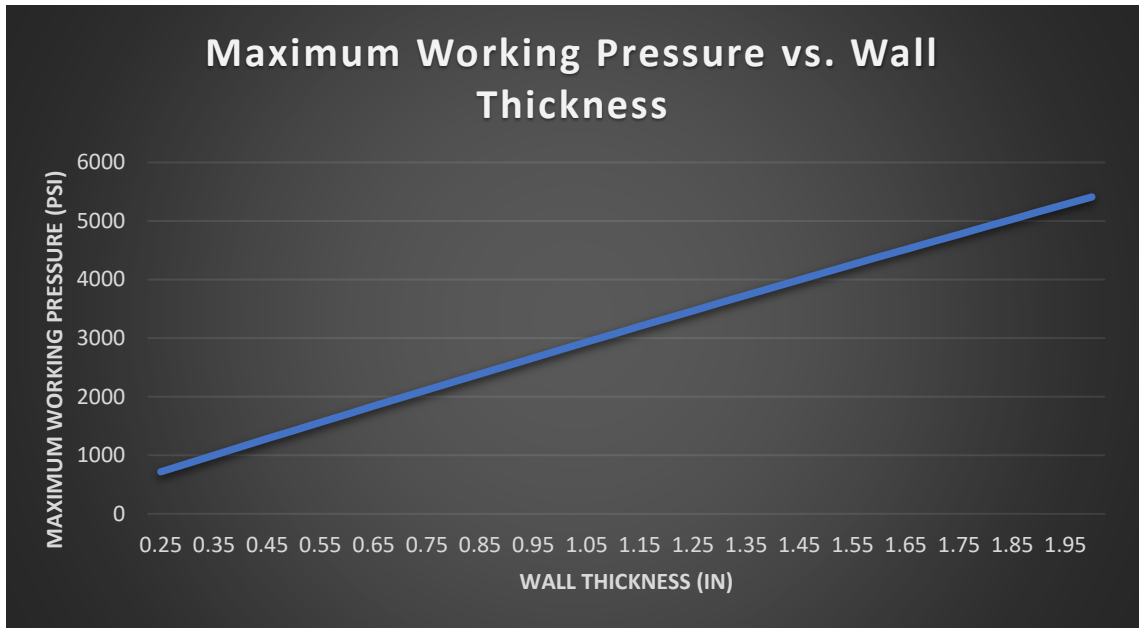


Figure 20: Maximum Working Pressure of A537 and A516 Carbon Steel with an Inner Radius of 17 in

The initial design laid out in Figure 18 has been changed dramatically and the changes are outlined below. Firstly, the pressure vessel was initially vertical to allow for ample space for the burners to fit inside. The problem is how the burners would be integrated into the pressure vessel design. Figure 17 shows the burner configuration. This burner configuration is important in the design of the pressure vessel because of the length of the burner, 50 cm, and the outlet diameter, 2 cm. The length of the burner can be resized and will not affect the flow if the converging section is kept to 5 cm. The burners would be at most 5 cm apart from each other to allow space for the reaction. If the pressure vessel is vertical with a radius of 12 in and an aspect ratio (L/D) of 2 (length=48 in) as shown in Figure 18, the burners would have to be held in place deep in the pressure vessel or have a long tube connecting them to the vessel. However, if the pressure vessel is flipped to be horizontal this would allow the burners to be much closer together and be much easier to integrate into the pressure vessel.

The next design choice changed was the inner radius of the pressure vessel. Since the pressure vessel was flipped horizontally the need for a larger inner radius is more important. The inner radius was decided from the burner length and the burner exit diameter. The burner exit diameter is 2 cm. The outlet of the burners could collide with the vessel's walls if the vessel's inner radius is too small. Furthermore, the total length of the burners and the space in between the burners is 110 cm. Based on these two an inner radius of 17 in (43.18 cm) was chosen. The end of the burners will be mounted at the entrance of the flange of the vessel allowing for the space to be adjusted by remounting the burners. 17 in allows for the burner to be held within that 5 cm range and will stop the vessel walls from interfering with the burner outlet flow since the inner radius is 21 times larger than the diameter of the burner outlet. The length of the cylinder is also important regarding the burner's outlets. The release valves and flows entering and exiting the vessel will also need to be distributed down the cylinder. To leave ample space for all the equipment, a length of 34 in was decided for the vessel.

Initially wall thickness was considered a very difficult design parameter. This was determined based on the massive effect wall thickness has on the maximum pressure of the vessel as shown in Figure 20. However, when the max pressure of 10 atm was determined the wall thickness became a minor point. Having a high wall thickness is ideal for high pressures as the max wall thickness, 2 in, shown in Figure 20, 5411 psi (368 atm). 2 in is too high for this experimental setup. The wall thickness test was decreased to 0.25 in to see what the max theoretical pressure would be for the vessel. The max pressure at 0.25 in is 717 psi (49 atm). The vessel is still almost 5 times higher than the desired max pressure. However, going any thinner with the wall thickness could prove problematic to the during testing as making the wall too thin could

cause problems such as denting if any accidents were to occur. Therefore, the wall thickness chosen for the vessel is 0.25 in.

During the design of the pressure vessel safety was a major factor. If an accident occurs and the pressure vessel needed to be vented or depressurized for any reason a safety release valve would be required. A spring released safety valve would allow for automatic release if the pressure inside the vessel got too high. A safety release valve works by setting the spring force inside the valve to a specific pressure so when the pressure at the end of the valve connected to the vessel is higher than the spring force the valve will activate relieving the pressure in the vessel. However, the safety release valves spring force should not be at the maximum pressure of the vessel. The ASME standards recommend a safety factor of 4 for any bolted pressure vessel. The spring force of the safety release valve should be set to 9.75 atm which is $\frac{1}{4}$ of the max working pressure of the vessel. The safety factor is important in preventing accidents and allowing safe use of the vessel during experimentation. The experiment will be operating at a maximum of .493 atm so the safety release valve should not interfere with the experiment. The safety release valve chosen is the pressure relief valve SV805 from Witt Gas. The valve is a spring-loaded valve which can be set to the specific pressure (Witt Gas, 2022). The valve is rated up to 44.36 atm. Figure 21 shows the release valve.



Pressure relief valve SV805

Figure 21: Pressure Relief Valve SV805

Windows needed to be designed for the pressure vessel to allow optical access. The main problem with windows is that they significantly bring down the maximum pressure of the vessel because the material for a window has a much lower tensile strength than A537 carbon steel. The main problem is that most pressure vessels are only capable of a very small window based on how they are implemented. Typically, windows sized at 0.5 in are used in pressure vessels. However, the experiment would be impossible to view or get any data from with a window that small. The space between the burner outlets is 5 cm (1.965 in) max. Having a window this size may cause problems when trying to view the entirety of the experiment as parts of it may get cut off. A radius of 2.5 in will allow for extra space when viewing the experiment. A wall thickness of 0.5 in should suffice for the window as well. This was decided not from stress calculation but from the external holder of the window being 1 in. Therefore, the window needed to be held in the holder and was chosen to have a thickness half the size of the holder. The problem of how the window would be attached to the vessel then appeared. However, based on industry standards of companies such as

Parr Industries a solution was found. The window will be externally mounted with a flange being added to the top and bottom of the pressure vessel as shown in Figure 23. The window would then be bolted into the flange setting it in place. This extension does lower the maximum pressure of the pressure vessel to about 40.83 atm (Parr Industries Company, 2022). The decrease in pressure occurs because of the joints connecting the flange to the main vessel and the tensile strength of the window being much lower than the vessel. A safety factor of 4 should be accounted for when designing the window. When designing the vessel Pyrex was considered for the window material. The material is clear and will be ideal for inspecting the experiment going on inside. The material is incredibly cheap, costing about \$12.91 for a 5 in x 5 in x 1/8 in sheet. However, the tensile strength of Pyrex is only 1000 psi. Polycarbonate was also inspected as window material. Polycarbonate is cheaper costing \$5.52 for a 6 in x 6 in x 1/4 in sheet. Furthermore, the tensile strength is 9500 psi which is significantly higher than Pyrex. Polycarbonate is clear and would work well for inspecting the experiment. Based on the criteria outlined above polycarbonate is the better choice for the window materials. The window will be mounted to an external holder with 12 bolts as shown in Figure 25. The holder will then be bolted to the flange with 8 bolts with a gasket in between the flange and the holder to stop any leaks.

The inflow and outflow of the vessel will be controlled by pressure regulators set to specific pressures and will be attached to the vessel. They will be adjusted to the value required for the experiment. The pressure trying to be maintained for the experiment will be set up between 30 and 50 kpa. In the case of ignition experiments, using an inert gas like nitrogen as the coflow through the inlet can help dilute the reactants and prevent the buildup of a combustible mixture throughout the chamber. The inlets will be at either side of the top burner flange to help sustain the stagnation plane of the experiment. The outlet valves will be further out on the vessel equidistant to the burner

flange so as not to interfere with the inlets but will also be entering from the top of the vessel. Having the outlets further out will allow for no interference with the experiment by not exhausting any of the materials entering the vessels through the burners. Figure 22 shows a diagram of the setup of inlet and outlet of the flow.

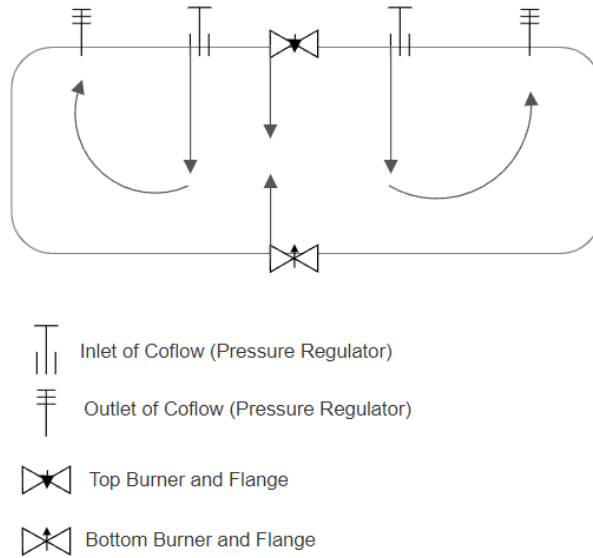


Figure 22: Inflow and Outflow of the Vessel

2.7.1 Pressure Vessel CAD Design

This section displays the SolidWorks modeling of the pressure vessel. The individual parts are shown and may be updated based on further research. Appendix C has drawings of the parts. Figure 23 shows the pressure vessel designed for the experiment. The dimensions of the vessel are shown in Table 3.

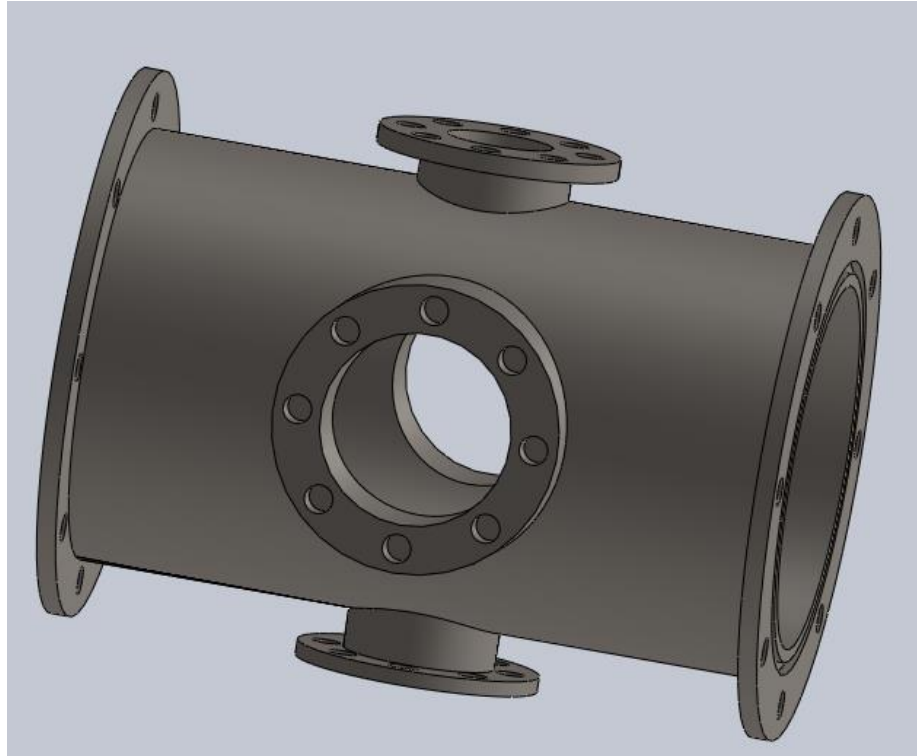


Figure 23: Pressure Vessel Design

Table 5: Pressure Vessel Dimensions

Pressure Vessel Parts	Dimensions (in)
Inner Radius of Vessel	17
Length of Pressure Vessel	34
Wall Thickness of Vessel	0.25
Burner Insert Flange	0.787
Burner Flange Top	0.5
Burner Flange Diameter	6.3
Burner Insert Diameter	2.755
Window Flange Diameter	7.5
Window Insert Diameter	5
Endcap Flange Top	0.5
Endcap Flange Radius	14.7

The endcap flanges attached to each end of the pressure vessel are shown below in Figure 24. The endcap has a diameter of 36 in and a thickness of .25 in.

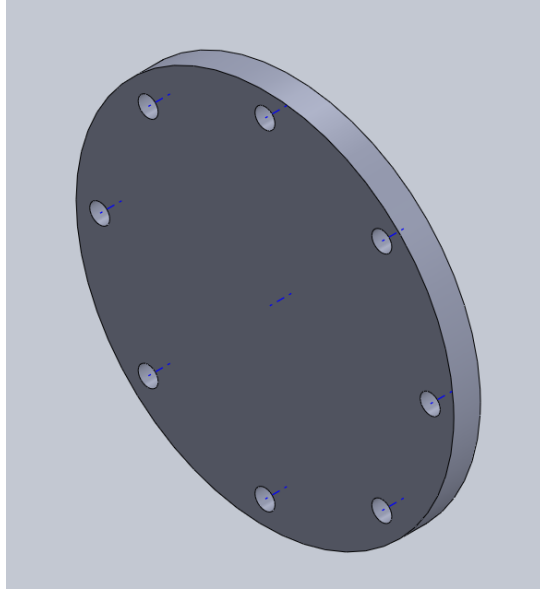


Figure 24: Pressure Vessel Endcap

The window and window holder designed for the vessel are shown below in Figure 25.

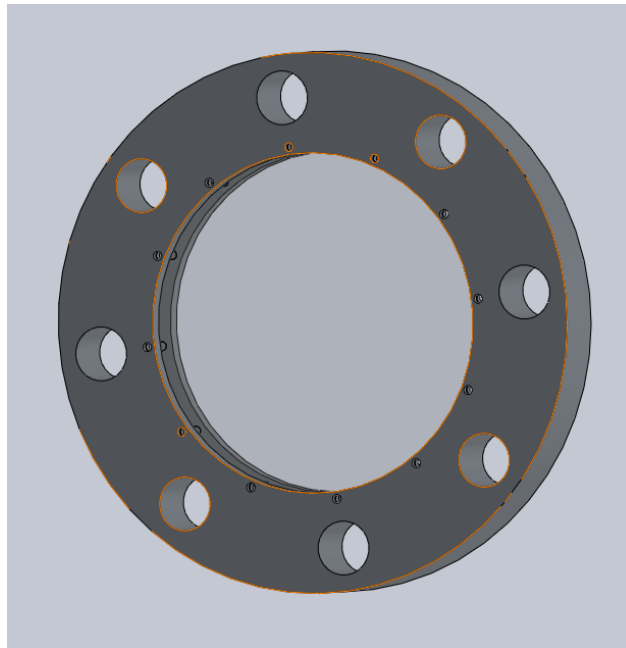


Figure 25: Pressure Vessel Window and Holder

The full assembly is shown in Figure 26.

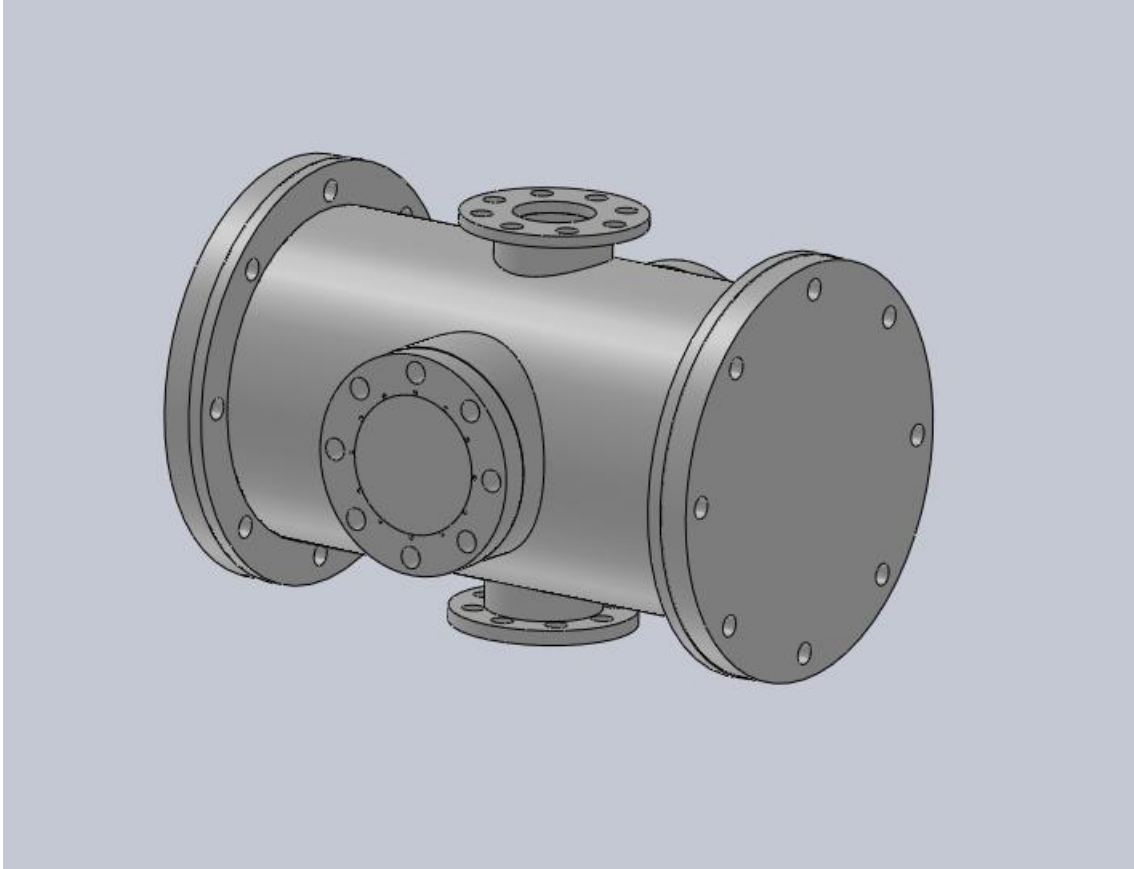


Figure 26: Full Assembly of Pressure Vessel

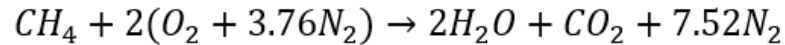
3 Modeling

This section details the modeling used to design and improve each component of the experimental apparatus. The layout is broken down into four main categories: Atomizer, Burner, Flow System, and Pressure Vessel.

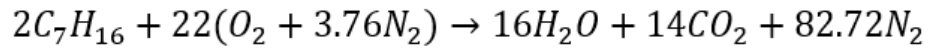
3.1 Air to Fuel Ratio and Droplet Vaporization Times

Stoichiometric air to fuel ratios were calculated to estimate fuel injection rates, to decide on atomizer possibilities, and predict some aspects of combustion. Both molar and mass AFRs are shown below. Various chemical combustion reactions are shown below. Not all fuels are to be tested but analysis was done to compare options.

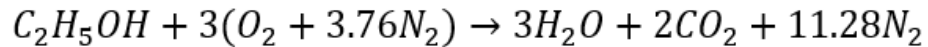
3.1.1 Methane AFRs - 9.52 molar; 17.16 mass



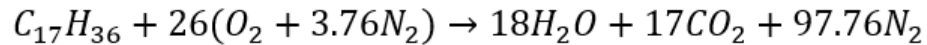
3.1.2 Heptane AFRs – 52.36 molar; 30.20 mass



3.1.3 Ethanol AFRs – 14.28 molar; 8.95 mass



3.1.4 Heptadecane AFRs – 123.76 molar; 14.84 mass



Once the stoichiometry was completed the AFR was used to solve the desired fuel injection rates, which are shown in the tables below for maximum and minimum air inlet flow rates. These mass flow rates were 0.00038 kg/s and 0.000038 kg/s. The equations for calculating mass flow rates additionally follow-on Figure 27. The values on this figures line are multiplied and the bottom values are divided. Following these calculations, ‘x’ amount of mass flow rate of air is divided by the molar mass of air, then divided by the molar AFR ratio, and finally multiplied by the molar mass of the specific fuel. Additionally, as described in the calculations of the mass flow rate, the molar fuel flow rate is the value prior to multiplying by the fuels molar mass. The volumetric flow rate is found with a simplistic dimensional analysis – converting units and utilizing density of the specific fuel. The densities the team used are shown in Section 2.4. Both Table 6 and 7 display the mass flow rate, molar flow rate, air to fuel ratios, and volumetric flow rates of 4 fuels that could be used for testing. Table 6 shows the values that correlate with the team’s theoretical minimum

flow rate and Table 7 shows the values that correlate with the theoretical maximum air flow through the designed nozzle. The method and source of these minimum and maximum values can be found in section 2.3 with the sonic nozzle flow calculations. All fuels are liquids besides gaseous methane and densities and conditions can also be found in section 2.4

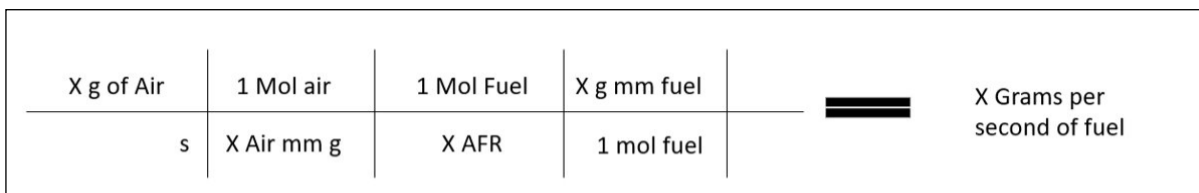


Figure 27: Stoichiometric Fuel Calculations Utilizing the Commonly used Domino Method

Table 6: Fuel Flow Rates for the Minimum Air Mass Flow Rate 0.000038 kg/s

Fuel Flow Rates		g/s	moles/s	AFR - molar	mL/min
	△ methane	2.20E-03	1.38E-04	9.52	1.99E+02
	△ ethanol	4.23E-03	9.19E-05	14.28	3.21E-01
	△ N-heptane	2.51E-03	2.51E-05	52.36	2.20E-01
	△ heptadecane	2.55E-03	1.06E-05	123.76	1.97E-01

Table 7: Fuel Flow Rates for the Maximum Air Mass Flow Rate 0.00038 kg/s

Fuel Flow Rates		g/s	moles/s	AFR - molar	mL/min
	△ methane	2.20E-02	1.38E-03	9.52	1.99E+03
	△ ethanol	4.23E-02	9.19E-04	14.28	3.21E+00
	△ N-heptane	2.51E-02	2.51E-04	52.36	2.20E+00
	△ heptadecane	2.55E-02	1.06E-04	123.76	1.97E+00

After computing the theoretical fuel rates, it was time to solidify atomizer choices and compare further compare available atomizers. Choosing an atomizer that can handle these flow rates is apparent, but the challenges revolve around understanding droplet physics and placement of the atomizer. Since the team is trying to model relight, larger non-vaporized droplets are desired.

D^2 law, described in the introduction, was the basis for understanding droplet residence time and vaporization rates. It is important to keep the well-defined boundary at the exit of the burner to compare the team's experiments and models. The figure below depicts droplet size versus time with respect to different temperature differentials between the surrounding gas and the surface of the droplet. The team calculated the values at standard sea level temperature and pressure. Challenges pertaining to these calculations revolved around choosing which T_1 to use, T_1 being the surface temperature of the liquid. If the temperature of the atmosphere is above the boiling point of the liquid the boiling point temperature should be used. Furthermore, if the temperature of the atmosphere/far field is less than the boiling point of the liquid, only the temperature differential should be considered in the calculation of characteristic heat transfer number. T_1 is then just the temperature of the liquid droplets.

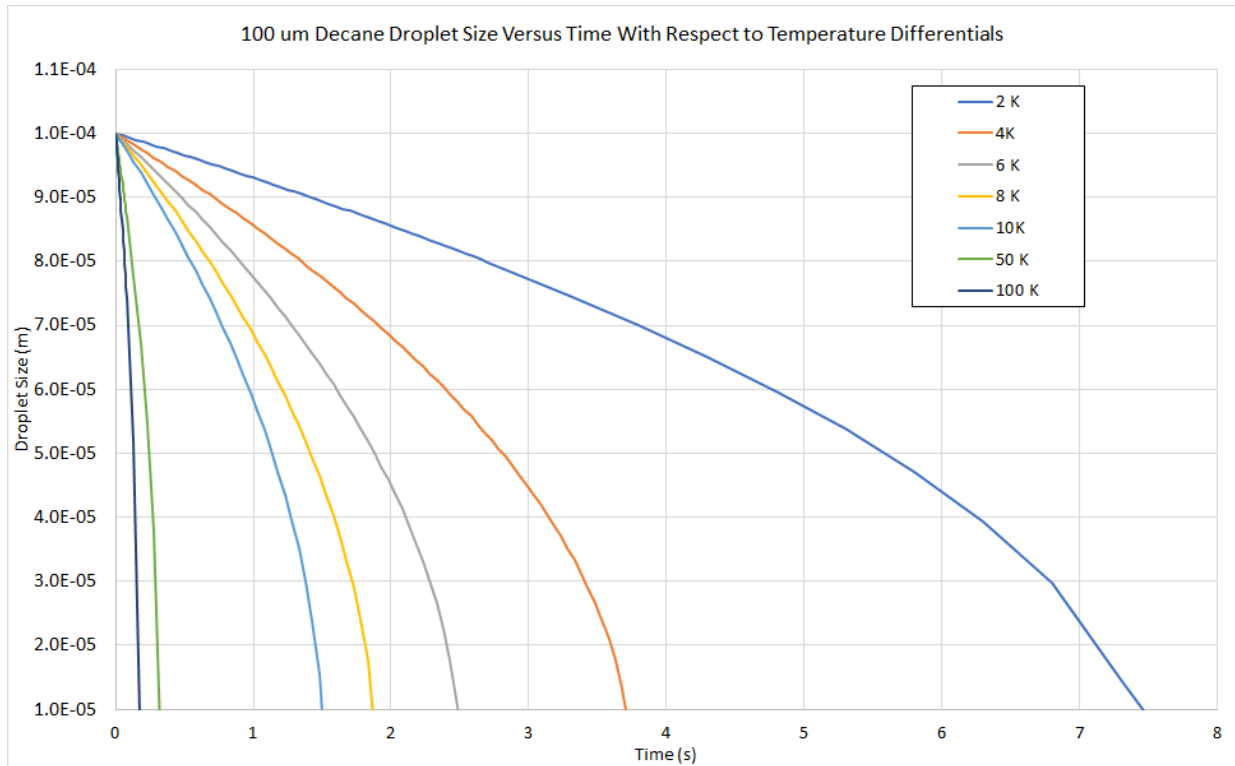


Figure 28: 100-micron Decane Droplet Size versus Time with Respect to Temperature Differentials Between the Fluid and the Flow

As depicted above in Figure 28, the higher the temperature differential the faster the droplets vaporize, creating premixed-type condition. For engines it is beneficial to have fuel vaporize quickly, but to model relight it poses a challenge. To best model relight the team would have to keep the temperatures precise with respect to one another and understand that the colder the system is the longer the droplets will last. This last assumption cannot be seen as easily with this graph but can be understood through the mass transfer number formulation of the D^2 law, specifically the vapor-liquid equilibrium. Since temperature affects the density, thermal conductivity, and the specific heats of the liquid fuels slightly therefore increasing the vaporization times. When more kinetic energy in the molecular kinetic systems, the molecules experience changes to their properties stated above, resulting in “stabler” droplets at lower temperatures. Additionally, the lower the temperature, the lower the mole fraction of vapor at the vapor/liquid interface.

Once the team got a solid understanding of D^2 law they proceeded to compare fuels and their respective residence and vaporization times at similar conditions – specifically temperature differentials. Ethanol, heptane, decane, and heptadecane were the fuels of interest. The time it takes to evaporate 10 percent of the droplets' total size – starting at 100 microns wide – is displayed below in Tables 8a-b. Figure 29 shows a comparison between the fuels of interest and their times to evaporate. As evident from the table the longer chain organics evaporate slower but still do not provide the optimal amount of time for droplets to enter the team's burner without large amounts of vapor. The desire is to vaporize the fuels as minimally as possible to recreate high-altitude relight and its larger, colder droplets.

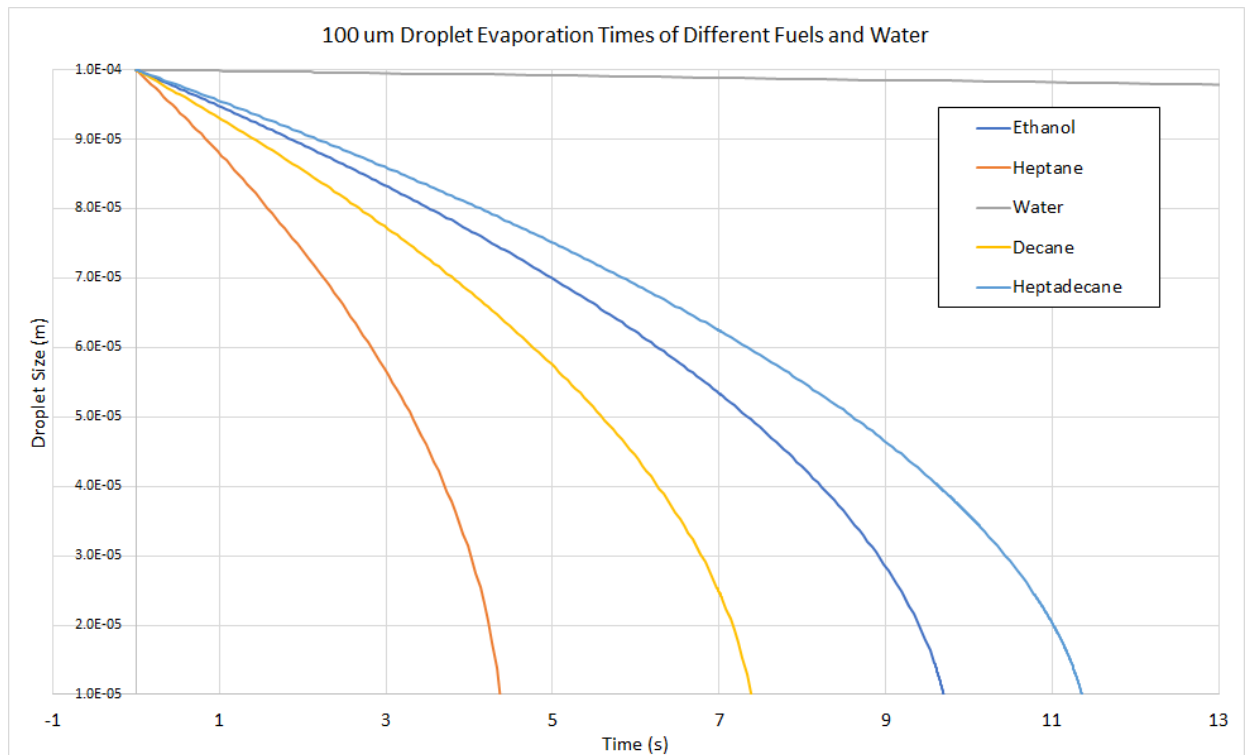


Figure 29: 100 um Droplet Evaporation Times of Different Fuels and Water

Table 8a: Time to Reach 10% Loss of Diameter Due to Vaporization of 100 um Droplets

(Various Fuels)

Time to Reach 10 % Loss of Diameter Due to Vaporization of 100 um Droplets	
Water	58.167 sec
Heptadecane	2.180 sec
Ethanol	1.861 sec
Decane	1.417 sec
Heptane	0.839 sec

Table 8b: Time to Reach 10% Loss of Mass Due to Vaporization of 100 um Droplets (Various Fuels)

Time to Reach 10 % Loss of Mass Due to Vaporization of 100 um Droplets	
Water	24.002 sec
Heptadecane	0.899 sec
Ethanol	0.768 sec
Decane	0.585 sec
Heptane	0.346 sec

Ethanol-water solutions became of interest when the team brainstormed methods of expanding droplet lifetimes. Even though ethanol has a relatively low vaporization time – as seen on the above table – it can be made into a solution with water to extend its vaporization time. This is since water has the slowest evaporation rate when compared to the fuels in question. In Figure 30 below the results of a parametric study detailing the effects of different ethanol-water solutions is displayed. The higher the water concentration the longer the droplet lifetime. Even with just 20 percent water the droplet would last 300 percent longer by total size. Within 14 seconds the 100-um ethanol-water droplet would only lose 10% of its mass and be able to travel 630 cm, since it is traveling at or near the expected flame speed range of 45-60 cm/s, which is now plenty of distance. The mass and diameter reductions can be seen on Tables 9a-b. The only issue that arises from using a water-based mixture is ignition consistency and flame stability. Further tests could be run in a Bunsen burner type of experiment to test the ability of different concentrations to keep a sustained flame. Ethanol-water solutions could also be viewed as a way of mimicking the high-altitude reflight condition of water entering the combustion chamber. When conducting this parametric model of

ethanol-water solutions the team used a summation method for finding the solutional properties. The molar fraction of the pure and combine species properties were used. This simplification works well for density but is not as accurate an approximation for the other properties (McQuarrie et al. 2011). The properties calculated and the equations used can be seen on Table 11 and Figure 31 respectively. X_i is the mole fraction. Both n_i and n_{tot} are the number of moles but n with the subscript i is the species moles and the subscript tot refers to total moles of species present. P_i is the individual species property. P_{tot} is the total calculated property of the solution. Droplets could be tested in the same fashion as shown in section 4.2 to further quantify evaporation rates.

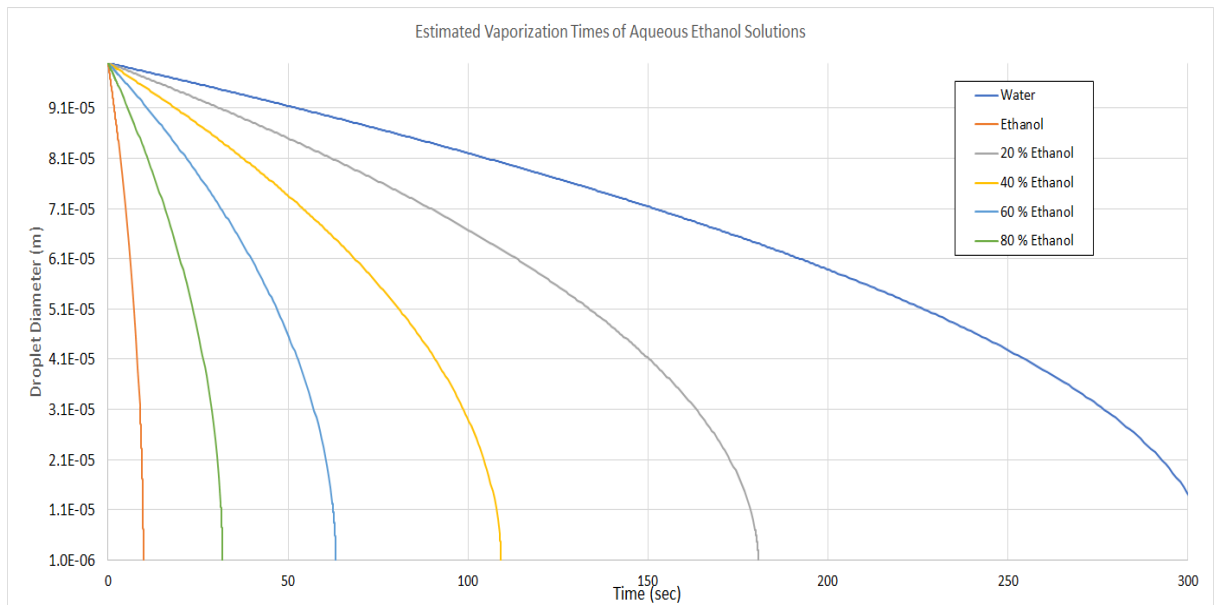


Figure 30: Parametric Study of Ethanol-Water Solution Estimated Vaporization Times

Table 9a: Time to Reach 10 % Reduction in Diameter of 100-micron droplets of Different Ethanol Concentrations

Time to Reach 10 % Reduction in Diameter of 100 um Droplets	
20	34.332 sec
40	20.747 sec
60	12.024 sec
80	6.038 sec
Pure Ethanol	1.860 sec
Pure Water	58.167 sec

Table 9b: Time to Reach 10 % Reduction in Diameter of 100-micron droplets of Different Ethanol Concentrations

Time to Reach 10 % Reduction in Mass of 100 um Droplets	
20	14.167 sec
40	8.561 sec
60	4.962 sec
80	2.491 sec
Pure Ethanol	0.768 sec
Pure Water	24.002 sec

Table 10: Total Vaporization Times of 100-micron droplets of Different Ethanol Concentrations

Ethanol %	Total Vaporization Time (Sec)
20	180.695
40	109.195
60	63.286
80	31.778
Pure Ethanol	9.792
Pure Water	306.143

Table 11: Properties Used for Ethanol-Water Solution Study

Ethanol Percent	Moles	Mole Fraction	Thermal Conductivity (W/mk)	Cp	Density (kg/m ³)	Heat of Vaporization (J/Kg)
20	343.043	0.072	0.029	3897.535	982.096	2154993.701
40	686.087	0.171	0.044	3755.909	961.496	2015384.985
60	1029.130	0.317	0.067	3547.371	931.163	1809816.684
80	1372.174	0.553	0.103	3209.833	882.067	1477085.889

$$P_{tot} = \sum X_i P_i$$

$$X_i = n_i / n_{tot}$$

Figure 31: Equations Used for Ethanol-Water Solution Study

(Terms defined earlier within this section)

Keeping the vaporization times and flow rates in mind, the team knew that it would have to be flexible in atomizer placement depending on the atomizer used and droplet sizes attainable at each corresponding flow rate. An atomizer placed too far might give too much time to vaporize.

The team created the idea of a modular atomizer assembly where the atomizer and fuel inlets would be in a cylindrical apparatus, with the same volume as the largest part of the converging nozzle. This is further illustrated in Figure 32. The atomizer could then be placed further upstream by adding additional cylinders that would lengthen the distance of the atomizer exit to the converging nozzle. Possible placements are shown on the figure as 1, 2, and 3. Each rectangular section in front of the numbered place chosen would allow more open space leading to the converging nozzle. Thus, allowing for more vaporization if necessary. The placement of the atomizer would not interact with the flow smoothing mesh placed in the burners air inlets since the atomizer – and therefore the droplets – are on the midline of the burner with walls protecting the air from the droplets until the converging segment is reached – see initial burner configuration in section 2.6.

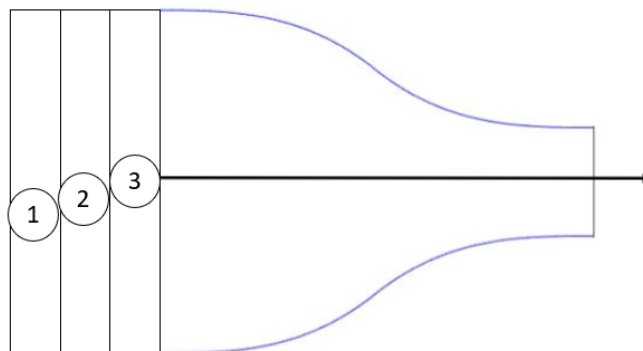


Figure 32: Placement of the Modular Atomizer Assembly within the Burner

After gaining a better understanding of our flow system capabilities it was recognized that larger droplets were going to be much harder to generate consistently at our low flow velocities. Originally the WBD Industrial Spray nozzle by Delavan was chosen for its flexibility but challenges arose in the contacting of Delavan. Delavan is a company based in the U.K but owned

by an American subsidiary. The team attempted to contact Delavan but could not reach them. After multiple attempts the team needed to pivot its decisions. A search for a similar Delavan nozzle sold locally occurred and led to the industrial supply company Grainger. However, after this lack of contact we decided to contact other atomizer manufacturers. This led back to Meinhard, a chemical nebulizer and glass blowing manufacturer. The team understood that Meinhard's products were typically used for gas chromatography and mass spectrometry, so the expected droplet sizes were to be much lower. This would lower our ability to fully model relight but if the small droplets were kept from evaporating, we could still study the impact of unevaporated fuel. Meinhard was very helpful and supportive in providing part selection and understanding of the specifications of their nebulizers. A lead scientist at Meinhard explained the challenges that we could expect, the droplets would be around 3 microns in diameter. The lowest the team wanted to go was around 15 microns since this already strains the vaporization amounts of the droplets and the freedom of atomizer placement. 15-micron droplets at 45 cm/s would only be able to travel a distance around 14 cm and would completely vaporize in 0.313 seconds if held at a temperature differential of 2 K. This residence time – time the droplets stay in the burner - and total vaporization time do not correlate well with the team's desired low vapor conditions. Meinhard's scientist explained that we could possibly get droplets surpassing 45 microns if we increased our fuel injection rate, but they had no exact data for this, just theoretical calculations. They graciously agreed to send us a couple of nebulizers to test if the conditions were appropriate for our experiment and we found that we could expect 15–25 micron wide droplets at our maximum stoichiometric fuel flow rates. These were expected to be used in our primary testing to see if they match our desired test conditions. Gravity fed fuel and pressurized air would flow into this nebulizer.

A few secondary plans were in the works in-case the Meinhard nebulizers are unusable. Grainger had some Delavan nozzles in stock, with fast response times, that appear to match similar conditions as the Delavan WDB nozzle we wanted first, as described in section 2.5. This new Delavan nozzle had a spray angle of 70 degrees and a max flow rate of .6 gallons per hour which is listed on Grainger. The teams flow rates of interest are .05 to .5 GPH, when converted from ml/min. The flow rate of this nozzle is reduced when the pumping pressure is reduced. The expected size of the droplets is not listed like other Delavan atomizers since the normal use of this nozzle is in an industrial oil burning environment where droplet size is not as important a factor. Additionally, the team searched for independent ultrasonic nebulizers for sale. A few companies, including Sono-Tek were contacted but lackluster responses were given on if they sell their atomizers independently from their spray paint systems, which they are known for. No further responses from Sono-Tek were received.

Unfortunately, the Meinhard nebulizers were never received. The team proceeded to use the Delavan industrial oil burner nozzle, sold by Grainger. To reiterate there was no data available for expected droplet size. Thus, the team had to measure the performance of this atomizer. Results can be seen in section 4.2. The spray angle was said to be 70 degrees and the flow rate was modifiable, due to upstream pressure. This atomizer can be seen in Appendix B.

3.2 Burner FLUENT Modeling

3.2.1 Grid Independence Study

To understand the effect of the grid on the results, the outlet velocity profile for the optimized contour was produced for four separate meshes with varying element sizes. Figure 33 shows each of these meshes. And Figure 34 compiles the outlet velocity profile produced by each mesh for an inlet velocity of 0.45 m/s.

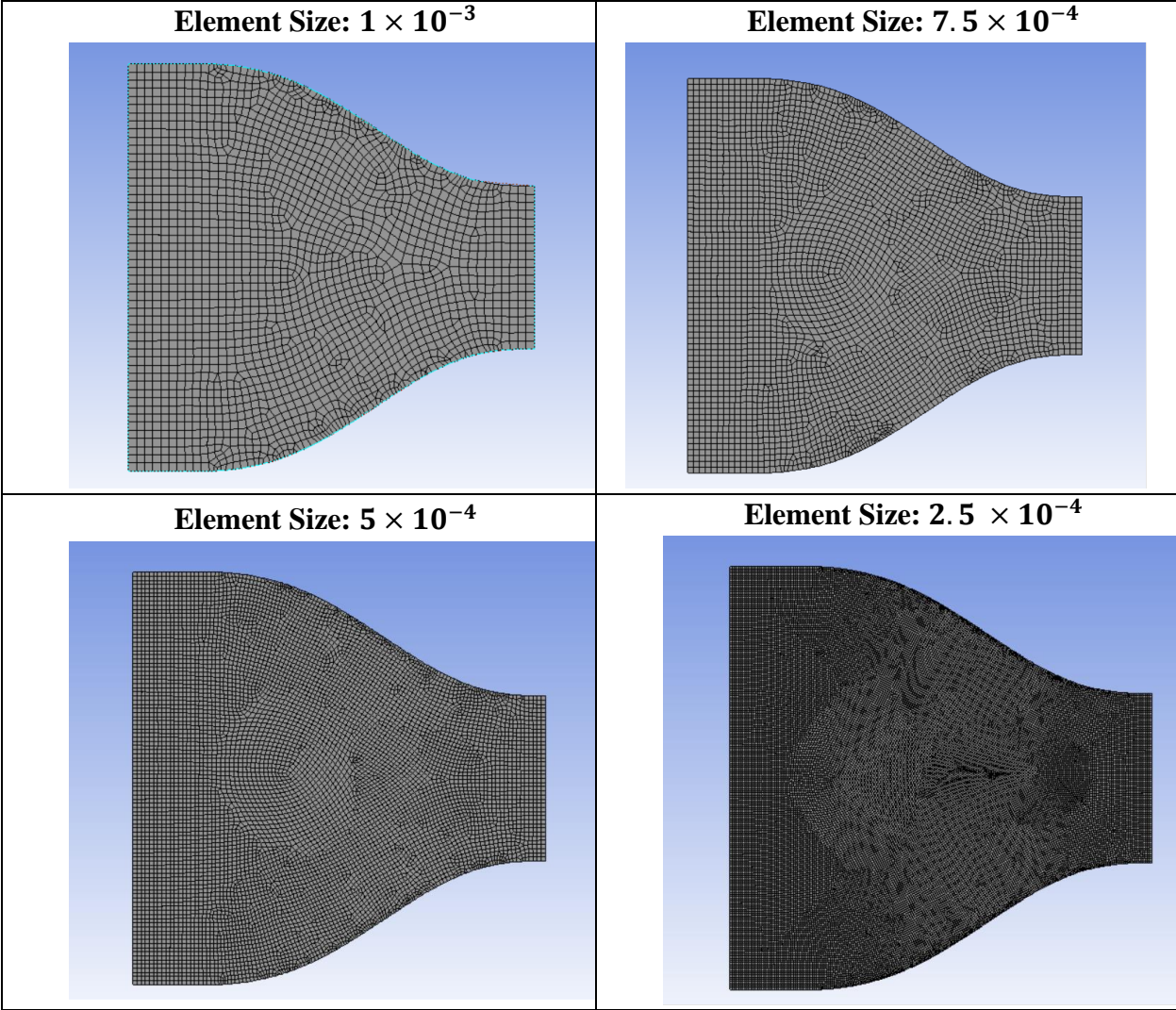


Figure 33: Four Meshes Characterized by Element Size

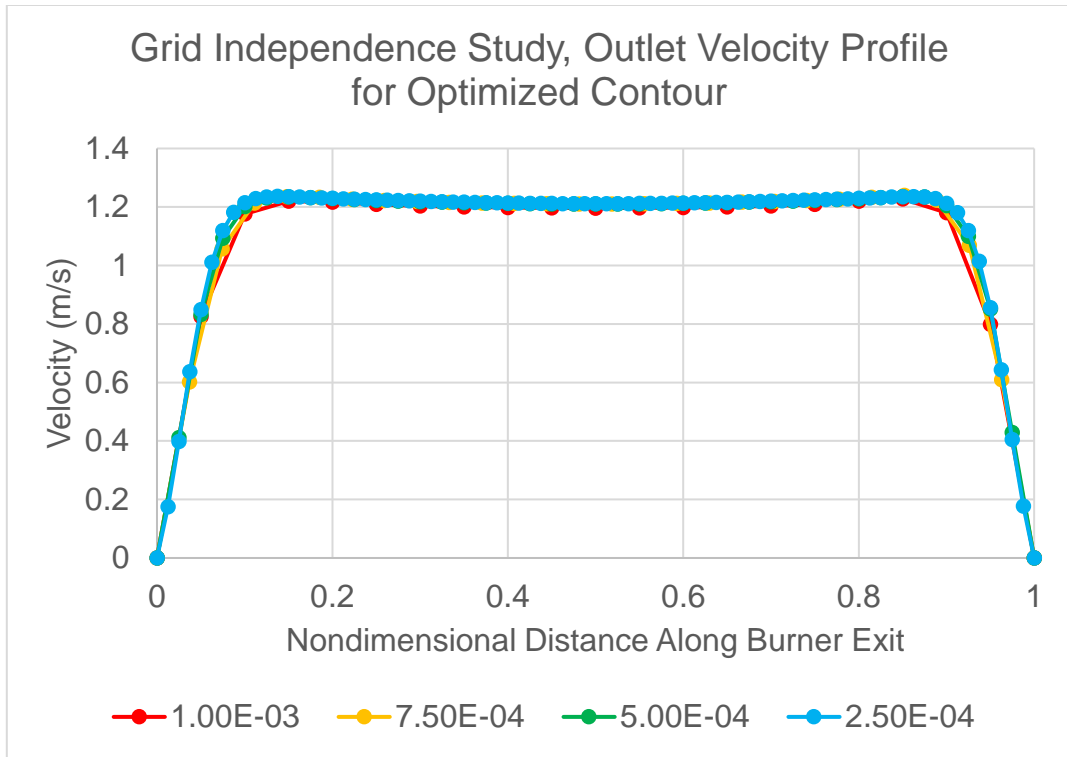


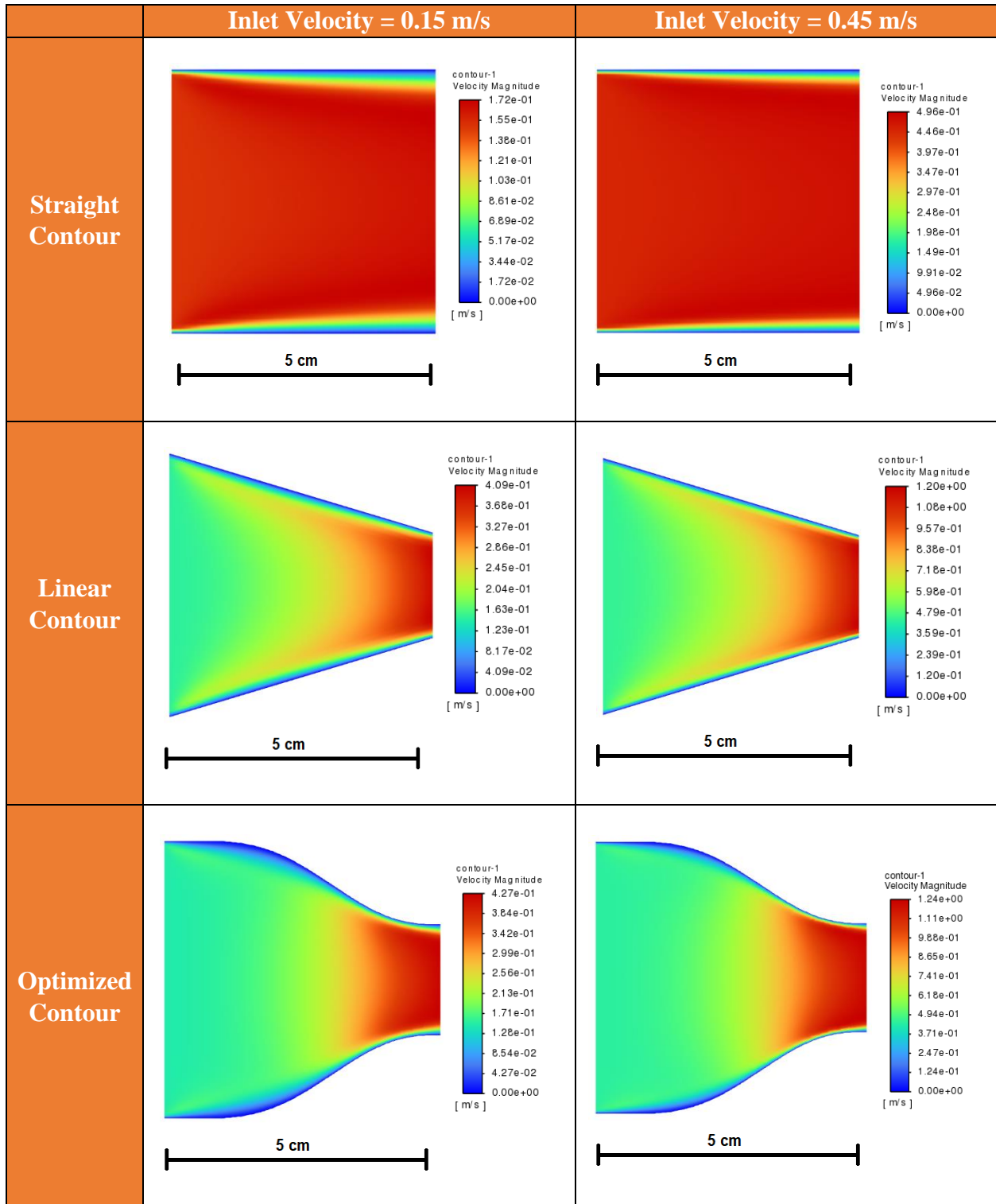
Figure 34: Outlet Velocity Profile for Optimized Contour for Four Meshes

From Figure 34, although there is some variation between the results from each mesh, it is quite minimal. Thus, it can be concluded that these results are grid independent.

3.2.2 Comparison Between Straight, Linear, and Optimized Contour

The performance of the optimized nozzle contour, based on the method used by Bergthorson, see Section 2.6, was compared with that of a straight and linear contour for two different inlet conditions. This was done to ensure that the optimized contour truly performs better than a typical design. The following table shows the total velocity magnitude across the three different contours under two different inlet velocity conditions. These two inlet conditions were chosen to capture the full range of exit velocities that need to be produced for future testing. Inlet and outlet pressures were set to atmospheric.

Table 12: Velocity Magnitudes Across the Straight, Linear, and Optimized Contours for Two Inlet Boundary Conditions



As seen on the above table, there is definite boundary layer formation for each contour type, even at an axial distance of 5 cm. It is also important to note that the boundary layer is much larger at the slower inlet velocity, which is expected. And lastly, for the optimized contour, the sudden change in curvature near the exit seems to result in a significant decrease in the thickness of the boundary layer.

The most important performance characteristic of the burner is its ability to produce a uniform exit velocity profile, to simplify flow calculations. The following two figures, Figures 35 and 36, show the outlet axial velocity profile at the two separate inlet velocities for each of the three contours.

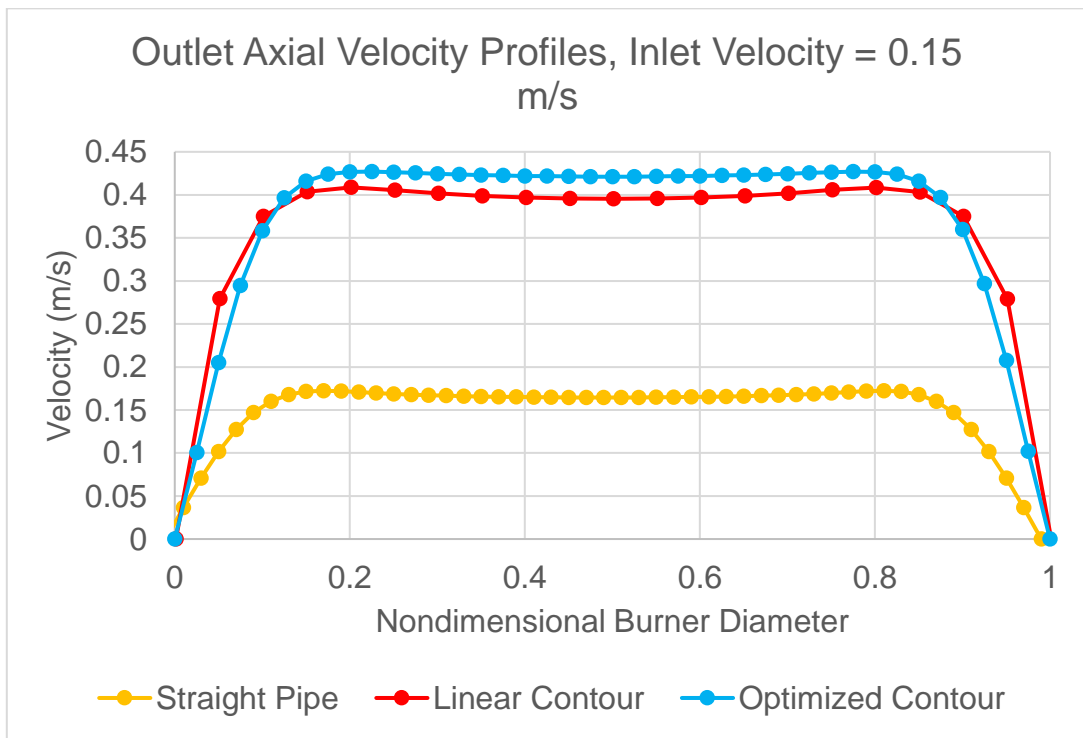


Figure 35: Outlet Axial Profile for Straight, Linear and Optimized Contour at 0.15 m/s Inlet Velocity Boundary Condition

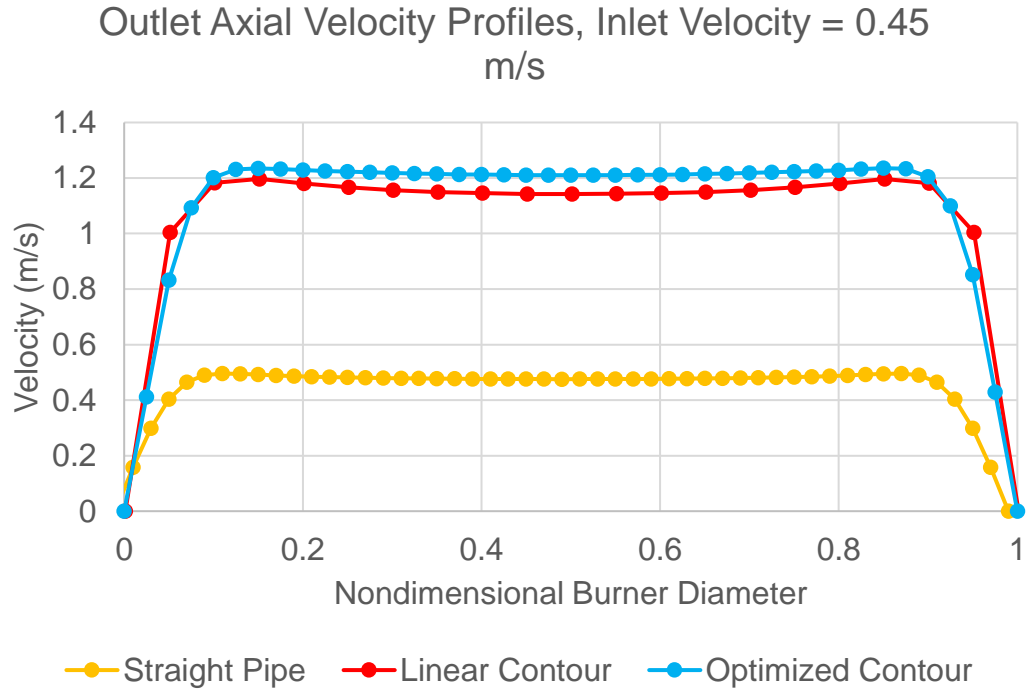


Figure 36: Outlet Axial Velocity Profile for Straight, Linear and Optimized Contour at 0.45 m/s Inlet Velocity Boundary Condition

Due to the difference in the exit diameters between the three contours, this distance was nondimensionalized with the respective exit diameter before the velocity profiles were compared. The outlet velocities differ between the straight and the linear and optimized due to the decrease in diameter for the latter two. The straight pipe’s diameter is constant, therefore, due to mass conservation, the velocity does not increase as much as it would for the other two.

For both inlet velocity conditions, the optimized contour does not produce an entirely uniform velocity profile. However, it does outperform the linear contour and straight pipe. The linear contour and straight pipe plots display a dip in the axial velocity at the center of exit diameter that is mostly absent in the optimized contour plot. To better understand the possible reasons for this, the radial velocity component is plotted for each of the contours in Figure 37.

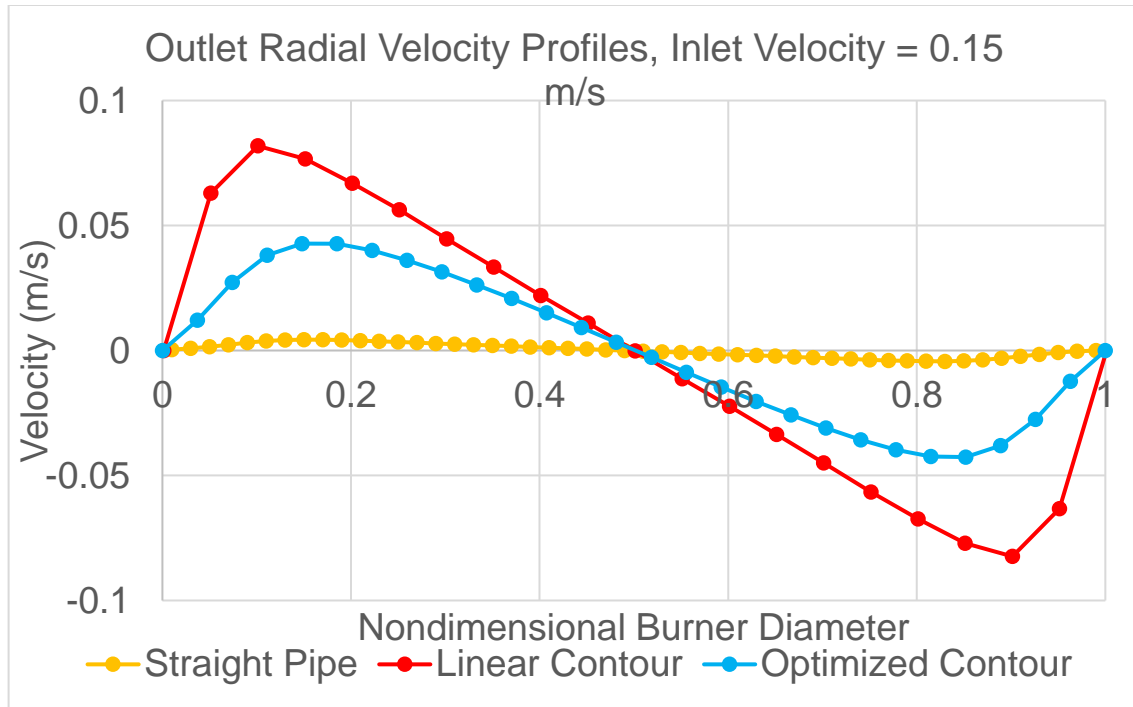


Figure 37: Outlet Radial Velocity Profile for Straight, Linear and Optimized Contour at 0.15 m/s Inlet Velocity Boundary Condition

The dip in the axial velocity for the linear contour can be explained by the large radial velocities seen in Figure 37. Although the straight pipe seems to perform better, this is due to the lower exit velocity magnitude and lack of curvature forcing flow in a radial direction. In an ideal contour, the radial exit velocity would be closer to zero. Overall, from these results, the optimized contour performs significantly better than the linear contour but could benefit from further improvements to its performance.

3.3 Fluid Flow Heat Transfer COMSOL Modelling

The team used COMSOL to generate a more in-depth theoretical understanding of the heat transfer occurring in the air flow subsystem of the experimental apparatus. This was done in an effort to design a cooling system that would meet the team’s desired air temperature condition –

265 Kelvin – while devising solutions for non-uniform temperature distributions. The goal of this model was to understand boundary conditions' effects on our experimental design to recreate relight conditions and how non-uniform temperature distributions would occur. In order to design a coolant system, the team had to understand how these cold gases would interact with the designed hardware in the experiment. The boundary conditions pertaining to the team's initial design were an outlet atmospheric pressure of 101325 Pascals, since validations and experimentation would first occur absent of the pressure vessel. Working with an inlet velocity of 45 cm/s and an inlet temperature of 261 K, an explanation of this value will follow. Again, the desired temperature of air mixing with the fuel is 265 K. Simplified hand calculations were completed alongside the computer-generated model to aid in understanding boundary condition effect on the design of the coolant system and the modeling itself.

To model and complete the hand calculations, the team focused on the temperature changes that appear prior to the nozzle, as those were the largest concern in the team's design for an experiment to recreate relight. Discussion of the heat transfer within the burner is later detailed in this section. A schematic for the problem modelled is shown in both Figure 38 and 39. It is important to note the dashed line appearing in both figures: this represents the midline of the theoretical apparatus and was noted here to further distinguish the studies were 2D axisymmetric. Figure 38 is the theoretical setup that the team's model and hand calculations were based upon. The numbers refer to key sections of the theoretical design, '1' refers to the air in a tank being pushed into the quarter inch pipe that the team has designed the flow system around. The segment numbered '2' displays where the theoretical pipe outlet enters the burner. In the team's designed burner, this is not the correct entrance but was designated here for easier explanation of air inlet temperatures. The control volume of the model and hand calculations is highlighted in blue.

Figure 39 displays the control volume magnified; this is the section of the apparatus that the coolant system would have to mostly be designed around. The segment numbered '3' depicts a 1/8-inch radius and '5' represents the area where a boundary condition of 1 atm and exit velocity of 45 cm/s occurs. The wall temperature is labelled number '4', originally set at room temperature, 298 K, and later 265 K, the desired relight condition. Since this model is axisymmetric, the dashed line represents the midline of the pipe and the study rotates along that axis. The length of the control volume is 12 inches for this study.

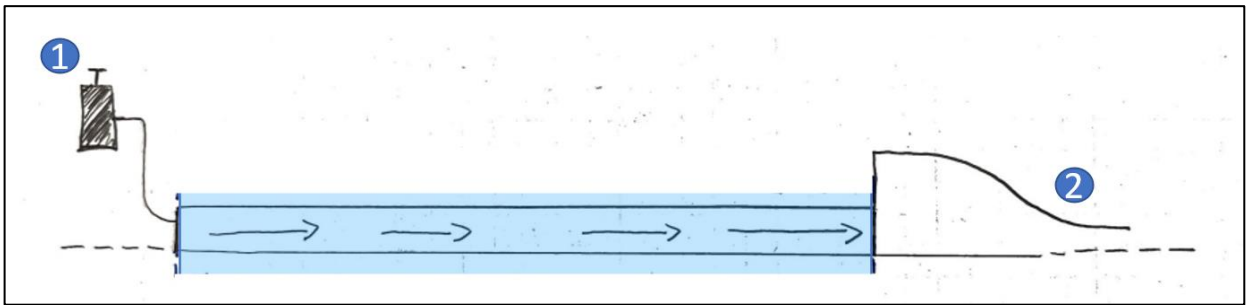


Figure 38: Schematic of 2D Axisymmetric Model Design

Used for both COMSOL modelling and hand calculations

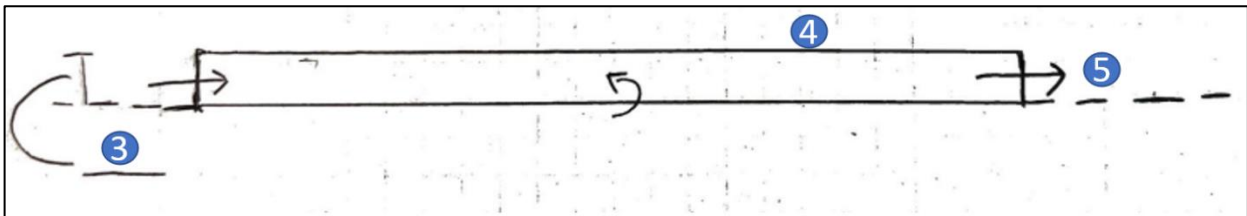


Figure 39: Schematic of 2D Axisymmetric Control Volume Design

Used for both COMSOL modelling and hand calculations

The hand calculations gave the basis for an initial guess for inlet temperature but did not consider radial temperature gradients due to assumptions and simplifications within these

calculations. Again, the team wanted to have the oxidizers and fuels meet at desired temperatures. The hand calculations were performed for the same setup as shown in the Figure 39, directly above. The pipe was assumed to have a constant wall temperature of 298 K, a 12 in pipe, a radius of 1/8 inch, and the same boundary conditions stated previously. For calculating the heat transfer of laminar air flow through a constant surface temperature pipe, the team followed the University of Colorado Boulder's method shown on the school's LearnChemE webpage, uploaded in 2013. The assumption in this method is that there is no radial temperature gradient, which is not realistic. This initial calculation was used to get a baseline inlet air temperature of 260.9 K, rounded to 261 for modelling purposes.

The team's fundamental model simulated the heat transfer within a pipe with a diameter of a quarter inch and a length of 12 inch, the schematics are the same as previously stated and shown directly above. The model is 2D axisymmetric, allowing for resolution of all three dimensions to be understood. The team made this decision utilizing the symmetry of a cylindrical pipe. Each cross section of the pipe was created as rectangle and rotated around 360 degrees. The problem is a bit complex as the fluid flow and heat transfer need to be modeled simultaneously. Boundary conditions consisted of an inlet velocity of 45 cm/s, a pipe inlet temperature of 261 K, and an outlet pressure of 1 atm, developed from the simplified hand calculations. Originally, the wall temperature was set to 298 K, room temperature. The air flow through the pipe was laminar and fully developed. Figure 40 and 41 display two distinct views of the heat transfer simulation. There is a large heat differential separating the outlet and inlet, over a 30 K difference. Putting cold air and letting it heat up throughout the piping is not a good coolant system design unless the air system was less than a foot long. Due to the laboratory environment this is not the case. On top

of that issue, there is a clear variation in radial temperature which the team’s coolant system must take into account. Radial temperatures are plotted on Figure 42 and 43.

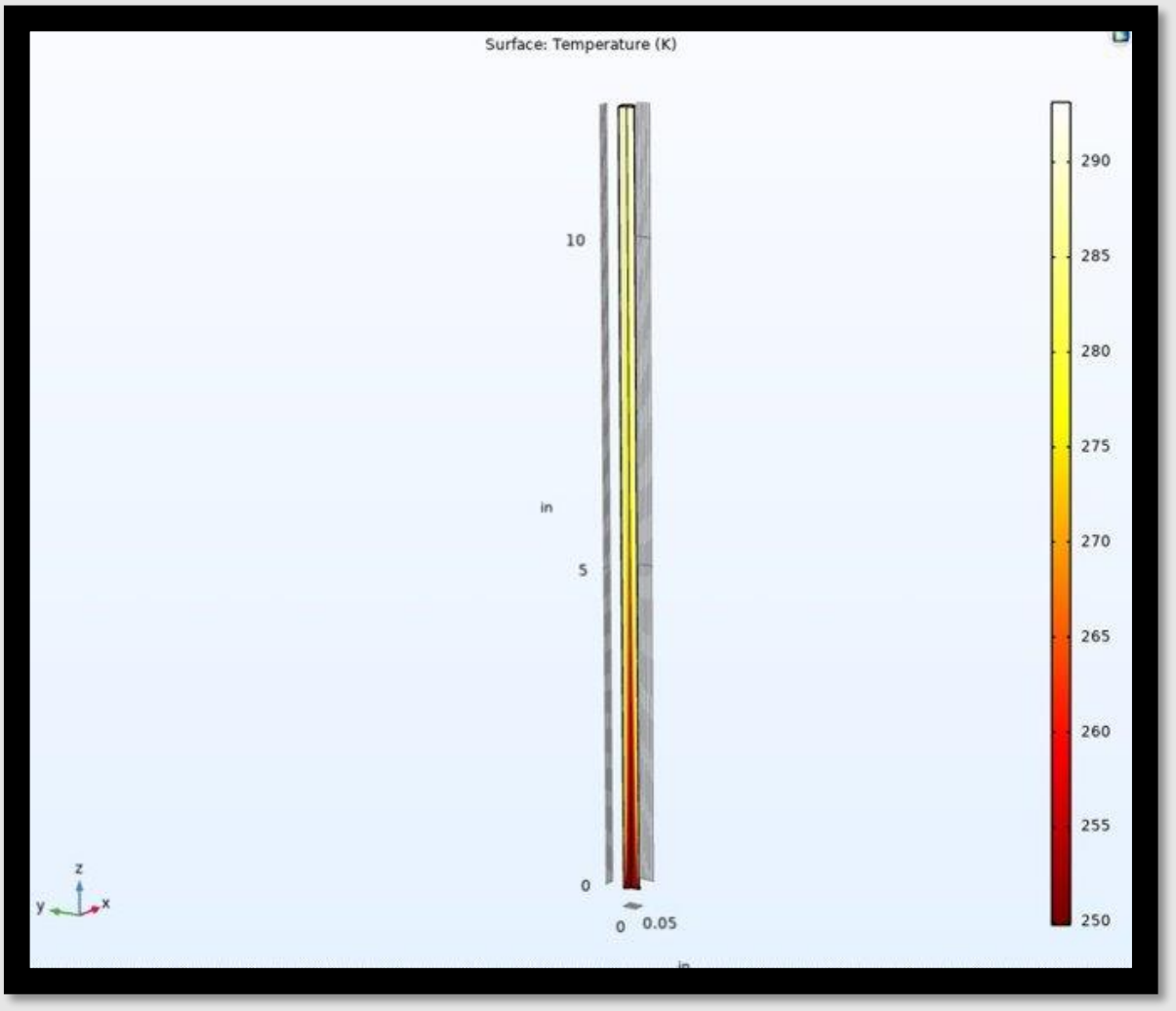


Figure 40: Complete COMSOL Heat Transfer Study

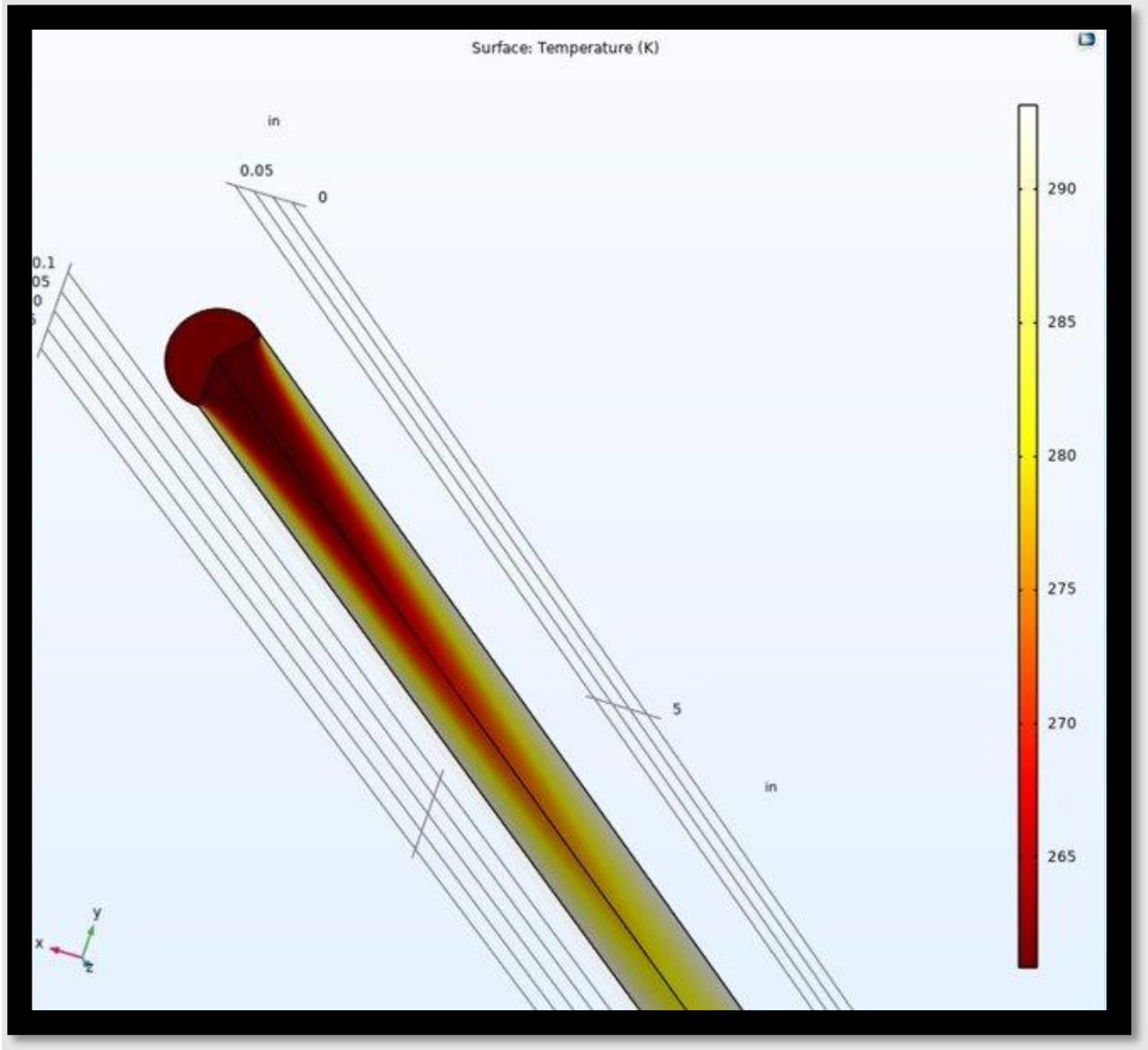


Figure 41: COMSOL Heat Transfer Study Another POV

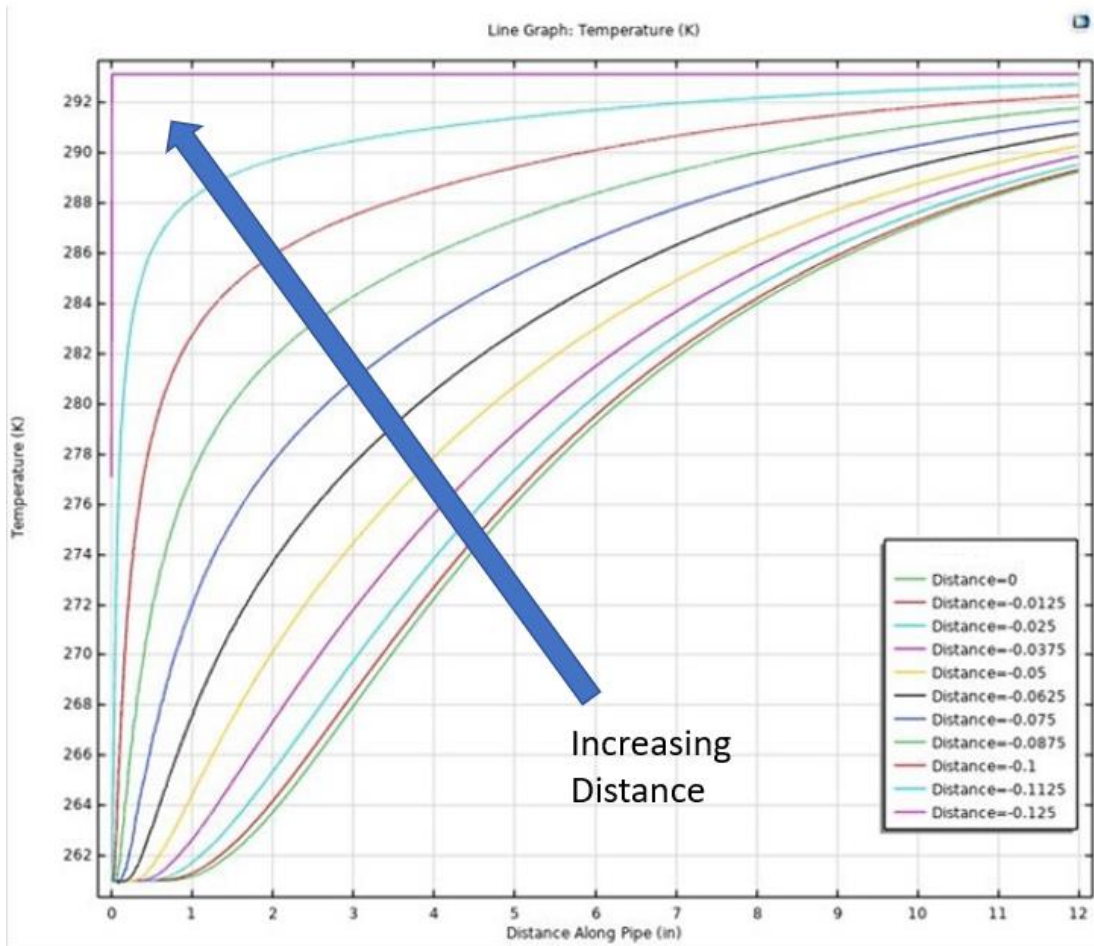


Figure 42: Temperature as a Function of Pipe Length of Complete Heat Transfer Study, Each line represents a different radial cut of the pipe starting at the center and moving 0.0125 inch each cut. The arrow depicts an increase in radial distance from the center line.

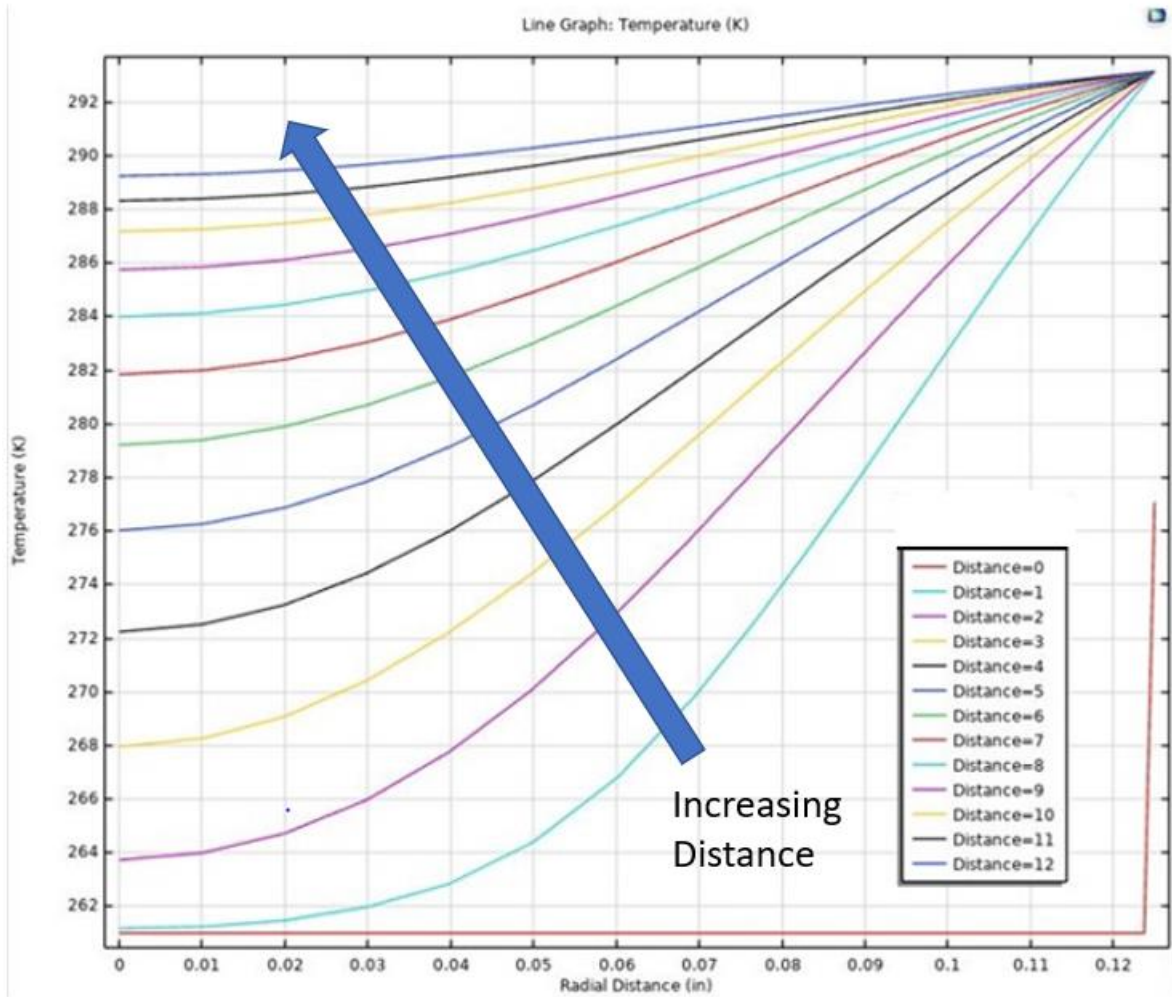


Figure 43: Temperature as a Function of Radial Distance of Complete Heat Transfer Study, Each line represents a different cut of the pipe’s length starting at the inlet and moving 1 inch each cut. The arrow depicts increasing pipe lengths from the inlet.

The radial heat differentials are the key information for the team’s design of an experimental apparatus. Radius of the pipe versus temperature can be seen in Figure 42. Each line is a different segment 1 in. down the pipe. On the following figure, Figure 43, temperature is graphed versus pipe length, with each line representing a tenth – 0.0125 in – of the pipe’s radius. As can be seen, the radial temperature difference is quite large. The team realized that it was best to disturb the

fluid flow in the pipe, disrupting heat boundary layers, and balancing the heat across the radial distance. The fluid can be disturbed in this part of the experimental apparatus since there are flow smoothing devices at the entrance to the burner, thus disturbance here would not affect downstream laminar conditions. 3D-printed bumps, ramps, and wedges could be fashioned to place in the pipes inlet to disrupt the flow. Vortices and flow stagnation near the walls of the pipe would have to be disrupted.

Once the design process to get the gas flowing through the pipe more uniformly had begun, reducing the temperature of the gas entering the pipe and exiting the burner had to be further considered. Since the desired temperature of the gas entering the burner is 265 K, the cooling system was modelled. Figures 44-46 are the coolant system design simulation plots and their respective insights on heat transfer are displayed. The boundary conditions and control volume remain the same except for the surface temperature, which is now 265 K, the desired temperature at the outlet. Figure 44 shows the 3D view of the pipe with the temperature gradient. Figures 45 and 46 show the radial and pipe length temperature differentials, respectively. The outlet temperature can now be seen to be much more uniform temperature at 265 K as desired. A coolant system that keeps these wall temperatures at 265 K and the inlet at 261 K is necessary when the piping prior to the burner is one foot long. If longer piping is introduced and the inlet and surface temperature is maintained the outlet should still be 265 K.

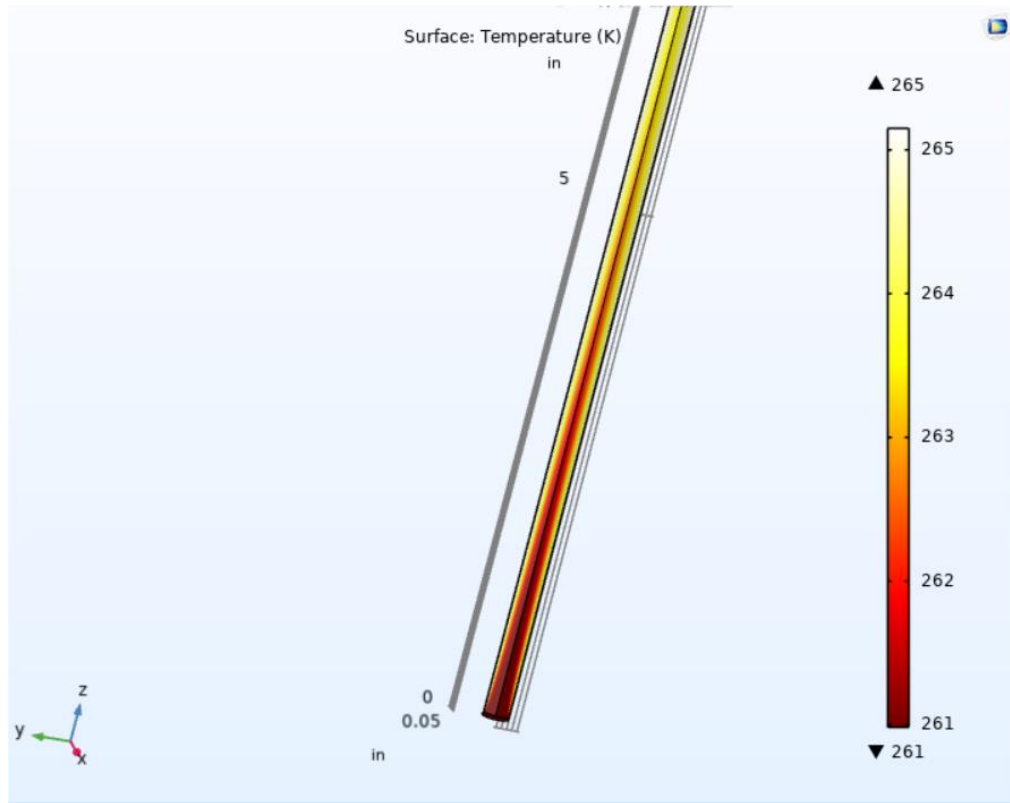


Figure 44: Coolant System Heat Transfer Model for Coolant System

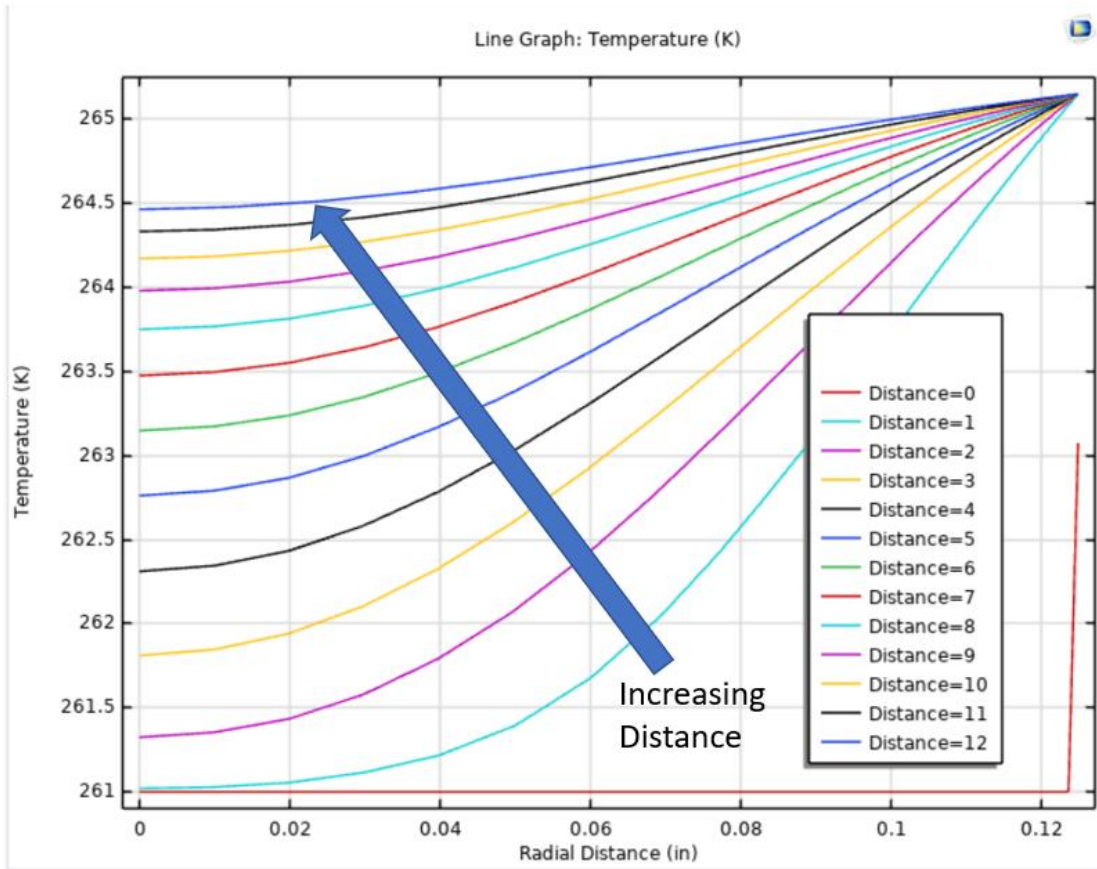


Figure 45: Coolant System Temperature Versus Radial Distance of Complete Heat Transfer Study. Each line represents a different cut of the pipe's length starting at the inlet and moving 1 inch each cut. The arrow depicts increasing pipe lengths from the inlet.

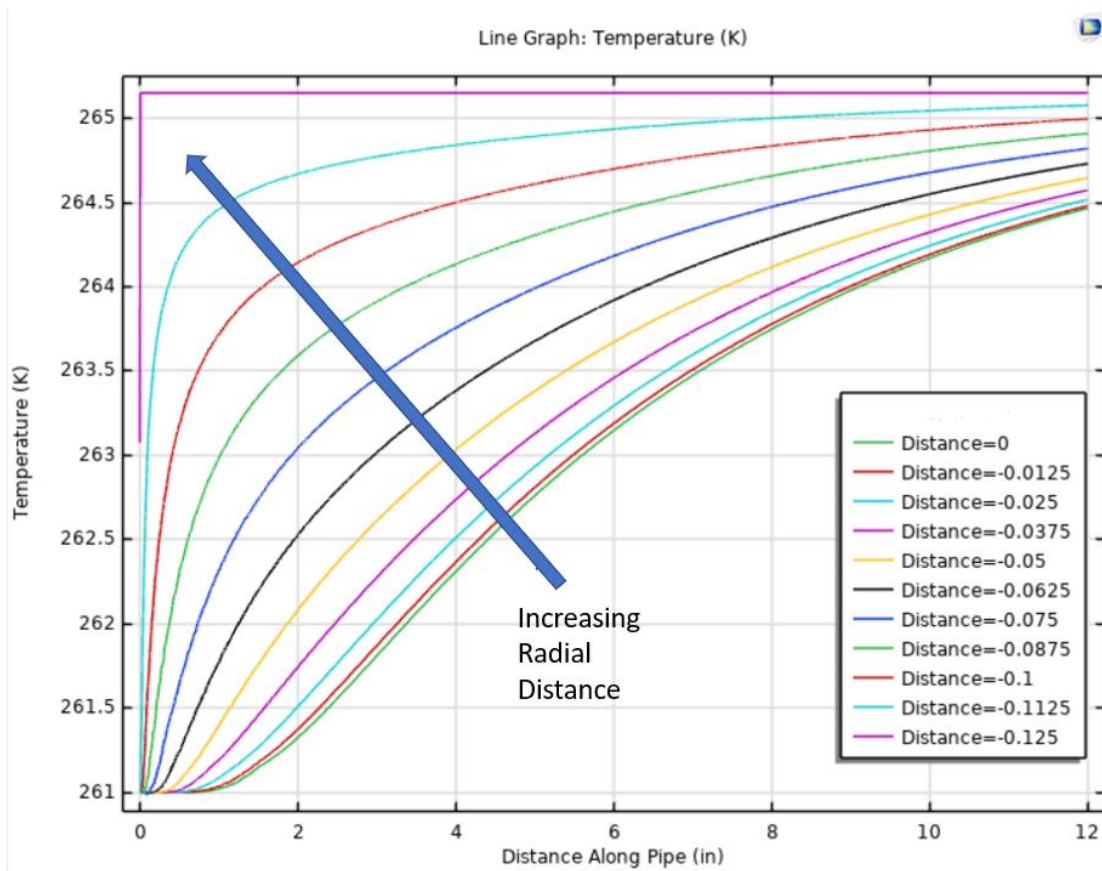


Figure 46: Coolant System Temperature Versus Pipe Length of Complete Heat Transfer Study, Each line represents a different radial cut of the pipe starting at the center and moving 0.0125 inch each cut. The arrow depicts an increase in radial distance from the center line.

A coolant system must enforce a uniform outlet temperature of 265 K by keeping the pipe temperature at 265 K, providing an inlet temperature of 261 K, which keeps the minimum pipe length at 12 in, and implementing the flow disturbing devices discussed earlier. A costly solution that has flexibility in temperature ranges for the inlet temperature is an industrial heat exchanger from Xchanger Incorporated. The flexibility of temperature would be necessary for different tube lengths. If the inlet temperature is 261 K, as modelled the pipe can be as long as needed if the pipe's surface is kept at 265 K, a liquid nitrogen bath is discussed later to implement this. If the

inlet temperature is greater than that of the pipe temperature, the longer the tube length would mean more heat is transferred and lost from the fluid within the pipe to the pipe. If further designs and desired testing could cope with hotter temperature fluids, which are less comparable to re-ignite conditions, vortex coolers could be employed for the inlet. These coolers use compressed air to inject into a specially designed chamber to create two streams of air, both hot and cold. The cold air could be used, and the hot air ejected. Shown below on Figure 48b is a standard vortex cooler. The compressed air splits into the cold and hot streams-left and right respectively. Certain vortex tubes have been seen to reach 223 K, if implemented correctly (Walker, 1975). Since this would have to be created out of an industrial setting, flexibility and repeatability might be a larger challenge. However, the cost difference could be the decider, with some heat exchangers reaching the range of \$2000-4000. The size could cause additional strain when connecting to an experimental apparatus; heat exchangers can be multiple feet long by multiple feet thick. A diagram of a heat exchanger can be seen in Figure 48a. Further expansion of this experimental design is required to keep the air cool by creating a constant pipe surface temperature of 265 K. A somewhat inexpensive solution to this is a liquid nitrogen cooled system. Liquid nitrogen can flow over to surround metallic piping to cool the liquid to a desired temperature by keeping the pipe surface temperature a constant 265 K. However, the fully developed design of this liquid nitrogen steady state coolant system is out of the scope of this project. Ideally, if your inlet temperature is 265 K and the pipes are held at 265 K, through a liquid nitrogen encasement, the piping could be any length. However, maintaining a perfectly uniform and precise inlet temperature either at 265 K, 261 K as modelled, or below may not be feasible. If further tests can only provide an inlet temperature equivalent to room temperature, 298 K, the piping length would have to be at least 20 in long and preferably above 25 in. This will force the room temperature air to become a uniform

265 K at the outlet. The piping would still all have to be held, through liquid nitrogen cooling, at 265 K, this room temperature inlet case can be seen on figure 47, where the fluid becomes radially uniform and 265 K at around 20 in.

Finally, the burner must be discussed since it can be expected that at least some heat transfer occurs within the burner. The team believes this heat transfer to be negligible for several reasons. Firstly, for major heat loss to occur the fluid needs to flow over a comparatively longer distance. Since the burner is 5 cm, or around 2 in, this is not a huge distance to cover. Secondly, the flow system could be run for a period through an insulated burner causing the burner material to slowly lose heat to the flow. Eventually the temperature of the burner gets colder, and experimentation can take place at this point. The flow, thus, loses even less heat to the burner. If large flow heat loss is experienced within the burner, and a cause for concern, the liquid nitrogen encasement should be extended to encompass the burner keeping the burner at the same 265 K temperature desired. This would create an equilibrium between the flow at 265 K and the burner at 265 K so there would be no heat loss.

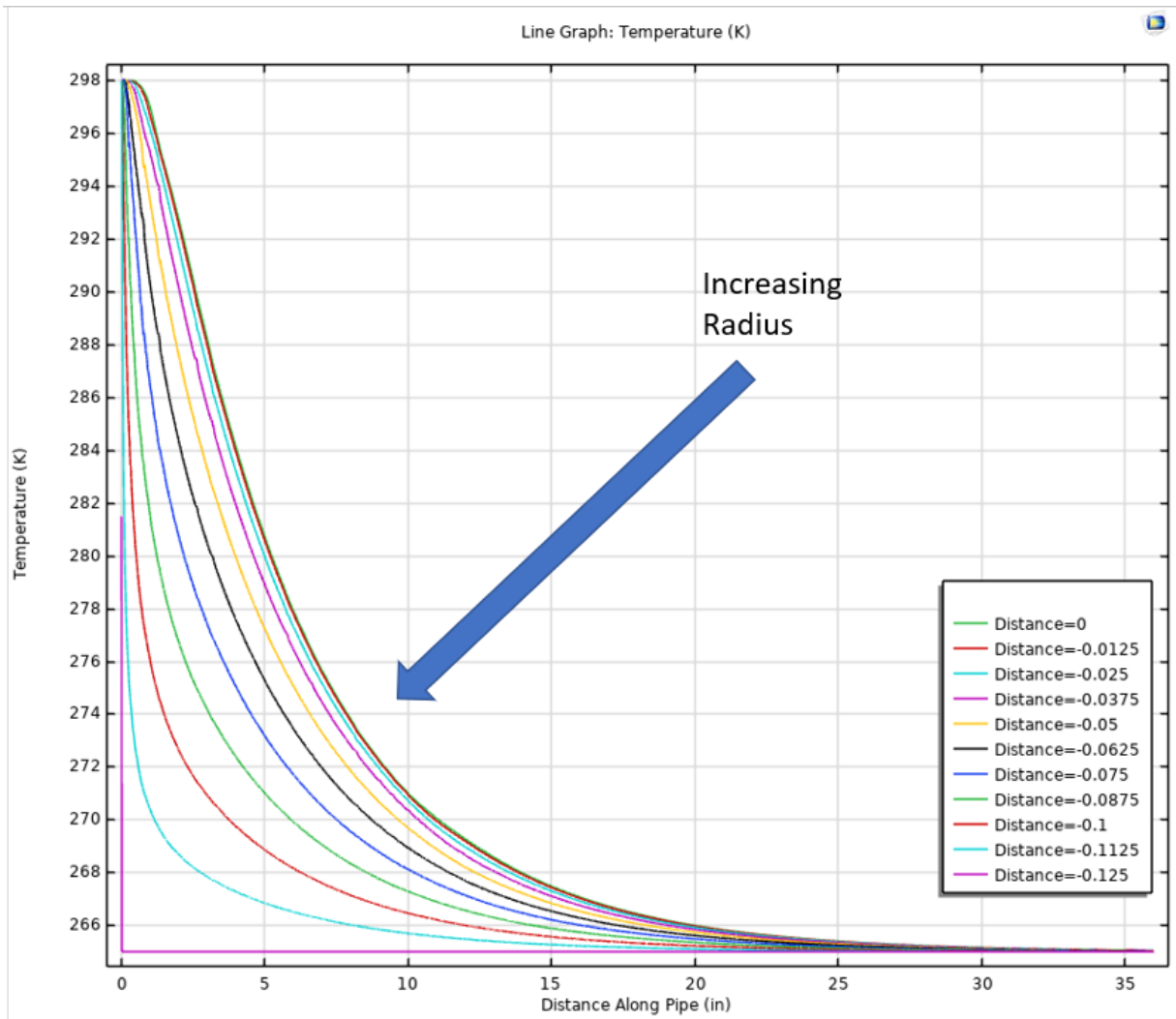


Figure 47: Room Temperature Inlet Model of Temperature Versus Pipe Length

Each line represents a different radial cut of the pipe starting at the center and moving 0.0125 inch each cut. The arrow depicts an increase in radial distance from the center line.

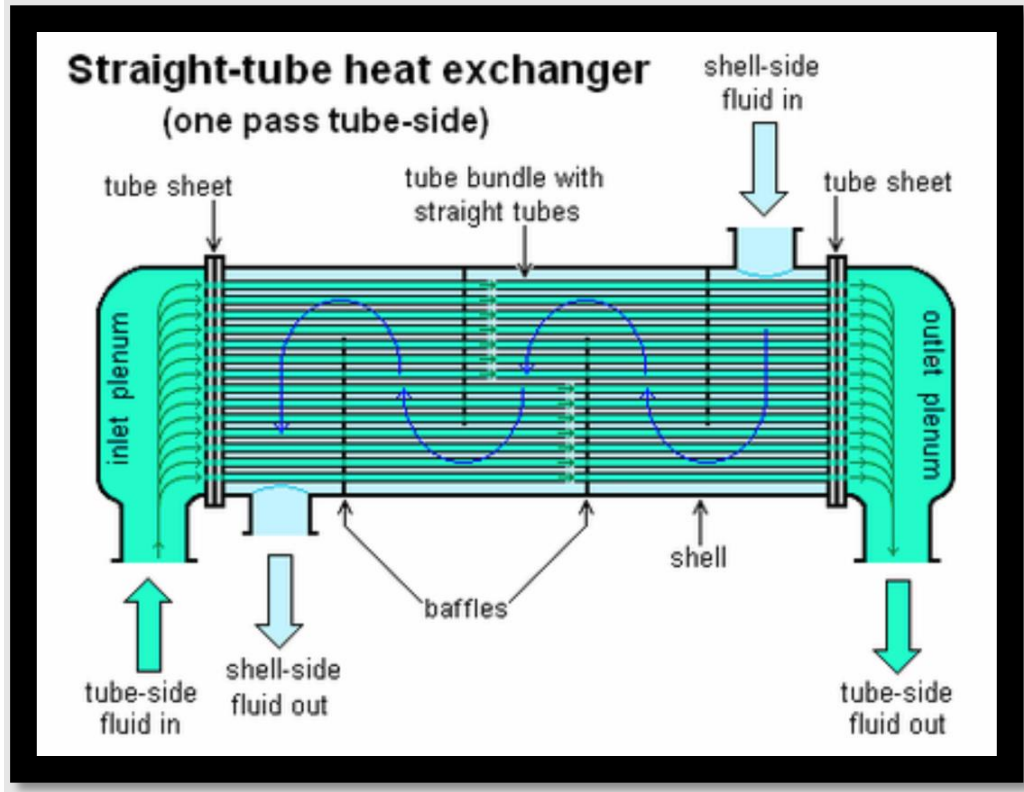


Figure 48a: Heat Exchanger Diagram (Wikipedia, “Heat Exchanger”)

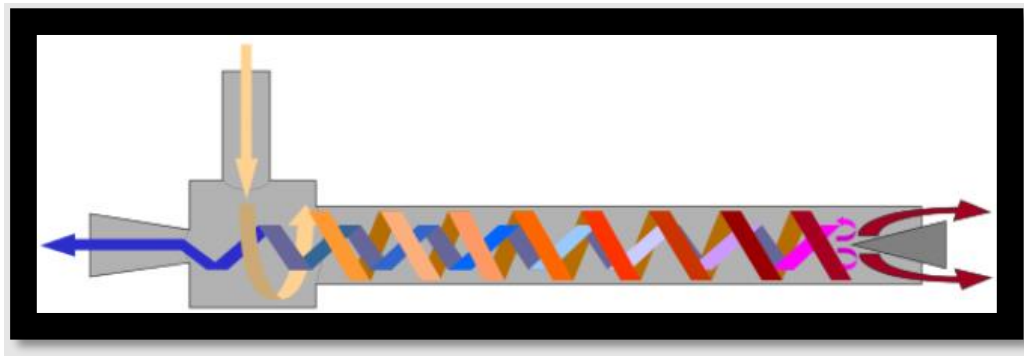


Figure 48b: Standard Operation of a Vortex Cooler (Wikipedia, “Vortex Tube”)

3.4 Pressure Vessel Analysis

Analysis of the CAD model of the pressure vessel was completed using ANSYS Static Structural. This software allows for stress calculations and deformation calculations caused by

exerting pressure on the inside of the vessel. Modeling was run at the expected pressures of the experiment and at the max pressure of the vessel. A grid independence study was conducted by fixing one of the larger diameter flanges at the ends of the vessel. Setting it in place will stop external or internal forces from shifting the vessel at this point, simulating real use with an end being restrained. The results of the forces only cause deformation and not translational movement because the body is fixed. The internal force is uniformly distributed normal to every internal surface. The study was done using an element size of .005 and .007 m and the max pressure found was exerted to see if the different meshes converge to the anticipated results. The meshes are more compact at the windows because of the difference in material from the vessel and the window. Figures 49-50 show the meshes.

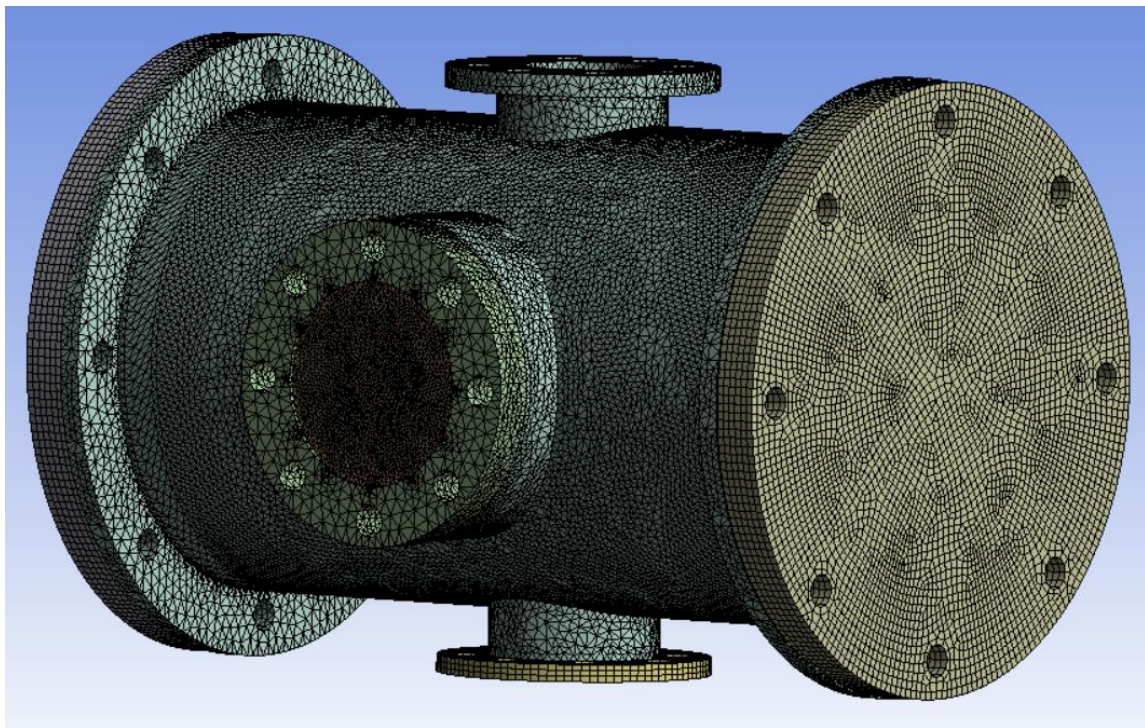


Figure 49: Element Size 5×10^{-3} m with Displacement of 0 m on Main Body of Vessel and Internal Pressure of 250000 Pa

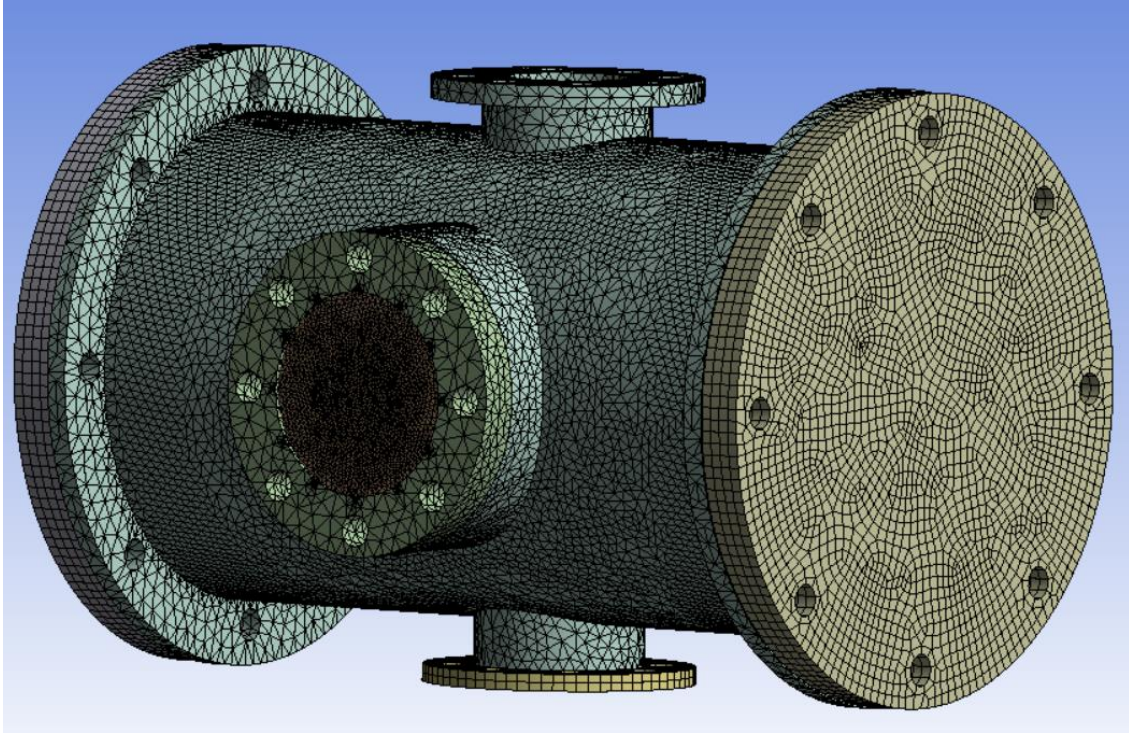


Figure 50: Element Size 7×10^{-3} m with Displacement of 0 m on Main Body of Vessel and Internal Pressure of 250000 ka

The figures below show the stress analysis of the vessel with the element sizes above.

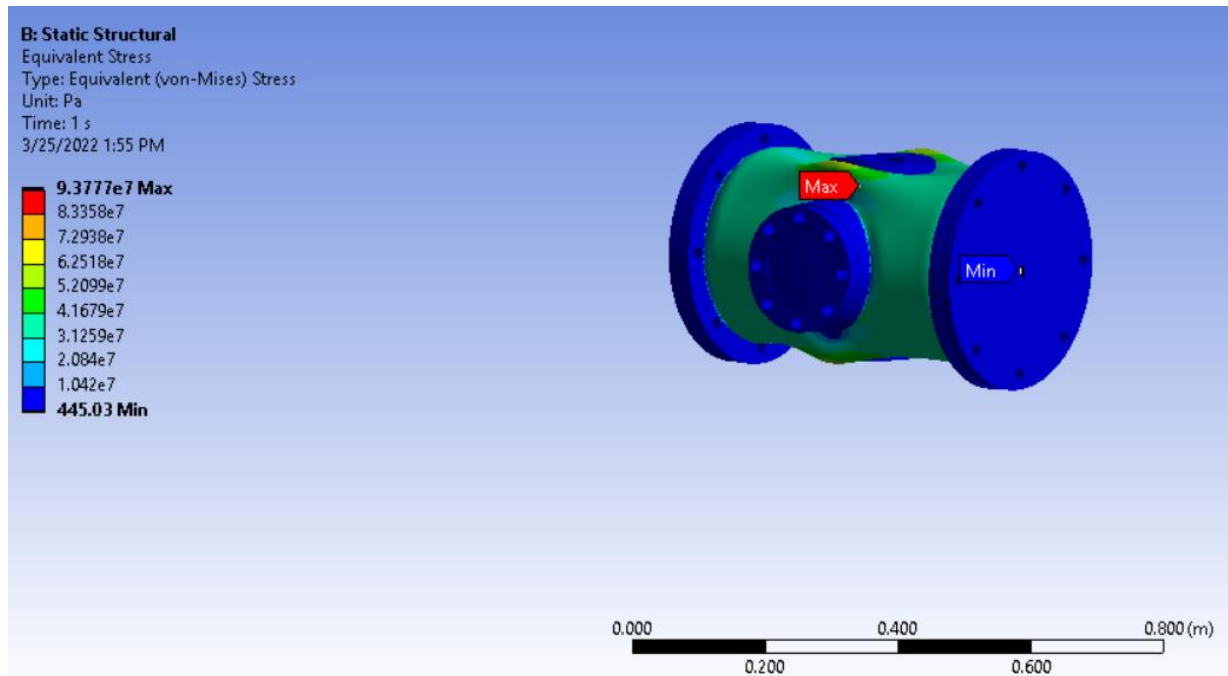


Figure 51: Stress Analysis of Element size 5×10^{-3} m with Displacement of 0 m on Main Body of Vessel and Internal Pressure of 250 kPa (Units in Pa)

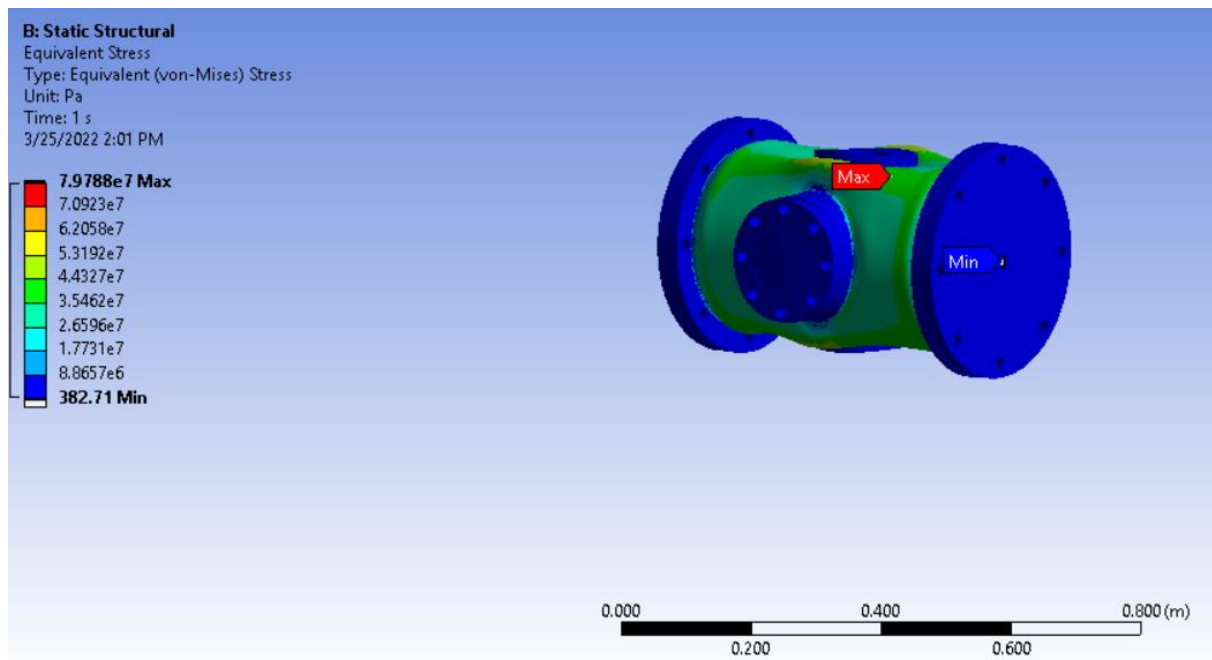


Figure 52: Stress Analysis of Element size 7×10^{-3} m with Displacement of 0 m on Main Body of Vessel and Internal Pressure of 250 kPa (Units in Pa)

From Figures 51 and 52, the minimum stress has difference of around 15 % and the maximum stress has a difference of around 15 %, depending on the element size of the grid. Full grid independence is not reached since the results from the simulations with two element sizes are not the same.

Figures 53-54 show the stress analysis and total deformation of the vessel at 250000 Pa. These results are preliminary and due to insufficient time, the design of the vessel was not complete.

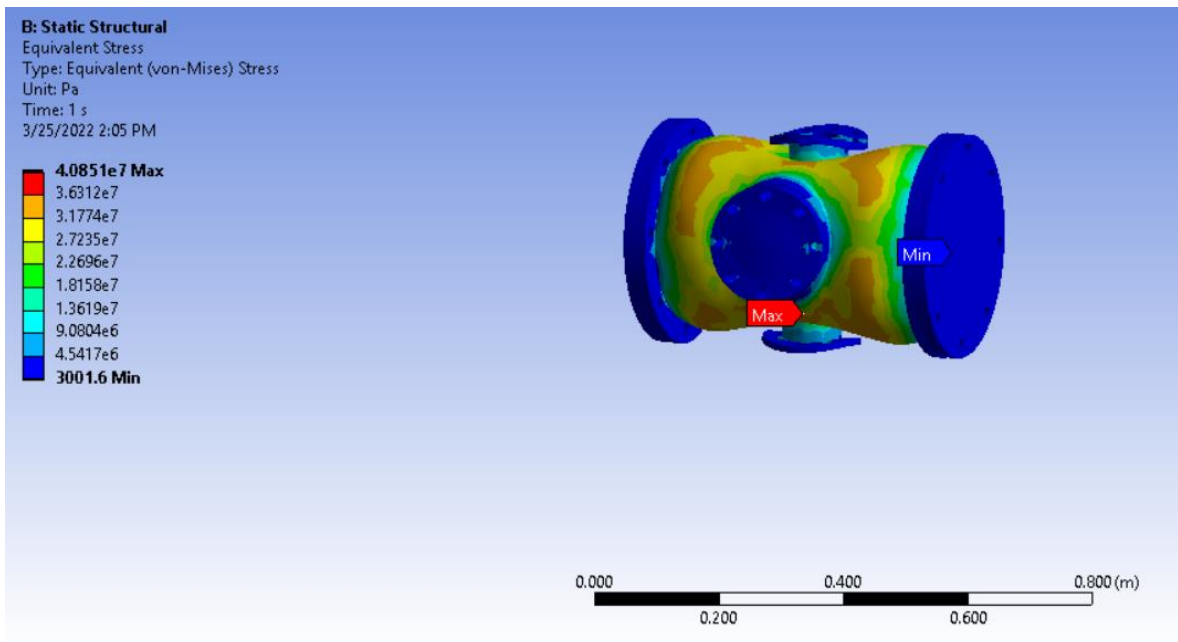


Figure 53: Equivalent Stress of Pressure Vessel External with Displacement of 0 m on Main Body of Vessel and Internal Pressure of 250 kPa (Units in Pa)

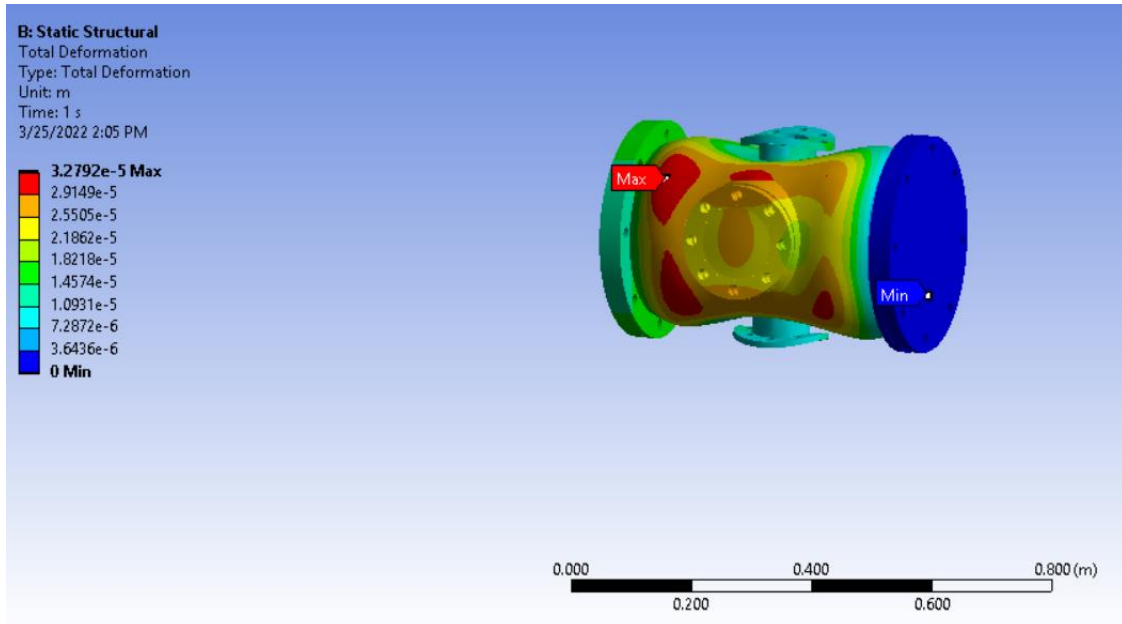


Figure 54: Total Deformation of Pressure Vessel External with Displacement of 0 m on Main Body of Vessel and Internal Pressure of 250 kPa (Units in m)

4 Experimental Results

Tests were conducted to validate the experimental apparatus. This section details the results of these validation tests.

4.1 Particle Image Velocimetry Testing

The SOLIDWORKS model of the burner, designed with the application of the Bergthorson optimization scheme, was 3D printed to begin running particle image velocimetry (PIV) testing to validate if the burner's exit velocity profile was indeed uniform. These tests were conducted in tandem with the modeling discussed in Section 3.2 Burner Fluent Modeling. Figure 55 depicts a schematic of the experimental setup. Figures 56 and 57 depict components of this setup. Other parts can be seen in Appendix B.

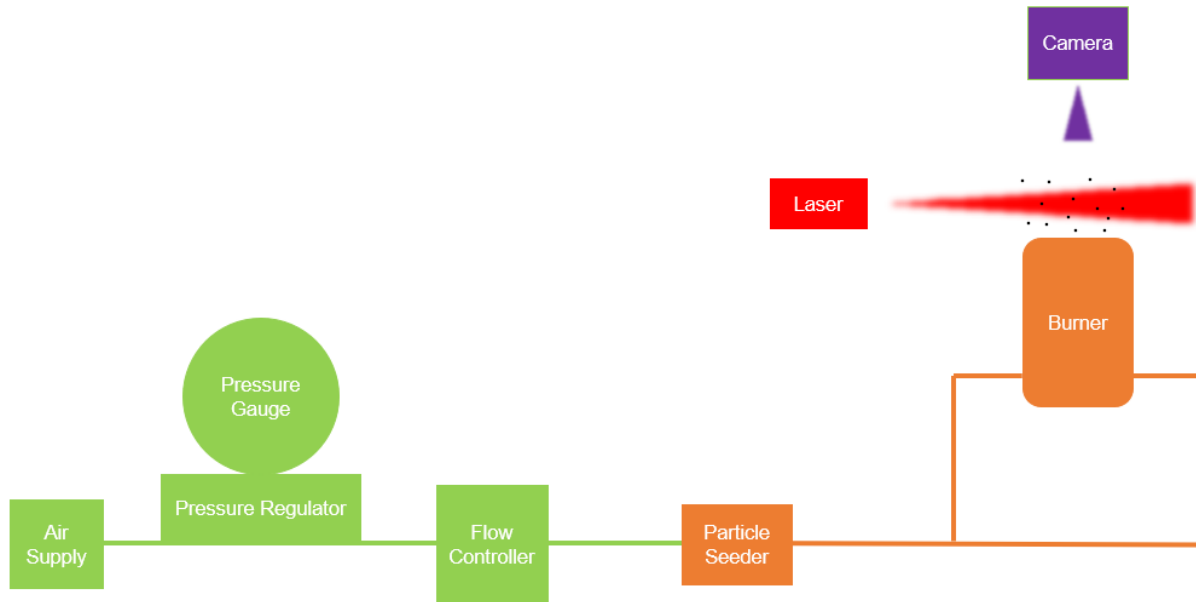


Figure 55: Experimental Setup for Particle Image Velocimetry Testing



Figure 56: Experimental Setup Featuring the Burner and Laser, Focused by 3 Lenses

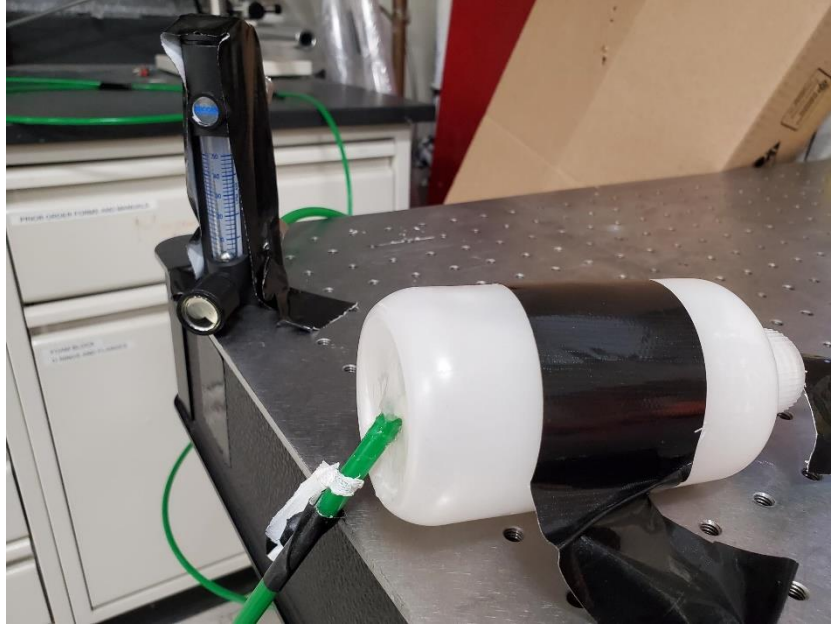


Figure 57: Experimental Setup Featuring Particle Seeder and Flowmeter

Testing was conducted at 30 SLPM, leading to an exit velocity of 1.59 m/s. A Cavilux Smart Laser was paired with a Photron FASTCAM NOVA high-speed camera to capture particle movement. Particles of talcum powder were introduced into the flow as the seeder particles. These particles were placed in a holding chamber through which airflow was allowed to pass, the airflow picking up particles along the way. With a laser repetition rate of 1 kHz, the expected particle movement between pulses is 1.59 mm. Figure 58 depicts two of the pictures captured during testing. Figure 59 displays the parameters used to analyze this test in the Open PIV software (Ben Gida et al., 2020). And Figure 60 displays the results.

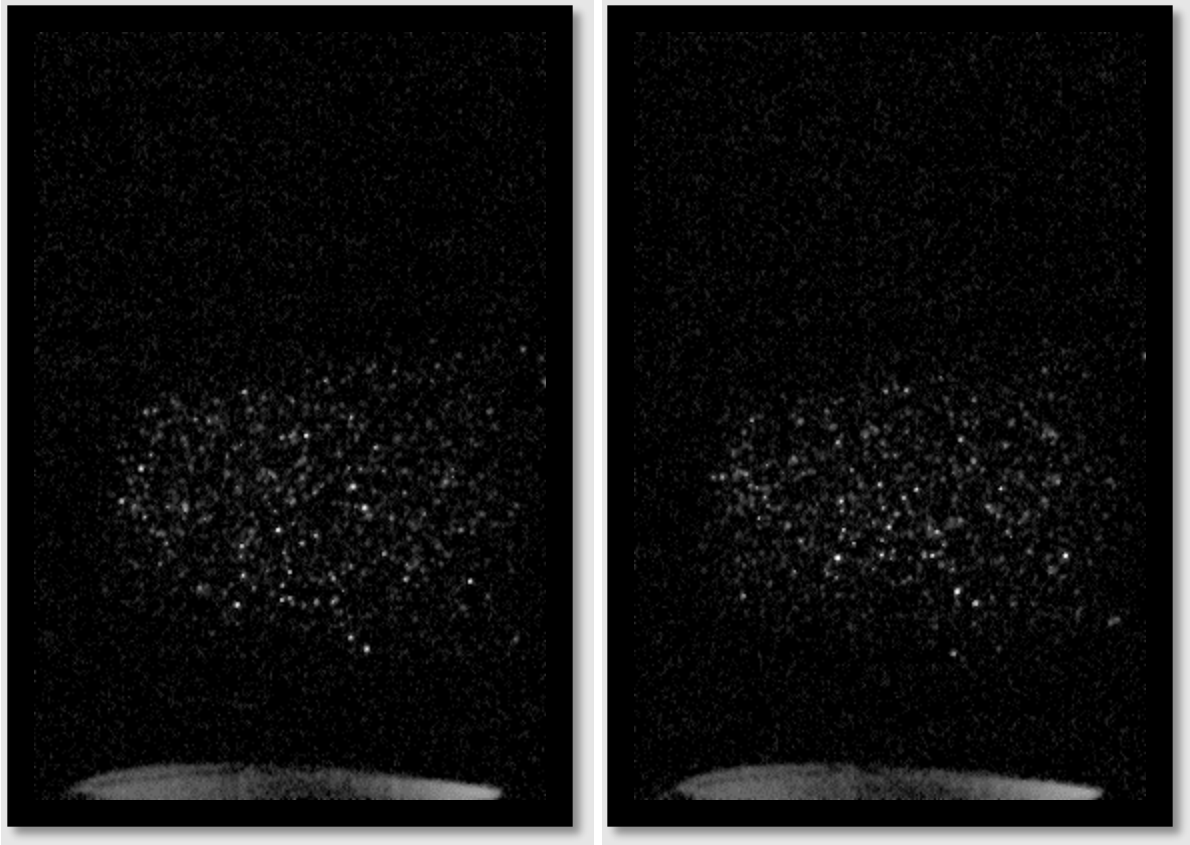


Figure 58: Images Captured with High-Speed Camera

Interrogation window size	
Width	Height
128	128
Spacing/Overlap	
Horizontal	Vertical
16	16
S/N type	2
S/N value	1
Scale (m/pix)	0
dt (sec)	1
Outlier filter	100
Jump	1

Figure 59: Open PIV Settings Used to Conduct Analysis

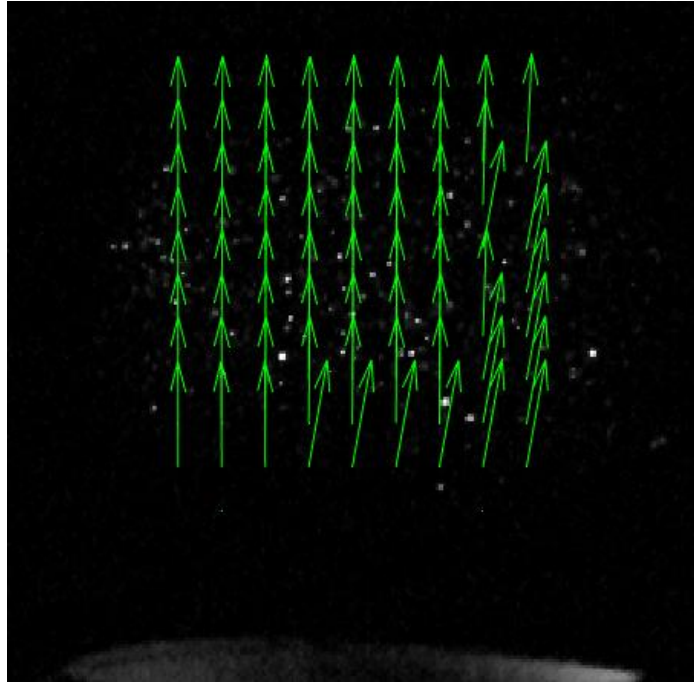


Figure 60: Open PIV Results for 30 SLPM, 1 kHz

The width of the pictures is the same as the diameter of the burner, 20 mm. The width of the pictures is 256 pixels, thus each pixel corresponds to 0.078 mm. The average axial displacement through the Open PIV analysis was found to be 20.33 pixels, corresponding to 1.588 mm. This is practically the same as the expected displacement of 1.59 mm. There is also some radial displacement, averaging 0.1104 pixels, or 0.0086 mm. Hence the velocities measured using PIV agree with those estimated from the flow rates.

The visual results indicate that the flow is largely laminar. However, some regions of the flow show deviation from the vertical path. This could be due to remnants of flow that have not been fully flattened after traveling through the mesh and burner contour. Another reason for this deviation from the uniform flow profile could be external disturbances from the vent present above and to the right of the experimental setup. Additionally, the seeder particles mixed within the flow might not have been homogeneously distributed causing flow disturbances. To get more accurate

results, it is recommended that the experimental setup is placed directly below the vent, rather than at an angle.

4.2 Droplet Sizing

Not much information was available regarding the droplet size performance of the atomizer used in the experimental apparatus, the Delevan Type B Oil Burner Nozzle. Thus, tests were conducted to understand the range of droplet sizes produced by the atomizer at various distances downstream of the burner. Water was fed into the atomizer's inlet, pressurized airflow behind it acted as a piston applying pressure to the water itself. Droplets emitted by the atomizer were captured on a nonabsorbent surface for three seconds and then immediately examined under an optical microscope. This was conducted for an upstream air pressure of 30 psi for four different distances: 5 in, 5.5 in, 5.75 in, and 7 in. First, tests were done for 5 and 7 in. From these results, it was decided that the distances of 5.5 in. and 5.75 in. should be tested to try to optimize the droplet sizes for water. Figure 61 displays the experimental setup for these tests. Table 13 depicts representative droplet patterns seen for each of these distances. For reference, each image is at the scale of 1mm x 1mm.

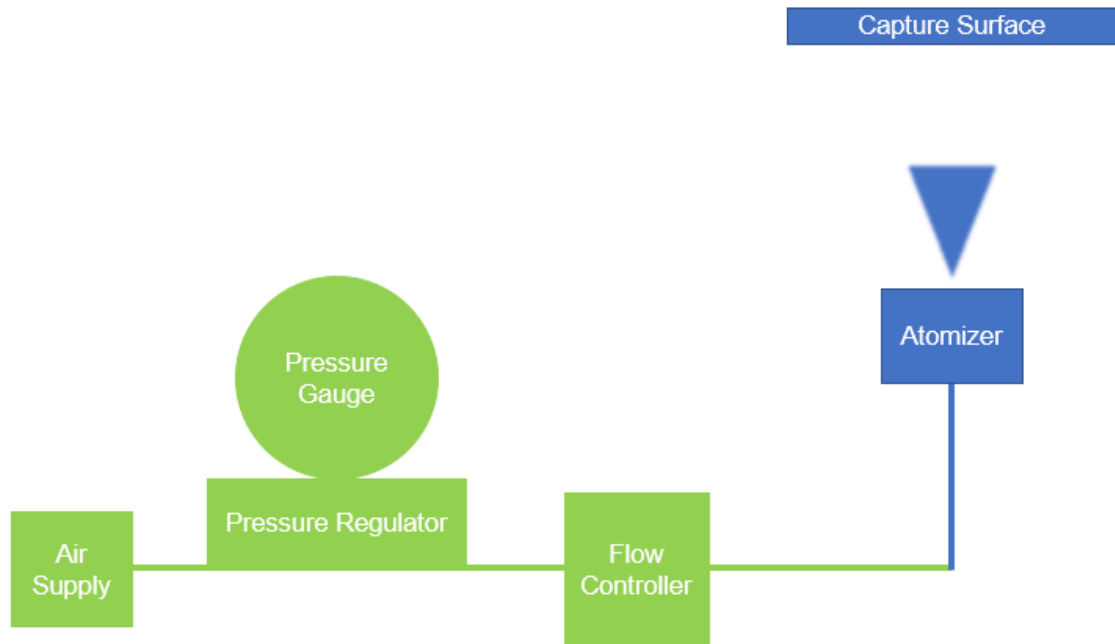
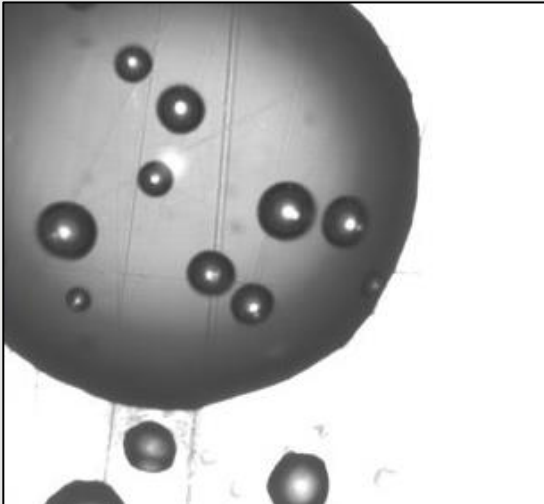
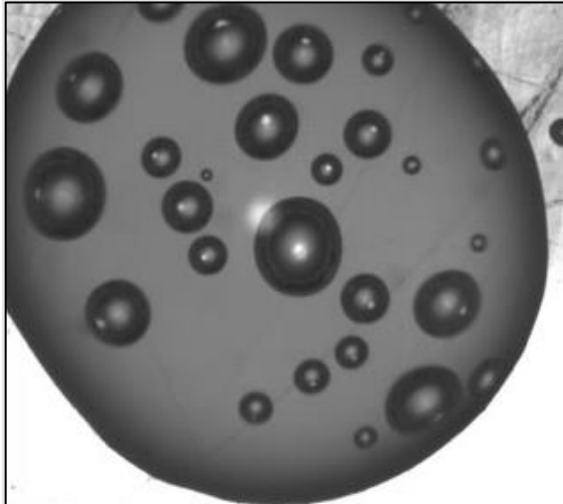
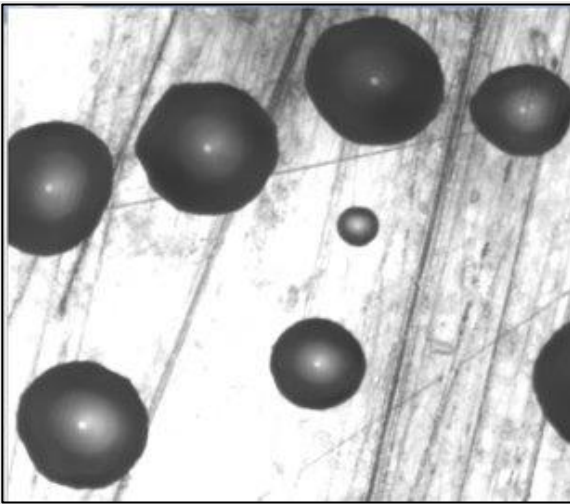
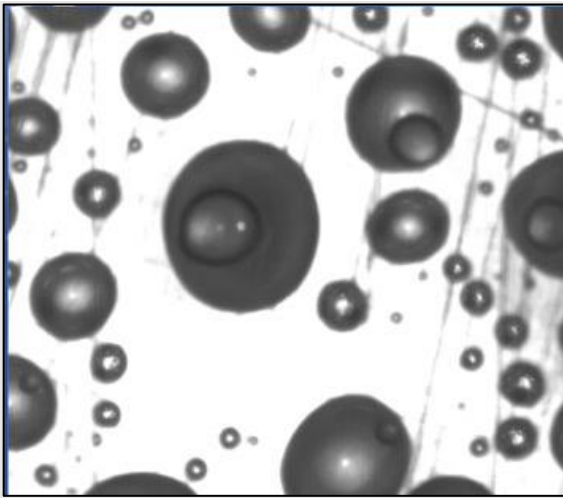


Figure 61: Experimental Setup for Droplet Testing

Table 13: Droplets Captured at Various Distances from the Atomizer, Air Pressure of 30 psi,
Each Image 1mm x 1mm

Distance of 5 in.	Distance of 5.5 in
 A grayscale micrograph showing several dark, spherical droplets of varying sizes on a light-colored, textured surface. The droplets are scattered across the frame, with some appearing larger and more prominent than others.	 A grayscale micrograph showing a higher density of dark, spherical droplets compared to the 5 in. distance. The droplets are more numerous and appear to be more uniformly distributed across the textured surface.
Distance of 5.75 in.	Distance of 7 in.
 A grayscale micrograph showing a few large, dark, spherical droplets on a textured surface. The droplets are more widely spaced, and the surface texture is more pronounced than in the previous images.	 A grayscale micrograph showing a very high density of dark, spherical droplets. The droplets are packed closely together, and the surface texture is less visible due to the high concentration of droplets.

Measuring the various droplet sizes seen at each of the distances, a range of values was compiled. Table 14 summarizes the range of droplet sizes seen at each of the different distances from the atomizer.

Table 14: Range of Droplet Sizes at Different Distances from the Atomizer

Distance from Atomizer	Min. Droplet Diameter	Max. Droplet Diameter
5 in.	0.1 mm	0.7 mm
5.5 in.	0.05 mm	1 mm
5.75 in.	0.1 mm	0.2 mm
7 in.	0.03 mm	0.3 mm

The range of sizes seen for each of the distances from the atomizer shows that at closer distances, there is a wider range of sizes. At 5.75 in., there is more of a consistent size variation. At 7 in., the droplet sizes are much smaller overall. Thus, balancing the experimental desire for uniform droplets or vapor poor conditions led to the ideal separation distance for water to be about 5.75 inches. The further the atomizer is moved from its desired position the more evaporation that will occur.

4.3 Droplet Dispersion Angles

When doing droplet size testing a significant change in the dispersion angle of the atomizer was noticed. The atomizer is listed to have a dispersion angle of 70 degrees. During testing the angle would decrease sporadically. Image analysis was done on images taken from testing the dispersion angle to find out what the two different angles were. The dispersion angle was calculated at 74 degrees in Figure 63 which is within the error expected from the quality of the image. The angle in Figure 62 was 34 degrees which is nowhere near the listed angle. After analysis and discussion, the team concluded the smaller dispersion angle can be attributed to the low amount of water during testing. When the water in the pipes gets low the air that is pressurizing

the water forces its way through the atomizer reducing the amount of water going through the system and decreasing the angle the water is being dispersed. To combat this effect, a larger amount of fuel will need to be in the piping to keep the air from entering the atomizer. The figures below show the angles of dispersion found during testing.



Figure 62: 34 Degree Angle of Dispersion at 30 psi



Figure 63: 74 Degree Angle of Dispersion at 30 Psi

4.4 Sonic Nozzle Validation

For a choked flow, the flow rate at the nozzle throat can be expressed by Equation (31) where p_0 and T_0 are the stagnation pressure and temperature (John and Keith, 2006). R is the gas constant, A is the area of the nozzle throat, γ is the specific heat ratio for air. The stagnation pressure and temperature are related to the local pressure and temperature by Equations (32) and (33) where M is the Mach number.

$$\dot{m}_{max} = \frac{p_0 A}{\sqrt{RT_0}} \sqrt{\gamma} \left(\frac{\gamma + 1}{2} \right)^{-\frac{\gamma+1}{2(\gamma-1)}} \quad (31)$$

$$p = \frac{p_0}{\left(1 + \frac{\gamma-1}{2} M^2 \right)^{\frac{\gamma}{\gamma-1}}} \quad (32)$$

$$T = \frac{T_0}{1 + \frac{\gamma-1}{2} M^2} \quad (33)$$

From these equations, the mass flow rate depicts a direct linear relation with pressure, as pressure increases, mass flow rate increases. This relation was used to validate the performance of the sonic nozzles.

The air flow rate exiting the sonic nozzle at a certain upstream air pressure was measured with the flow meter. This was repeated for three sonic nozzles, E-22-SS, E-17-SS, and E-12-SS, at three different pressures each, 40 psi, 70 psi, and 100 psi. The results of these tests are compiled in Figure 64.

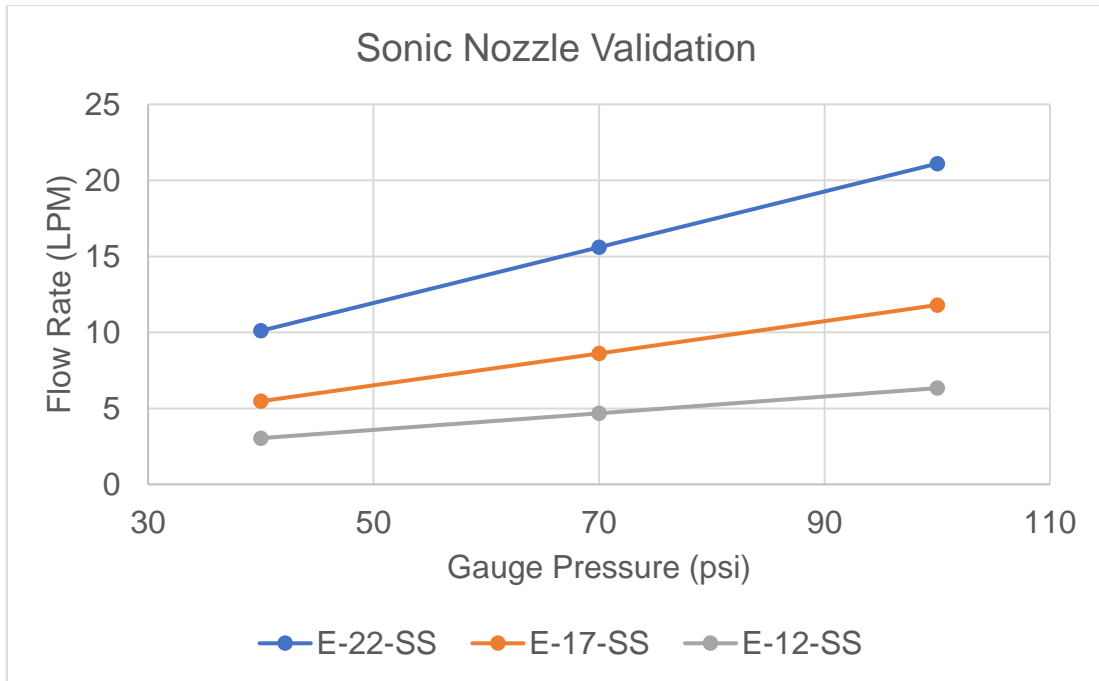


Figure 64: Flow Rate Exiting Three Types of Sonic Nozzles under Three Pressure Conditions

From the plot, as expected, the sonic nozzles depict a positive linear relation between upstream pressure and flow rate. These values also compare well with the values provided by the manufacturer. Thus, these results ensure that the sonic nozzles are performing as required.

5 Challenges

5.1 Design Challenges

Most of the team had never faced a design project this intricate with so many unknown variables. Many design challenges were the result of our novice experience. Sticking to our educational backbone was key in overcoming some of these design challenges. Creating visual tools and iterating greatly impacted our decisions. The growth from our original ideas of part placement and flow control can be seen in the heavily iterated P&ID diagram. After every iteration we understood the flow and comparable flow systems much better. In the multiple iterations of a

pressure vessel, it can be seen how the team's original design changed based off other experimental designs and the idea our original design may not be modular enough and too cumbersome. Another major design challenge came about when trying to fully understand and recreate others experimental design philosophies and calculations. When calculating droplet vaporization times, it was difficult to decode all the assumptions necessary to recreate a consistent model. There was also an initial difficulty in understanding the MATLAB modeling of nozzle design used by other studies due to their omission of certain key parameters. Thus, it took more time to recreate their results and apply those techniques to the efforts of this work.

5.2 Experimental Challenges

Selection of parts for our flow system was challenging as after searching a website extensively one could find an item that seems perfect just to find out it doesn't meet the maximum pressure requirement or that it has the wrong type of connection threading. Therefore, narrowing down options and check if they would work appropriately was a process that had to be repeated many times in order to make sure when ordered the correct parts would be delivered.

When conducting the experiments constructing the apparatus for different tests resulted in challenges. When attempting to set up the backup atomizer it was noticed that the adapter for the threads was not included. The team used epoxy and duct tape to secure the atomizer to the fuel lines. Storing the seeder particles in a section of the burner was challenging, a uniform amount of the particles needed to exit the burner. Trial and error modifications were used till a storage device was manufactured to sit behind the burner inlet to allow for a constant stream of particles to be dispersed.

5.3 Global Project Challenges

With the current state of manufacturing in the United States, getting prompt responses and accurate information from companies to purchase their products was a major challenge throughout this project. Dozens of unanswered phone calls and emails, incomplete product information on websites, and lack of inventory for high priority parts for this project led to further delays.

The lead time for sonic nozzles, which were used for controlling the flow rates of air in the experimental setup, was found to be a minimum of twelve weeks. Thus, these were ordered well in advance to ensure that the experimental apparatus could be fully assembled and tested. However, these items were not received until the last few days of the project. The team addressed this challenge by being resourceful with the equipment available and at-hand.

Each component and company brought about their own problems. Such as when there was no further communication between the team and a supplier that had offered to send a certain nebulizer but was never received. The impact of the global Covid-19 pandemic cannot additionally be overstated and most certainly played a role in company responses, response times, and inventory of certain stock.

6 Summary, Conclusions, Recommendations, Broader Impacts

6.1 Summary

The team's efforts to design an experimental apparatus to study the phenomena of relight began with gaining an understanding of relight and its pertinent conditions. The team researched high-altitude relight and issues that jets face when attempting to relight their engines. Once these conditions were understood, expressed in section 1, the members split up design aspects to focus on. The four main subsystems were burner design, flow delivery system, fuel dispersion methods,

and pressure vessel. A converging nozzle was designed to maximize the uniformity of the flow. A flow system was designed to inject the correct amounts of air to match desired test conditions. The atomizer availability, droplet capabilities, and fuel flow rates were the design criteria for the fuel delivery system design. A pressure vessel was modeled to be expanded by future works. Simulations and models aided in design and validation of design decisions. The team was able to validate and test multiple components of an experimental apparatus to be used for further relight simulation testing.

6.2 Conclusions

The goal of this project was to study the effects of varying conditions, such as pressure and temperature, on the success of relight. Due to shipping delays, much of the equipment necessary for achieving this goal were not received until well into the end of the project timeline. However, with the equipment available to the team, an experimental apparatus was constructed and validated to be able to recreate the necessary conditions. The primary lesson learned throughout this project was how to be flexible and resourceful. Despite numerous setbacks and obstacles, an experimental apparatus validated by complex structural, fluid, and thermal models and various methods of testing were designed and assembled. For example, the sonic nozzles necessary for controlling the mass flow rate of the system did not arrive until the last few days of the project. However, in the meanwhile, the team utilized a flow controller to estimate the volumetric flow rate to conduct tests without the sonic nozzles. Another example includes the lack of proper connection types being available on the market to connect the atomizer to the rest of the flow system. Thus, the team repurposed a combination of several other connectors and epoxy to ensure a proper fit.

6.3 Recommendations for Future Work

Throughout this experiment the team has compiled ideas for future projects to implement and try to continue the project. Based on time constraints and delays in shipping and ordering the team did not have enough time to test or implement these changes but think they would be beneficial to future work pertaining to the experiment.

The team did not have time to integrate the burner design with the atomizer. This integration is key to recreating relight conditions. The burner design created for this project was tested for uniform flow and the atomizer was tested for the droplet dispersion angle and droplet sizes. The two will need to be integrated to continue the experiment further. To fully integrate these two parts, the burner will need to be redesigned. The inlet for the atomizer needs to be expanded, the burner width should be increased to reduce possible droplet interactions with its walls, and the burner contour needs to be further optimized to create a more uniform exit velocity profile. Additionally, this experimental setup should be placed directly under a vent to reduce external disturbances leading to changes in the flow pattern.

If a premixed fuel is used, a one-way valve needs to be added to the fuel flow to stop the fuel from going back down the air flow. This was a problem when testing the atomizer droplet sizes as the water would go back down the tube and risk going into the pressure regulator. Furthermore, trace amounts of water would not flow down the tubing when enough pressurized air would come through causing the angle of dispersion of the atomizer to decrease. The air would also come out of the atomizer forcing the spray angle to decrease significantly.

Further atomizer testing is required if a new atomizer is chosen. The atomizer determined for this project was chosen because of price, effectiveness, and most importantly, availability. Atomizers are typically more expensive, and the team was not able to purchase most of the

atomizers examined due to availability and cost restraints with the rest of the items needed to be purchased such as the NPT connectors, the pressure regulator, the pressure gauges, the flow meters, and the sonic nozzles. If a new atomizer is chosen, new dispersion angle testing and droplet size testing must be done to integrate a new atomizer into the burner configuration.

Future experiments with ethanol should be done to understand which concentrations of ethanol are able to ignite with ease. This test can could be done with a Bunsen burner instead of the relight experimental apparatus. The concentration of ethanol needs to be tested before being used in the experiment to determine if high concentrations of water will ignite allowing more vaporization for the fuel. The researchers would gain the ability to further elongate residence and vaporization times by reducing the speed at which the droplets vaporize. Just to reiterate, slow vaporization times are terrible for engine performance but good for recreating high-altitude relight conditions.

Future efforts should validate the heat transfer simulations and burner insulation through more complex simulations and physical testing. The heat transfer simulations can be expanded to encompass the burner and the piping. Since it was expected that the solutions discussed at the end of section 3.3 were sufficient in coolant design, teams could take different temperature readings within the apparatus to understand the heat physics of this particular real-world experimental apparatus.

6.4 Project Broader Impacts

A clearer understanding of relight, specifically high-altitude relight, will result in a reduction of pollution, greater engine efficiency, and safer travel conditions. Understanding cold, low-density air engine relight, equivalent to high-altitude, could be the deciding design factor in air travel on other planets.

Climate change is a tremendous societal hazard to the continuation of life on Earth as we know it. Solutions to reduce and decrease production of greenhouse gases must be put into effect swiftly. Air travel accounts for 4% of the United States greenhouse gas emissions (Chokshi & Krauss, 2021). Designing engines to reduce pollution has led to heavy investment into lean fuel burning and low NO_x producing engines. These engines, which are better for the environment, suffer from inconsistent relight. The temperatures and fuel consumption used by differing engine types changes relight ease and ability. Inability to reignite modern engines safely and swiftly after flameout is an obstacle to the implementation of more environmentally friendly modern engines.

Aircraft engines, when relighting at high altitudes, waste fuel before successful ignition. Thus, engines additionally emit more harmful pollutants such as nitrogen dioxide and not fully combusted hydrocarbons. Reduction in one pollutant can sometime greatly expand the production and emission of others (Freeman 2018). In order for optimal complete combustion to occur, where carbon dioxide and water are the only constituents, relight must happen readily and repeatedly. Greater understanding of relight allows for the optimization of engine performance leading to less fuel being wasted before a flame begins and engine conditions to more quickly match optimal combustion conditions, in turn increases the completeness of combustion occurring.

A typical commercial jet, a Boeing 747, uses 4 liters of fuel a second. The total number of commercial flights handled by the FAA alone numbered 16.5 mil (FAA 2021). Even marginal improvements in time to reignite the engine would save large amounts of fuel. Making flights more economically and environmentally sustainable. This however might not be the largest factor in studying relight in the modern era. Engine flameout is predicted to happen once out of every hundred thousand flights (Garrison 2006). In catastrophic engine failure, where both engines' flames are extinguished, pilots are forced into very dangerous situations. If airspeed and conditions

inside the combustor are not optimal, pilots must dive to gain airspeed. The other option is glide for an emergency landing. Historically this has led to loss of life, planes, and environmental destruction. Although some might say it is rare, it is important to keep in mind that additional safety risks associated with plane travel has negatively impacted the desire for this form of transportation, due to historical and current perception of flight safety. Furthermore, this lack of desire could cause aviation study to stagnate and add extra strain on air transport.

Overall, a better understanding of high altitude relight would secure a safer, less polluting, and more efficient air transit system. High altitude relight insight could be extrapolated to better prepare for lower density atmospheres seen on other planets, allowing for greater implementation of transportation and travel systems on other planets.

Appendix A: Flow System Parts

Table A1: Final Flow System Parts Details

Company	Product Name	Product Number	Quantity
Omega			
1	Pressure Gauge	DPG104-100G	3x
2	Pressure Regulator	PRG700-2	3x
Swagelok			
3	Brass Tee Connector (F)	B-400-3-4TFT	1x
4	Brass Straight Connector (F)	B-400-7-4RG	6x
5	Brass Straight Connector (M)	B-1010-1-4	1x
6	Straight Connector (F)	B-1010-7-8	1x
7	Stainless Steel Straight Connector (F)	SS-400-7-4RG	10x
8	Stainless Steel Tee Connector (F)	SS-400-3-RTTTF	3x
O'Keefe			
9	Sonic Nozzles (SS)	E-22-SS	1x
		E-17-SS	1x
		E-12-SS	1x
		E-11-SS	1x
		E-9-SS	1x
		E-4-SS	1x
Grainger			
10	Mechanical Flowmeter	2ktw5	1x
11	Mechanical Flowmeter	16x856	1x
12	Reducing Adapter	46M456	1x
13	Atomizer	3AAG2	1x
14	Support Stand and Rings	23YW88	1x
15	Wire Mesh	45TR03	1x

Table A2: Cost Breakdown for Ordered Parts

Omega					
	Pressure Guage	DPG104-100G	3x	\$302.77	\$908.31
	Pressure Regulator	PRG700-2	3x	\$108.82	\$326.46
				Total:	\$1,234.77
Swagelok					
	Tee Connector (female) brass	B-400-3-4TFT	1x	\$18.59	\$18.59
	Straight Connector (female) bra	B-400-7-4RG	6x	\$9.46	\$56.76
	Straight Connector (female) SS	SS-400-7-4RG	10x	\$21.12	\$211.20
	Tee Connector (female) SS	SS-400-3-RTTTF	3x	\$41.58	\$124.74
	Straight Connector (Female)	B-1010-7-8	1x	\$14.08	
				Total:	\$425.37
O'Keefe					
	Sonic Nozzles (SS)	E-22-SS	6x	\$30	\$180
		E-17-SS		Total:	\$180
		E-12-SS			
		E-11-SS			
		E-9-SS			
		E-4-SS			
Brooks					
	Mechanical Flowmeter	2ktw5	1x	\$79.56	
	Mechanical Flowmeter	16x856	1x	\$64.84	
				Total:	\$144
Grainger					
	Atomizer	3AAG2	1x	\$13.86	
	Support Stand and Ring	23YW88	1x	\$62.46	
				Total Cost	\$76.32
Amazon					
	Wire Mesh		1x	\$11.77	
				Total Cost	\$11.77
Harbor Freight Tools					
	Epoxy		1x	\$1.79	
				Total Cost	\$1.79
	Total Order	Cost:		\$2,074.02	

Appendix B: Images of Flow System Parts



Figure B1: Atomizer (courtesy of Grainger)

Item: 3AAG2

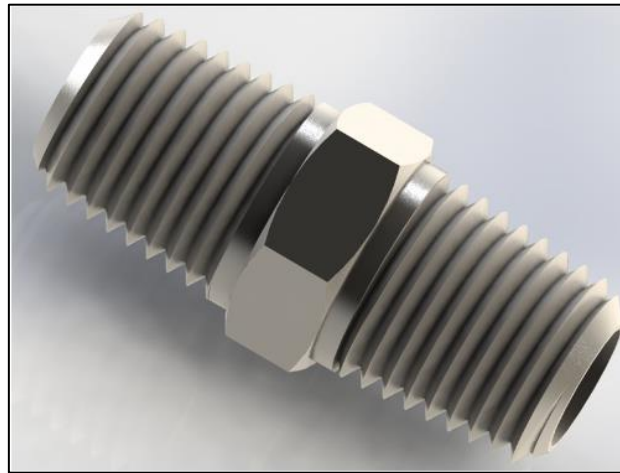


Figure B2: Sonic Nozzle (courtesy of O'Keefe Controls)

Items:

E-22-SS

E-17-SS

E-12-SS

E-11-SS

E-9-SS

E-4-SS

Table B1: Air Flow Table for Sonic Nozzles in SLPM

Metal Orifice Air Flow – SLPM



If it's about precision, it's O'Keefe.

Orifice Diameter Inches	0.004	0.005	0.006	0.007	0.008	0.009	0.010	0.011	0.012	0.013	0.014	0.015	0.016	0.017	0.018	0.019	0.020	0.021	0.022	0.023	0.024	0.025	0.026	0.027	0.028	0.029	0.031	0.032	0.033	
Size Number	4	5	6	7	8	9	10	11	12	13	14	15	16	17	18	19	20	21	22	23	24	25	26	27	28	29	31	32	33	
C_v	0.00035	0.00061	0.00086	0.0012	0.0015	0.0019	0.0025	0.0028	0.0034	0.0038	0.0043	0.0050	0.0055	0.0067	0.0073	0.0080	0.0088	0.0096	0.011	0.012	0.013	0.014	0.016	0.017	0.018	0.019	0.022	0.024	0.025	
Supply Pressure - psig	1	0.035	0.064	0.086	0.127	0.170	0.226	0.280	0.308	0.398	0.45	0.52	0.61	0.66	0.77	0.86	0.96	1.05	1.13	1.29	1.41	1.54	1.67	1.91	1.95	2.21	2.39	2.65	2.88	3.03
	5	0.09	0.16	0.21	0.30	0.40	0.52	0.65	0.71	0.92	1.06	1.21	1.41	1.54	1.76	1.98	2.22	2.47	2.65	2.97	3.24	3.53	3.83	4.34	4.44	4.94	5.31	5.86	6.42	6.80
	10	0.12	0.22	0.31	0.43	0.57	0.74	0.93	1.01	1.29	1.48	1.68	1.95	2.01	2.26	2.54	2.83	3.16	3.53	4.33	4.75	5.18	5.55	6.15	6.43	7.18	7.83	8.63	9.40	9.98
	15	0.16	0.28	0.39	0.54	0.72	0.93	1.17	1.26	1.62	1.85	2.10	2.44	2.50	2.85	3.23	3.57	4.01	4.41	5.35	5.93	6.43	6.95	7.58	7.95	8.78	9.58	10.6	11.6	12.3
	20	0.19	0.33	0.46	0.65	0.85	1.10	1.38	1.49	1.92	2.19	2.49	2.87	2.97	3.40	3.86	4.26	4.84	5.22	6.35	6.95	7.58	8.15	8.90	9.28	10.3	11.2	12.4	13.5	14.3
	25	0.22	0.39	0.53	0.75	0.98	1.27	1.59	1.71	2.20	2.50	2.86	3.28	3.42	3.92	4.45	4.91	5.59	6.01	7.30	7.95	8.65	9.38	10.2	10.7	11.7	12.8	14.2	15.4	16.3
	30	0.25	0.44	0.60	0.85	1.12	1.43	1.80	1.93	2.47	2.82	3.21	3.69	3.87	4.43	5.03	5.56	6.33	6.81	8.23	8.98	9.75	10.6	11.5	12.0	13.2	14.4	15.9	17.3	18.4
	40	0.30	0.54	0.74	1.05	1.38	1.77	2.21	2.37	3.04	3.45	3.93	4.51	4.78	5.47	6.21	6.85	7.81	8.42	10.1	11.0	12.0	13.0	14.1	14.7	16.1	17.5	19.4	21.1	22.5
	50	0.36	0.65	0.88	1.26	1.65	2.10	2.62	2.80	3.58	4.07	4.64	5.31	5.70	6.51	7.40	8.15	9.26	10.0	11.9	13.0	14.2	15.4	16.6	17.3	19.0	20.7	22.9	25.0	26.6
	60	0.42	0.75	1.02	1.46	1.91	2.42	3.02	3.23	4.13	4.70	5.34	6.13	6.61	7.56	8.58	9.46	10.7	11.6	13.8	15.0	16.4	17.7	19.2	20.0	21.9	23.8	26.4	28.8	30.7
70	0.48	0.86	1.16	1.67	2.17	2.75	3.43	3.66	4.68	5.32	6.05	6.96	7.53	8.61	9.77	10.8	12.2	13.2	15.6	17.0	18.5	20.1	21.7	22.7	24.8	27.0	30.0	32.7	34.9	
80	0.54	0.96	1.30	1.87	2.43	3.08	3.83	4.09	5.23	5.95	6.77	7.79	8.46	9.67	11.0	12.1	13.7	14.9	17.5	19.0	20.7	22.5	24.2	25.3	27.7	30.2	33.6	36.7	39.0	
90	0.60	1.07	1.44	2.08	2.69	3.40	4.23	4.51	5.78	6.58	7.49	8.62	9.38	10.7	12.2	13.4	15.2	16.5	19.3	21.0	22.9	24.9	26.8	28.0	30.7	33.5	37.2	40.6	43.2	
100	0.66	1.17	1.58	2.28	2.95	3.72	4.63	4.94	6.33	7.22	8.21	9.46	10.3	11.8	13.4	14.7	16.6	18.0	21.1	23.0	25.1	27.4	29.4	30.8	33.7	36.8	40.9	44.6	47.5	
Vacuum Level In. Hg. (Closed Flow)	5	0.053	0.096	0.129	0.191	0.253	0.332	0.406	0.450	0.582	0.661	0.773	0.899	0.977	1.14	1.28	1.41	1.55	1.70	1.90	2.10	2.30	2.48	2.74	2.83	3.16	3.41	3.78	4.12	4.32
	10	0.069	0.124	0.168	0.246	0.324	0.421	0.519	0.564	0.730	0.834	0.972	1.12	1.24	1.41	1.58	1.79	1.96	2.18	2.44	2.68	2.89	3.13	3.44	3.58	4.00	4.30	4.77	5.16	5.43
	15	0.075	0.134	0.185	0.268	0.351	0.455	0.566	0.614	0.792	0.902	1.07	1.22	1.35	1.55	1.75	1.94	2.19	2.32	2.61	2.85	3.12	3.34	3.65	3.78	4.20	4.51	5.05	5.45	5.72
20	0.075	0.134	0.185	0.268	0.351	0.455	0.566	0.614	0.792	0.902	1.07	1.22	1.35	1.55	1.75	1.94	2.19	2.32	2.61	2.85	3.12	3.34	3.65	3.78	4.20	4.51	5.05	5.45	5.72	
30	0.075	0.134	0.185	0.268	0.351	0.455	0.566	0.614	0.792	0.902	1.07	1.22	1.35	1.55	1.75	1.94	2.19	2.32	2.61	2.85	3.12	3.34	3.65	3.78	4.20	4.51	5.05	5.45	5.72	



Figure B3: Mechanical Flowmeter, (courtesy of Brooks)

Items:

2ktw5

16x856



Figure B4: NPT Connector (courtesy of Swagelok)

Items:

B-400-3-4TFT

B-400-7-4RG

B-1010-1-4

B-1010-7-8

SS-400-7-4RG

SS-400-3-RTTTF



Figure B5: Pressure Gauge (courtesy of Omega)

Item: DPG104-100G



Figure B6: Pressure Regulator (courtesy of Omega)

Item: PRG700-2

Appendix C: 2D CAD Drawings

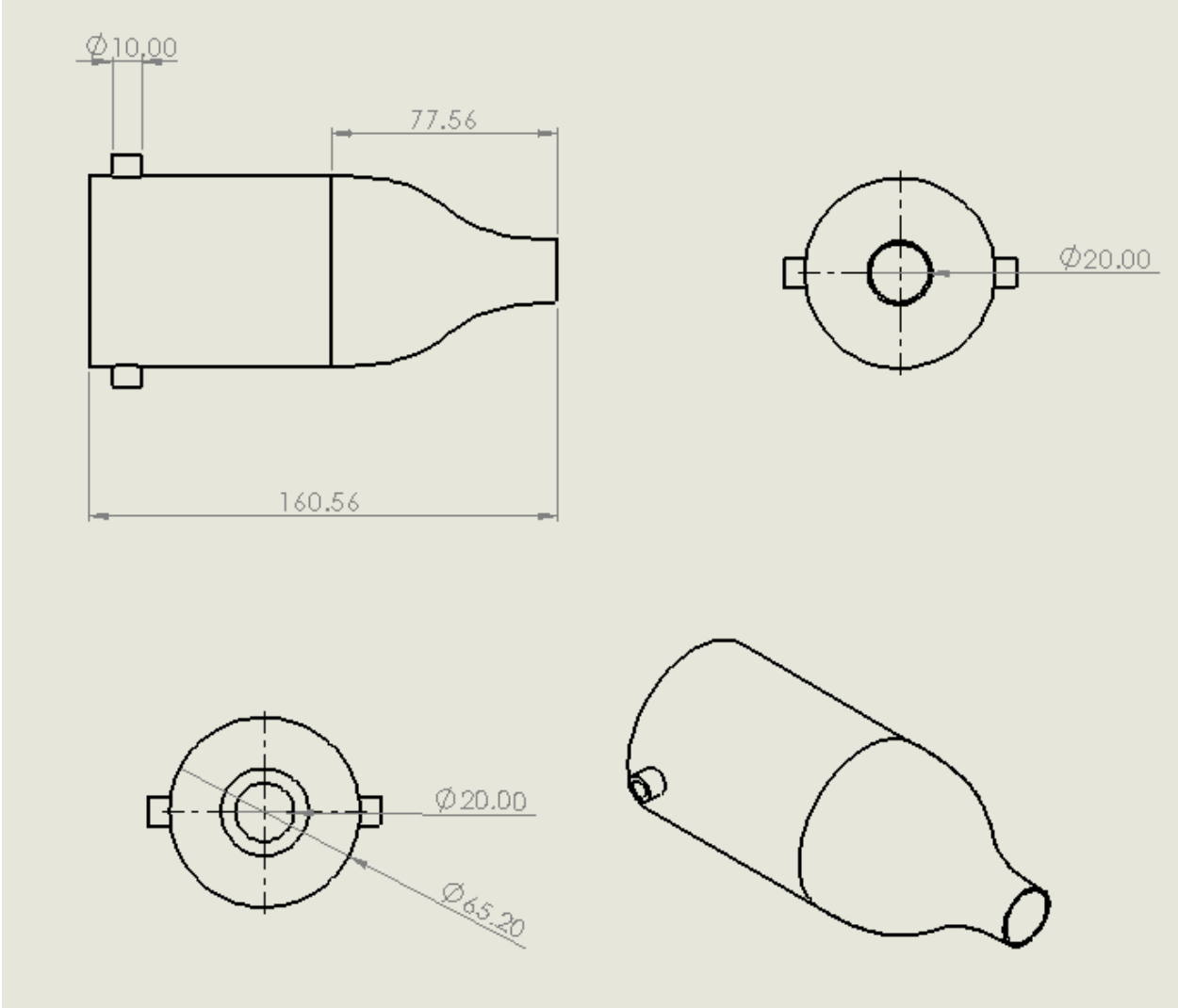


Figure C1: 2D CAD Drawing for Burner (mm)

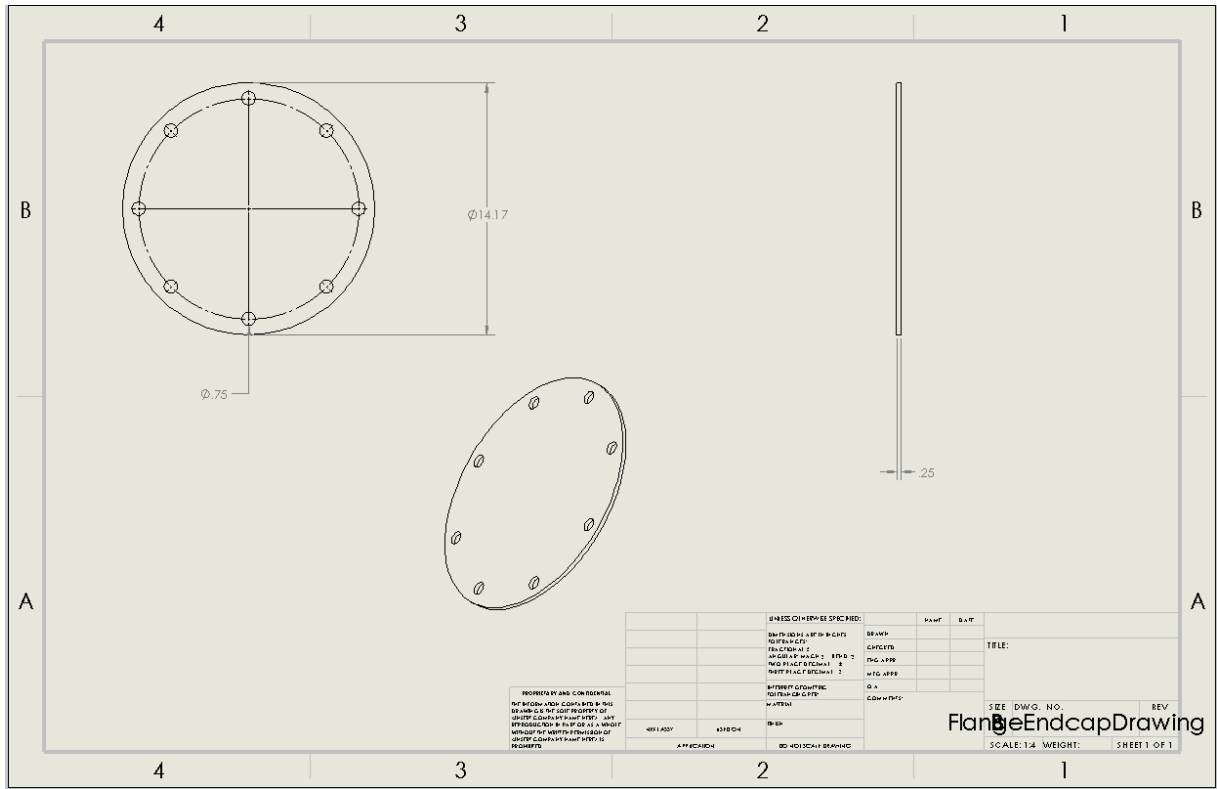


Figure C2: 2D CAD Drawing for Flange Endcap in Inches

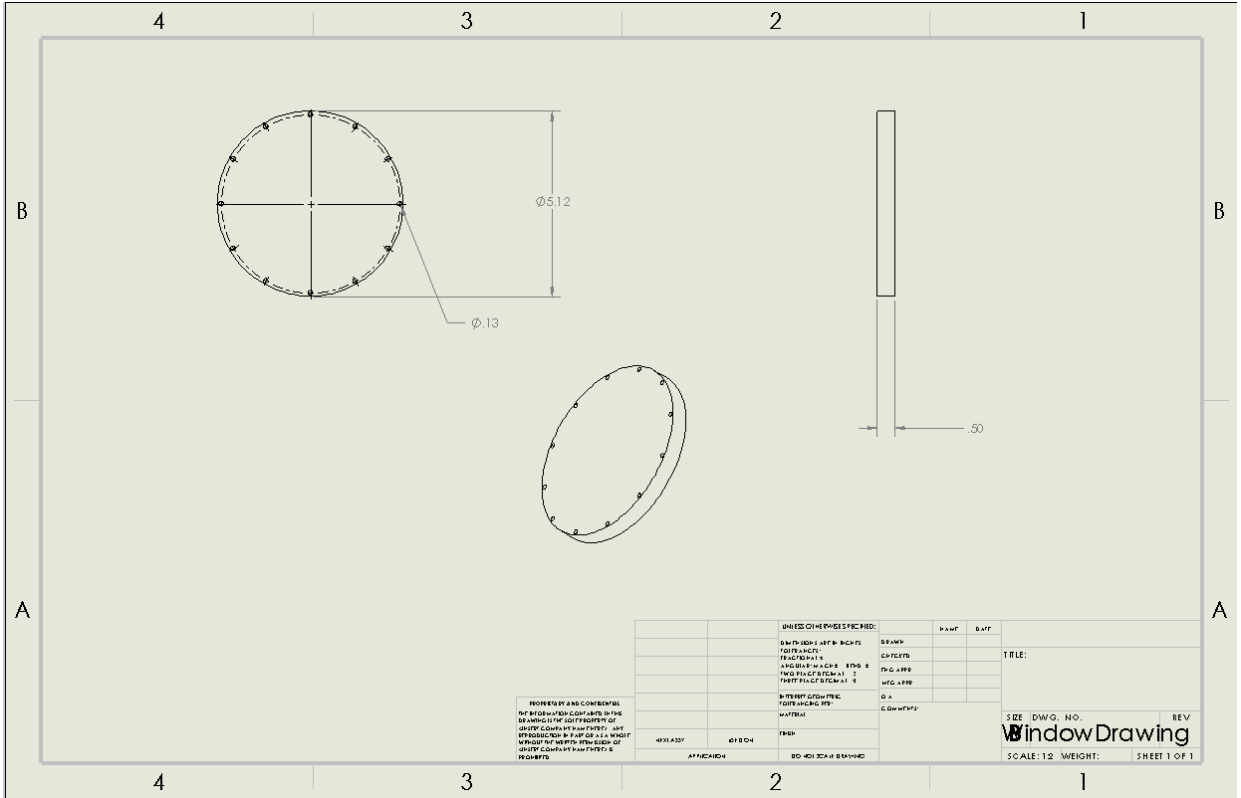


Figure C3: 2D CAD Drawing for Window in Inches

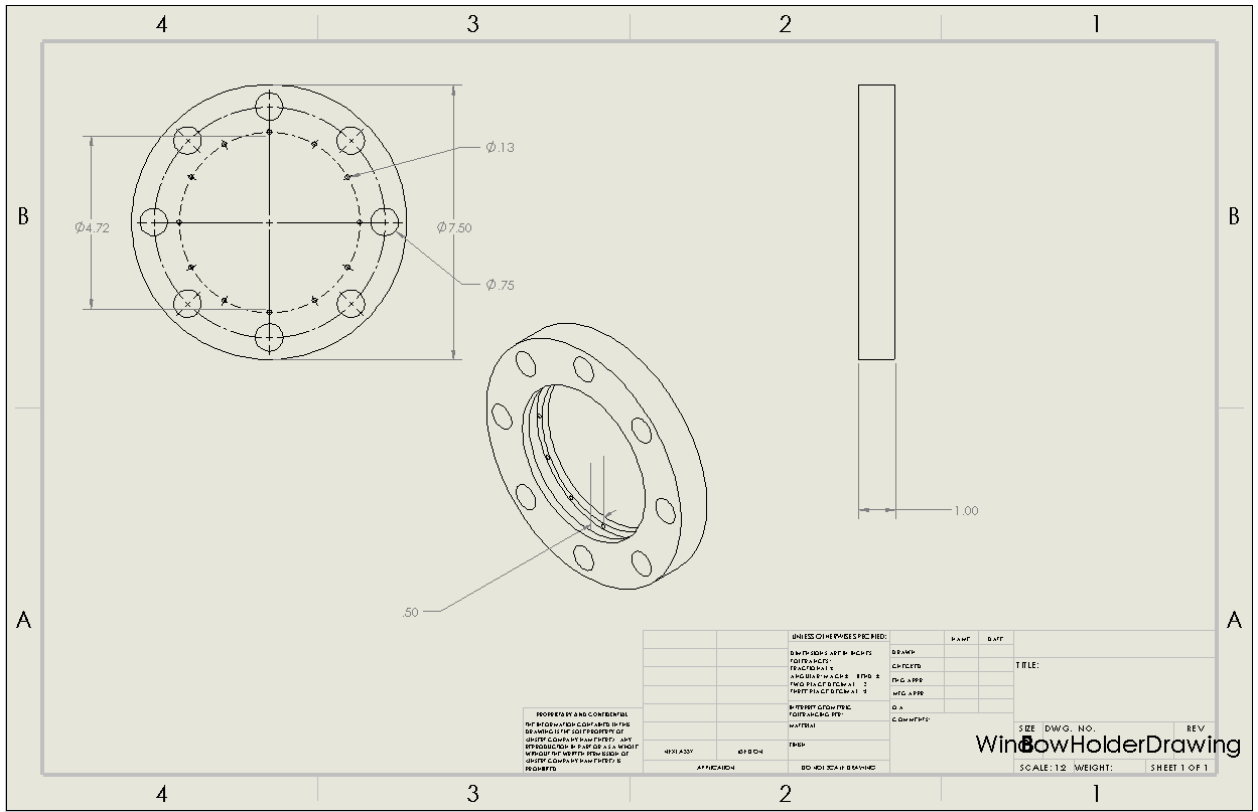


Figure C4: 2D CAD Drawing for Window Holder in Inches

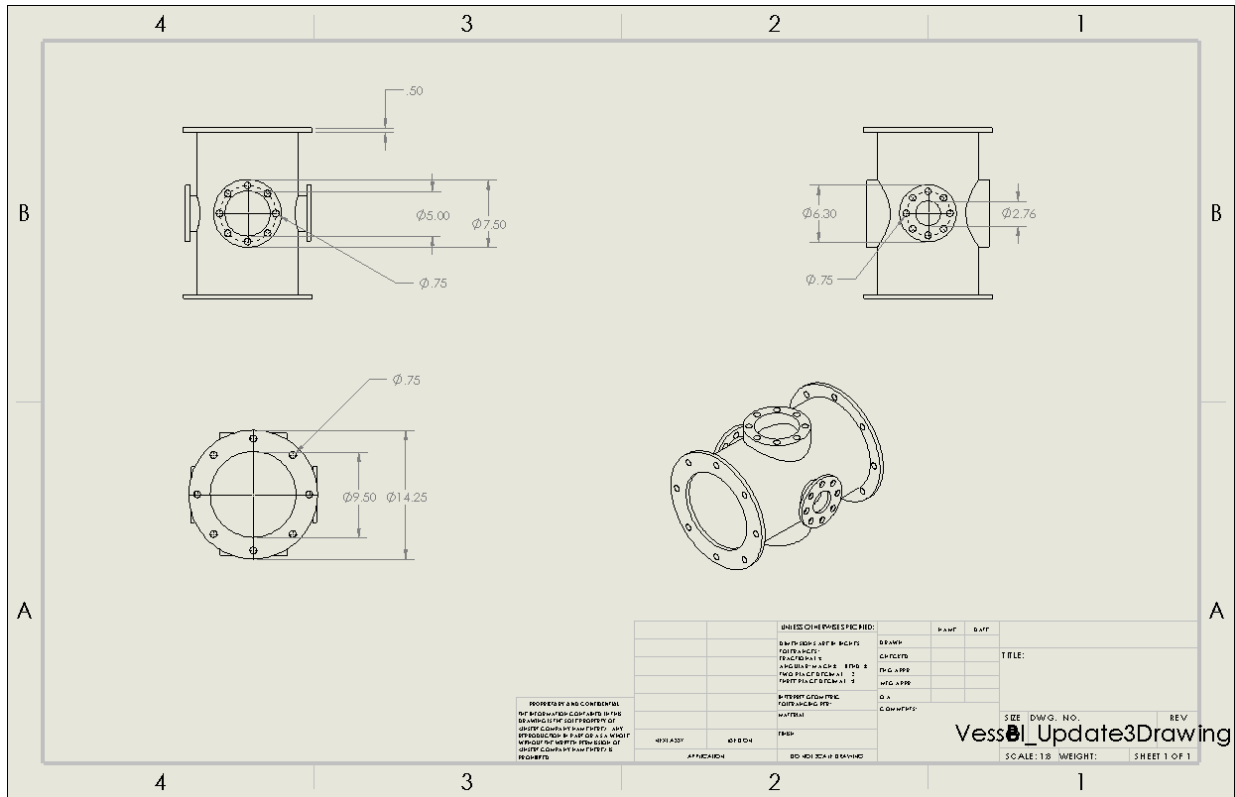


Figure C5: 2D CAD Drawing for Vessel Body in Inches

References

- Ahmed, S. . et al. (2007) Measurements of ignition probability in turbulent non-premixed counterflow flames. *Proceedings of the Combustion Institute*. [Online] 31 (1), 1507–1513.
- Animagraffs. (2019) *How Jet Engines work*, YouTube, <https://www.youtube.com/watch?v=L24Wf0VITE0>.
- Atkins, M. (2016) ‘Chapter 5 - Velocity Field Measurement Using Particle Image Velocimetry (PIV)’, in *Application of Thermo-Fluidic Measurement Techniques*. [Online]. Elsevier Inc. pp. 125–166.
- Ballal, & Lefebvre, A. (1979). Ignition and flame quenching of flowing heterogeneous fuel-air mixtures. *Combustion and Flame*, 35, 155–168. [https://doi.org/10.1016/0010-2180\(79\)90019-1](https://doi.org/10.1016/0010-2180(79)90019-1)
- Ben Gida, H., Gurka, R., and Liberzon, A. (2020) "OpenPIV-MATLAB — An open-source software for particle image velocimetry; test case: Birds’ aerodynamics," *SoftwareX*. <https://doi.org/10.1016/j.softx.2020.100585>
- Bergthorson, J. M. (2005) *Experiments and Modeling of Impinging Jets and Premixed Hydrocarbon Stagnation Flames*. California Institute of Technology
- Burbano, H. (2017). *Pressure Effects on C1-C2 Hydrocarbon Laminar Flames*. University of Southern California
- Chong, C. T. & Hochgreb, S. (2011) Measurements of laminar flame speeds of liquid fuels: Jet-A1, diesel, palm methyl esters and blends using particle imaging velocimetry (PIV). *Proceedings of the Combustion Institute*. [Online] 33 (1), 979–986.

- Choksi, N. & Clifford, K. (2021) A Big Climate Problem With Few Easy Solutions: Planes. *The New York Times*. <https://www.nytimes.com/2021/05/28/business/energy-environment/airlines-climate-planes-emissions.html>.
- Darabiha, N. et al. (1993) Laminar counterflow spray diffusion flames: A comparison between experimental results and complex chemistry calculations. *Combustion and flame*. [Online] 95 (3), 261–275.
- Egolfopoulos, F. et al. (2014) Advances and challenges in laminar flame experiments and implications for combustion chemistry. *Progress in energy and combustion science*. [Online] 4336–67.
- Federal Aviation Administration. (2021). *Air Traffic By The Numbers*. [Online] Accessed 2022. https://www.faa.gov/air_traffic/by_the_numbers/
- Figura, L. & Gomez, A. (2012) Laminar counterflow steady diffusion flames under high pressure ($P \leq 3$ MPa) conditions. *Combustion and flame*. [Online] 159 (1), 142–150.
- Freeman, S. & et al. (2018) Trading off Aircraft Fuel Burn and NO_x Emissions for Optimal Climate Policy. ACS Publications Environmental Science Technology. [Online] 52,5,2498-2505. <https://pubs.acs.org/doi/10.1021/acs.est.7b05719>.
- Garrison, P. (2006). Flameout. *Air & Space Magazine*, [Online] <https://www.smithsonianmag.com/air-space-magazine/flameout-9043856/>.
- Hoghooghi, H. et al. (2016) Optimization of a subsonic wind tunnel nozzle with low contraction ratio via ball-spine inverse design method. *Journal of mechanical science and technology*. [Online] 30 (5), 2059–2067.
- Jarosinski, J. & Veyssiere, B. (2009) *Combustion phenomena : selected mechanisms of flame formation, propagation, and extinction* . [Online]. Boca Raton: CRC Press.

- Ji, C. et al. (2010) Propagation and extinction of premixed C 5–C 12 n-alkane flames. *Combustion and flame*. [Online] 157 (2), 277–287.
- John, J. E. A. & Keith, T. G. (2006) *Gas dynamics*. 3rd ed. / James E.A. John, Theo G. Keith. Upper Saddle River, N.J: Pearson Prentice Hall.
- Khandelwal, B. (2021). Chapter 3 - Ignition and relight , and impact of alternative fuels. In *Aviation fuels* (pp. 39–58). essay, Academic Press.
- Lefebvre, A. H. (Arthur H., & Ballal, D. R. (2010). *Gas turbine combustion: alternative fuels and emissions* (3rd ed.). Taylor & Francis. <https://doi.org/10.1201/9781420086058>.
- LearnChemE. (2013) *Laminar, Fully-Developed Internal Flow Through a Pipe*. [Online] University of Colorado Boulder. YouTube. <https://www.youtube.com/watch?v=4Oh0wNIZrmk>.
- Li, S. et al. (1992) Experimental and theoretical studies of counterflow spray diffusion flames. *Symposium, International, on Combustion*. [Online] 24 (1), 1503–1512
- McQuarrie, D.A. & Simon, J.D. (2011). *Physical Chemistry, A Molecular Approach*. Viva Student Edition. New Delhi. Vinod Vasishtha for Viva Books Private Limited.
- Morel, T. (1975) Comprehensive Design of Axisymmetric Wind Tunnel Contractions. *Journal of Fluids Engineering*. 97 (2), 225–33. <https://doi.org/10.1115/1.3447255>.
- Niemann, U. et al. (2015) Accuracies of laminar counterflow flame experiments. *Combustion and flame*. [Online] 162 (4), 1540–1549.
- Pubchem. *Methane*. National Library of Medicine. October 2021. [<https://pubchem.ncbi.nlm.nih.gov/compound/Methane>]
- Read, R. *Experimental investigations into high-altitude relight of a gas turbine*. Homerton College University of Cambridge.

- ScienceDirect, 2018, *Viscosity*, <https://www.sciencedirect.com/topics/earth-and-planetary-sciences/viscosity>, Retrieved December 2021.
- Shi, X. et al. (2017) Laminar flame speeds of stratified methane, propane, and n-heptane flames. *Combustion and flame*. [Online] 176 (C), 38–47.
- Simon, V. et al. (2017) *Dimensional Analysis for Engineers*. Cham: Springer International Publishing AG.
- Sinclair, G. B., & Helms, J. E. (2015). A review of simple formulae for elastic hoop stresses in cylindrical and spherical pressure vessels: What can be used when. *International Journal of Pressure Vessels and Piping*, 128, 1–7. <https://doi.org/10.1016/j.ijpvp.2015.01.006>
- Walker, J. (1975). “The Madness of Stirring Tea.” *The Flying Circus of Physics*. John Wiley & Sons, inc. P. 97. ISBN 0-471-91808-3
- White, F. M. (1974) *Viscous fluid flow*. New York: McGraw-Hill.
- Wikipedia Contributors. “Heat Exchanger.” *Wikipedia, The Free Encyclopedia*, Wikimedia Foundation. Retrieved March 2022, https://en.wikipedia.org/wiki/Heat_exchanger.
- Wikipedia Contributors. “Vortex Tube.” *Wikipedia, The Free Encyclopedia*, Wikimedia Foundation. Retrieved March 2022, https://en.wikipedia.org/wiki/Vortex_tube.
- Wu, Y. et al. (2018) Experimental Investigation of Laminar Flame Speed Measurement for Kerosene Fuels: Jet A-1, Surrogate Fuel, and Its Pure Components. *Energy & fuels*. [Online] 32 (2), 2332–2343.